Title

MRI Reconstruction and Motion Compensation Techniques for Liver Fat and R2* Quantification

Author

Shih, Shu-Fu

Publication Date

2024

Peer reviewed|Thesis/dissertation

UNIVERSITY OF CALIFORNIA

Los Angeles

MRI Reconstruction and Motion Compensation Techniques for Liver Fat and R_2* Quantification

A dissertation submitted in partial satisfaction of the

requirements for the degree Doctor of Philosophy

in Bioengineering

by

Shu-Fu Shih

2024

ABSTRACT OF THE DISSERTATION

MRI Reconstruction and Motion Compensation Techniques for Liver Fat and R_2* Quantification

by

Shu-Fu Shih

Doctor of Philosophy in Bioengineering

University of California, Los Angeles, 2024

Professor Holden H. Wu, Chair

Metabolic dysfunction-associated steatotic liver disease (MASLD), formerly known as non-alcoholic fatty liver disease (NAFLD), is the most common chronic liver disease with a current global prevalence of 25% to 40%. MASLD is associated with the metabolic syndrome and cardiovascular morbidity, and can progress to fibrosis and cirrhosis. Chronic liver diseases such as viral hepatitis and MASLD can also lead to hepatic iron overload. Magnetic resonance imaging (MRI) provides non-invasive evaluation of hepatic steatosis and iron overload by quantifying proton-density fat fraction (PDFF) and R_2*. Conventional MRI techniques for liver PDFF and R_2* quantification require breath-holding, which can be challenging for children and elderly patients. 3D stack-of-radial MRI techniques have been proposed for self-gated free-breathing liver PDFF and R_2* quantification. However, several challenges remain, including residual streaking artifacts from system imperfections, long scan acquisition times,

computationally expensive reconstructions, and insufficient modelling of non-rigid liver motion during free-breathing. Techniques to overcome these challenges are important for a wide clinical adoption of free-breathing MRI techniques for liver PDFF and R_2* quantification. Additionally, in recent years, there has been an increased interest in lower-field MRI systems. A less expensive lower-field MRI system with a larger bore diameter may improve accessibility and comfort for populations with obesity and at risk for fatty liver diseases. However, the low signal-to-noise ratio problem can impact image quality and quantification accuracy. Therefore, noise reduction techniques are important to improve liver PDFF and R_2* quantification in lower-field MRI systems.

This work focuses on developing MRI reconstruction techniques to improve liver PDFF and R_2* quantification. First, this work developed a phase-preserving beamforming-based technique to effectively reduce radial streaking artifacts from system imperfections. This technique can be further integrated with motion-resolved reconstruction to improve self-gated free-breathing liver PDFF and R_2* quantification. Second, this work developed an uncertainty-aware physics-driven deep learning network for rapid reconstruction of PDFF and R_2* maps from self-gated free-breathing MRI. The uncertainty maps generated from the network can be used to predict quantification errors and improve reliability of deep learning reconstruction results. Third, this work developed a compressed sensing reconstruction model with non-rigid motion compensation to improve and accelerate self-gated free-breathing liver PDFF and R_2* quantification. Last, this work developed and evaluated image and k-space denoising techniques that can improve quantification accuracy and precision of Cartesian-based liver PDFF and R_2* quantification at 0.55T. These technical advancements can provide accurate and motion-robust liver fat and R_2* quantification.

The dissertation of Shu-Fu Shih is approved.

Kyunghyun Sung

Dan Ruan

Xiaodong Zhong

Holden H. Wu, Committee Chair

University of California, Los Angeles

2024

Dedicated to my parents:

Kun-Feng Shih & Mei-Hui Yeh

TABLE OF CONTENTS

LIST OF ABBREVIATIONS

ΔTE: echo spacing

2D/3D: two/three dimensional

ACC: adaptive coil combination

ACR: American College of Radiology

ACS: autocalibration signal

aSNR: apparent signal-to-noise ratio

BH: breath-holding

BMI: body mass index

CAIPIRINHA: Controlled Aliasing In Parallel Imaging Results IN Higher Acceleration

ConvNet: convolutional neural networks

CoV: coefficient of variation

CPU: central processing unit

CS: compressed sensing

CSE: chemical shift encoded

DL: deep learning

DVF: deformation vector field

DWI: diffusion weighted imaging

FA: flip angle

FB: free-breathing

FLOP: floating-point operation

FOV: field of view

GAN: generative adversarial network

GC: graph-cut

GPU: graphics processing unit

GRAPPA: GeneRalized Autocalibrating Partial Parallel Acquisition

GRE: gradient recalled Echo

HIPAA: Health Insurance Portability and Accountability Act

IRB: institutional review board

KLEANER: K-space Low-rankness Enabled Additive NoisE Removal

LoA: limits of agreement

LORAKS: Low-Rank modelling of Local k-Space Neighborhoods

MAP: maximum a posteriori

MASH: Metabolic Dysfunction-Associated Steatohepatitis

MASLD: Metabolic Dysfunction-Associated Steatotic Liver Disease

MD: mean difference

mm: millimeter

MP: Marchenko-Pastur

MRE: Magnetic Resonance Elastography

MRI: Magnetic Resonance Imaging

MRS: Magnetic Resonance Spectroscopy

ms: millisecond

MSE: mean squared error

MVDR: minimum-variance distortionless response

NAFLD: Non-Alcoholic Fatty Liver Disease

NASH: Non-Alcoholic Steatohepatitis

NRMSE: normalized root mean squared error

NUFFT: non-uniform fast Fourier transform

PCA: principal component analysis

PDFF: proton density fat fraction

PI: parallel imaging

PT: Pilot Tone

QIBA: Quantitative Imaging Biomarker Alliance

RLLR: robust locally low-rank denoising

RMT: Random Matrix Theory

ROI: region of interest

s: second

SIR: signal-to-interference ratio

SNR: signal-to-noise ratio

SSIM: structural similarity index

std: standard deviation

SURE: Stein's Unbiased Risk Estimate

SVD: singular value decomposition

T: Tesla

TE: echo time

TR: repetition time

UP-Net: Uncertainty-Aware Physics-Driven Deep Learning Network

LIST OF TABLES

LIST OF FIGURES

LIST OF EQUATIONS

ACKNOWLEDGMENTS

I am immensely grateful for the invaluable support and guidance from my advisor, Dr. Holden Wu, throughout my entire PhD journey. His insightful vision and advice helped me learn how to become a good researcher. I consider myself incredibly fortunate to have Dr. Wu as my advisor on this PhD journey.

I would like to thank my committee members, Dr. Kyunghyun Sung, Dr. Dan Ruan and Dr. Xiaodong Zhong, for the feedback on both research and presentation. They helped me explore my research topic in different perspectives.

I would like to thank the students in the Magnetic Resonance Research Labs (MRRL) Wu Lab. I would like to give special thanks to Sevgi Gokce Kafali. It has truly been a remarkable experience working alongside with her on this PhD journey. I would also like to thank Dr. Zhoahuan Zhang, Dr. Tess Armstrong, Qing Dai, Timoteo Delgado-Esbenshade, Dr. Le Zhang, Dr. Xinzhou Li, Elif Aygun, Ashmita Deb, Wenqi Zhou and Tristan Kelly.

I would like to thank my collaborators from UCLA Radiology and Pediatrics. Specifically, I would like to give special thanks to Dr. Kara L. Calkins, Dr. Shahnaz Ghahremani, Dr. Timothy Adamos, Dr. Katie Strobel, Dr. Jacob Story, Dr. Timothy Ryan, Dr. David Lu and Dr. Ely Felker for their contributions and feedback. I would also like to thank all the study coordinators for subject recruitment.

I would like to give thanks to my collaborators at the University of Arizona, Dr. Maria Altbach, Dr. Ali Bilgin, Dr. Kevin Johnson, Eze Ahanonu, and Brian Toner, for all the insightful discussion and their contributions and feedback on the research project.

I would like to give thanks to my collaborators at the University of Southern California, Dr. Krishna Nayak, Bilal Tasdelen and Ecrin Yagiz, for supporting patient scanning and data

acquisition in the research project. I would like to thank Mary Yung and the research coordinators at the University of Southern California for subject recruitment.

I would like to thank the students and faculty in MRRL and at UCLA who have had helpful discussions with me and provided feedback on my research projects. Specifically, I would like to thank Dr. Peng Hu, Dr. Chang Gao, Dr. Jiahao Lin, Dr. Haoxin Zheng, Dr. Tianle Cao, Yen-Chin Wang. I would like to thank the MR technologists at UCLA for all their help with patient scanning. I learned a lot on scanning and scanner operations from them.

I would like to give thanks to my collaborators at Siemens, Dr. Vibhas Deshpande, Dr. Sophia Cui, Dr. Fei Han, and Dr. Ute Goerke, for providing valuable feedback and resources in my research projects.

I would like to give my deep gratitude to my parents, Kun-Feng Shih and Mei-Hui Yeh, and my sister, Pei-Hsin Shih, who are always there and support me.

VITA

Education

2018-	University of California, Los Angeles Ph.D. (expected) in Bioengineering
2015-2017	National Taiwan University M.S. in Biomedical Electronics and Bioinformatics
2011-2015	National Taiwan University B.S. in Electrical Engineering

Honors and Awards

2022, 2023	Summa Cum Laude Award	*ISMRM*
2020	Magma Cum Laude Award	*ISMRM*
2023	Best Poster Award (2nd place)	*ISMRM Workshop*
2022-2022	Educational Stipend	*ISMRM*
2018	UCLA Graduate Fellowship	*University of California, Los Angeles*
2016	Best Thesis Award	*National Taiwan University*

Peer-Reviewed Journal Articles

[1] **Shu-Fu Shih**, Sevgi Gokce Kafali, Kara L. Calkins, Holden H. Wu. "Uncertainty-Aware Physics-Driven Deep Learning Network for Free-Breathing Liver Fat and R_2* Quantification using Self-Gated Stack-of-Radial MRI". Magnetic Resonance in Medicine 2023; 89(4): 1567-85. doi: 10.1002/mrm.29525

[2] **Shu-Fu Shih**, Holden Wu. "Free-Breathing MRI Techniques for Fat and R_2* Quantification in the Liver". (*Under review*)

[3] **Shu-Fu Shih**, Bilal Tasdelen, Ecrin Yagiz, Zhaohuan Zhang, Xiaodong Zhong, Sophia X. Cui, Krishna S. Nayak, Holden H. Wu. "Improved Fat and R_2* Quantification at 0.55T using Locally Low-Rank Denoising". (*Under review*)

[4] **Shu-Fu Shih**, Sevgi Gokce Kafali, Timoteo I. Delgado, Kara L. Calkins, Holden H. Wu. "Accelerated Free-Breathing Liver Fat and R_2* Quantification using Non-Rigid Motion Compensated Compressed Sensing Reconstruction". (*In preparation*)

[5] **Shu-Fu Shih**, Zhaohuan Zhang, Xiaodong Zhong, Timothy W. Ryan, Holden H. Wu. "Rapid 3D T_2 Mapping in Knee Cartilage with Isotropic Resolution using Dual-Echo Steady State MRI and Compressed Sensing Reconstruction". (*In preparation*)

[6] Sevgi Gokce Kafali, **Shu-Fu Shih**, Xinzhou Li, Grace Hyun J. Kim, Tristan Kelly, Shilpy Chowdhury, Spencer Loong, Jeremy Moretz, Samuel Barnes, Zhaoping Li, and Holden H. Wu. Automated Abdominal Adipose Tissue Segmentation and Volume Quantification on Longitudinal MRI

using 3D Convolutional Neural Networks with Multi-Contrast Inputs. Magnetic Resonance Materials in Physics, Biology and Medicine 2024; 1-16. doi: 10.1007/s10334-023-01146-3

[7] Zhaohuan Zhang, Elif Aygun, **Shu-Fu Shih**, Steven S. Raman, Kyunghyun Sung, Holden H. Wu. "High-Resolution Prostate Diffusion MRI Using Eddy Current-Nulled Convex Optimized Diffusion Encoding and Random Matrix Theory-Based Denoising." Magnetic Resonance Materials in Physics, Biology and Medicine 2024: 1-17. doi: 10.1007/s10334-024-01147-w

[8] Xiaodong Zhong, Marcel D Nickel, Stephan AR Kannengiesser, Brian M Dale, Fei Han, Chang Gao, **Shu-Fu Shih**, Qing Dai, Omar Curiel, Tsu-Chin Tsao, Holden H. Wu, Vibhas Deshpande. "Accelerated Free-Breathing Liver Fat and R_2* Quantification using Multi-Echo Stack-of-Radial MRI with Motion-Resolved Multidimensional Regularized Reconstruction: Initial Retrospective Evaluation". Magnetic Resonance in Medicine 2024. doi: 10.1002/mrm.30117

[9] Chang Gao, Vahid Ghodrati, **Shu-Fu Shih**, Holden H Wu, Yongkai Liu, Marcel Dominik Nickel, Thomas Vahle, Brian Dale, Victor Sai, Ely Felker, Chuthaporn Surawech, Qi Miao, J Paul Finn, Xiaodong Zhong, Peng Hu. "Undersampling artifact reduction for free-breathing 3D stack-of-radial MRI based on a deep adversarial learning network". Magnetic Resonance Imaging 2023; 95:70-79. doi: 10.1016/j.mri.2022.10.010

[10] Katie M. Strobel, Sevgi Gokce Kafali, **Shu-Fu Shih**, Alexandra M. Artura, Rinat Masamed, David Elashoff, Holden H. Wu, Kara L. Calkins. "Investigating the Influence of Pregnancy Complications and Maternal Characteristics on Fetal Body Composition in the Third Trimester of Pregnancy Using Free-Breathing MRI". Journal of Perinatology 2023; 43(1): 44-51. doi: 10.1038/s41372-022-01549-5

[11] Jacob Story, Shahnaz Ghahremani, Sevgi Gokce Kafali, **Shu-Fu Shih**, Kelsey Kuwahara, Kara Calkins, Holden H. Wu. "Using Free-Breathing MRI to Quantify Pancreatic Fat and Investigate Spatial Heterogeneity in Children". Journal of Magnetic Resonance Imaging 2023; 57(2): 508-18. doi: 10.1002/jmri.28337

[12] Sevgi Gokce Kafali, Tess Armstrong, **Shu-Fu Shih**, Grace J. Kim, Joseph L. Holtrop, Robert S. Venick, Shahnaz Ghahremani, Bradley D. Bolster Jr., Claudia M. Hillenbrand, Kara L. Calkins, Holden H. Wu. "Free-Breathing Radial Magnetic Resonance Elastography of the Liver in Children at 3T: A Pilot Study". Pediatric Radiology 2022; 52:1314-1325. doi: 10.1007/s00247-022-05297-8

[13] Tess Armstrong, Xiaodong Zhong, **Shu-Fu Shih**, Ely Felker, David S. Lu, Brian M. Dale, Holden H. Wu. "Free-Breathing 3D Stack-of-Radial MRI Quantification of Liver Fat and R_2* in Adults with Fatty Liver Disease". Magnetic Resonance Imaging 2022; 85:141-152. doi: 10.1016/j.mri.2021.10.016

[14] Chih-Chiang Chang, Zi-Yu Huang, **Shu-Fu Shih**, Yuan Luo, Arthur Ko, Qingyu Cui, Jennifer Sumner, Susana Cavallero, Swarna Das, Wei Gao, Janet Sinsheimer, Alex Bui, Jonathan P Jacobs, Päivi Pajukanta, Holden Wu, Yu-Chong Tai, Zhaoping Li, Tzung K Hsiai. "Electrical Impedance Tomography for Non-Invasive Identification of Fatty Liver Infiltrate in Overweight Individuals". Scientific reports 2021; 11(1):1-12. doi: 10.1038/s41598-021-99132-z

CHAPTER 1

Introduction

1.1 Clinical Significance of Liver Fat and Iron Quantification

Hepatic steatosis is characterized by abnormal accumulation of fat in the liver. Metabolic dysfunction-associated steatotic liver disease (MASLD)[1,2], formerly known as non-alcoholic fatty liver disease (NAFLD), is the most common chronic liver disease with a current global prevalence of 25% to 40%[3,4]. MASLD ranges from simple steatosis to Metabolic Dysfunction-Associated Steatohepatitis (MASH) (formerly known as non-alcoholic steatohepatitis [NASH]), which is hallmarked by liver fibrosis. MASLD is associated with the metabolic syndrome and cardiovascular morbidity, and can progress to fibrosis and cirrhosis that lead to hepatic carcinoma or liver failure[5-10]. Nontargeted liver biopsy is still considered the reference method for diagnosis of hepatic steatosis[11]. However, liver biopsy is an invasive procedure and is not appropriate for long-term monitoring that requires repeated evaluations. Liver biopsy also suffers from sampling bias and the assessment of steatosis on histopathology can be subjective[12,13].

Hepatic iron overload can result from excessive iron accumulation due to hereditary hemochromatosis or occur in patients undergoing repeated blood transfusion therapies[14-16]. Chronic liver diseases such as viral hepatitis and MASLD can also lead to hepatic iron overload[17,18]. Similarly, liver biopsy is the conventional method for iron quantification and iron overload diagnosis[17]. An invasive technique is not suitable for long term monitoring of hepatic iron overload.

As the obesity rate continues to rise across the world, global prevalence rates of MASLD and chronic liver diseases are also increasing. Techniques that can provide non-invasive measurements of hepatic steatosis and iron deposition can play a significant role in disease diagnosis, treatment, and monitoring.

1.2 Conventional MRI Techniques for Liver Fat and R_2* Quantification

Single-voxel proton (^{1}H) MR Spectroscopy (MRS) has high accuracy for measuring tissue fat content by resolving signal contributions from fat and water in the spectral domain. MRS techniques have been shown to be practical, accurate, and reproducible for non-invasive quantification of liver fat. However, similar to biopsy, single-voxel MRS technique suffers from sampling bias[19]. On the other hand, chemical shift-encoded (CSE) MRI methods exploit the difference in the resonance frequencies and resulting phases at different echo times (TE) to separate fat and water signals [20], and enable spatially resolved assessment of hepatic fat content with high spatial resolution and volumetric coverage. Proton density fat fraction (PDFF), a ratio of the signal from fat protons and the signal from fat and water protons combined, has been used for fat quantification[21]. R_2* can be quantified using multi-echo gradient-echo sequences. Studies have found that the presence of tissue fat can affect R_2* quantification accuracy. Since MRI PDFF and R_2* both provide essential information for clinical decision making regarding liver health and are confounding factors for each other in the quantitative MRI signal models for multi-echo gradient-echo sequences, they are often jointly modeled and quantified using CSE MRI methods[22-25].

Major MRI system vendors have commercial products for liver PDFF and R_2* mapping. Although 3D or 2D multi-slice liver PDFF and R_2* mapping methods have been successfully employed in routine clinical protocols, conventional MRI methods using Cartesian data sampling require a breath-holding acquisition of 15 to 20 seconds to reduce motion-induced artifacts in the liver and abdomen[26]. This breath-holding requirement can limit the practical use of MRI for liver PDFF and R_2* mapping in populations that are less compliant with breath-holding instructions or have limited breath-holding capacities, such as the elderly, children, or patients with chronic

diseases[27,28]. Unsuccessful breath-holding that results in motion artifacts can lead to errors for PDFF and R_2* quantification. To overcome the limitations of breath-holding, in recent years there has been an increase in the number of research works developing and evaluating free-breathing MRI techniques for PDFF and/or R_2* quantification in the liver.

1.3 Motion-Robust Free-Breathing MRI Techniques for Fat and R_2* Quantification

1.3.1 Free-Breathing MRI Techniques

Non-Cartesian MRI sampling trajectories often repeatedly visit the k-space center over many readouts and are generally less sensitive to motion due to averaging effects near the center of k-space and the geometries of the sampling trajectories[29]. Motion artifacts in non-Cartesian MRI are usually more distributed and less disruptive compared to Cartesian sampling[30]. However, the artifacts can still degrade the image quality and lead to quantification errors. In addition to artifacts, B_0 field variation, especially near the tissue-air boundary (e.g., the liver-lung interface), can cause errors in R_2* estimation[31]. Studies investigated free-breathing R_2* mapping found elevated R_2* values when respiratory motion is not corrected[32]. One explanation is that directly averaging signal from different motion states, which has different phase dispersions due to B_0 variation, can cause additional artifactually signal decay. In one study that uses 3D stack-of-radial acquisitions for free-breathing PDFF and R_2* quantification[33], an R_2* bias of 18.5 s^{-1} has been reported if respiratory motion is not corrected. These disadvantages, including increased artifacts and quantification errors, can affect conventional breath-holding techniques and free-breathing scans when motion is not properly managed. Free-breathing scans with strategies to manage motion is therefore important for improved diagnostic quality and quantification accuracy.

One strategy to manage motion is to use a motion surrogate signal to prospectively acquire MRI data from a certain motion state or retrospectively group the acquired MRI data into different motion states during image reconstruction[30]. The prospective acquisition or retrospective assignment of data to specific motion states is also referred to as "gating." Self-navigation is one popular approach in non-Cartesian MRI. The central k-space signal (i.e., DC signal)[32] or a z-axis projection signal calculated from k-space data along the $k_x=k_y=0$ line has been used[34,35] to track respiratory motion along the foot-head direction.

1.3.2 Challenges in Image Reconstruction and Motion Modelling

In recent years, free-breathing techniques using stack-of-radial MRI and self-gating motion management have been proposed for liver PDFF and R_2* quantification[36-38]. Studies showed improved quantification accuracy in adult and pediatric MASLD patients, especially in R_2* measurements, when motion gating was applied[33,36]. However, several challenges remained for free-breathing 3D stack-of-radial MRI techniques for liver PDFF and R_2* quantification. First, non-Cartesian MRI is sensitive to system imperfections[39]. Gradient error calibration through radial spoke alignment can only solve linear gradient errors[36,40]. Other imperfection such as B_0 inhomogeneity and gradient non-linearity can results in radial streaking artifacts and affect diagnostic quality and quantification accuracy. Second, motion-resolved reconstruction for self-gated free-breathing PDFF and R_2* quantification requires computationally expensive iterative algorithms[37,38].

1.4 MRI Fat and R_2* Quantification Techniques at Lower Field Strengths

In recent years, there has been increased interest in lower field strength MRI systems because of advantages such as reduced hardware and siting costs and reduction of artifacts in certain applications[41-43]. These systems can increase MRI accessibility to low-resource regions. The larger bore diameters[41] (compared to conventional 1.5T and 3T scanners) that these lower field strengths MRI system provided can also benefit obese patients at risk of fatty liver diseases.

Rapid R_2* decay from high iron overload can make accurate R_2* quantification challenging, especially at 3T. R_2* quantification on lower field strength MRI systems[44-46] (e.g., <1T) can have higher dynamic range. Recently, Campbell-Washburn et al. presented the feasibility of R_2* mapping in liver iron overload patients using a breath-holding multi-echo gradient-echo acquisition at 0.55T[47]. Despite the benefits, the reduction of signal-to-noise ratio (SNR) at lower fields can limit the precision. On the other hand, unlike R_2* values, PDFF measurements do not vary with field strength. Lower field strength MRI can provide a larger bore diameter which can improve comfort for patients with a larger body habitus[46], which is common for patients with MASLD. The feasibility of fat-water separation in breath-holding abdominal scans at 0.55T[48,49] and 0.75T[50] has been demonstrated. However, the in-phase and out-of-phase echo times are much longer at lower fields, which exacerbates the trade-offs between breath-holding acquisition time and imaging parameters. This makes accurate liver PDFF and R_2* quantification with adequate spatial resolution and coverage at lower fields more challenging than at 1.5T and 3T.

1.4.1 Considerations for the Acquisition Parameters

A common choice at 3T is 6 echoes at either out-of-phase or in-phase echo times and a low flip angle of 3° to 5° for reducing the T_1-related bias in PDFF estimation[26]. Due to the longer out-of-phase and in-phase echo times at 0.55T, this strategy would lead to longer TEs and TR that prolong acquisition beyond the acceptable time for one breath-hold. On the other hand, the effect of the T_1-related bias is reduced at 0.55T because of the shortened T_1 values and the increased TR. A larger flip angle that balances between SNR and the T_1-related bias may be considered for accurate PDFF mapping at 0.55T. As the R_2* values change with the field strength[51], TEs for accurate R_2* quantification should also be reconsidered.

1.4.2 Challenges in Scans with Low Signal-to-Noise Ratio

Because of the reduced SNR at lower fields, limited image resolution, reduced volumetric coverage, or longer scan time are common trade-offs to increase SNR for acceptable image quality. Previous works have also shown that the small flip angle required for accurate PDFF quantification (by mitigating T_1 bias[52]) further decreases the SNR and can become a source of quantification errors[53]. Noise reduction is therefore important and necessary for accurate PDFF and R_2* quantification at lower field strengths.

Techniques to reduce noise in MRI are the focus of active research[54]. Image filtering[55] or constrained reconstruction[56] can be used to suppress the rapidly-fluctuating high-frequency noise components. However, these methods incur risks of over-smoothing the images and removing desired signal components. Denoising techniques that can objectively estimate underlying noise variance and suppress noise with minimal over-smoothing effects are being actively explored.

1.5 Specific Aims

The purpose of the dissertation is to develop MRI reconstruction and motion compensation techniques to improve 1) free-breathing liver PDFF and R_2* quantification at 3T and 2) breath-holding Cartesian-based liver PDFF and R_2* quantification at 0.55T. In the long term, these technical breakthroughs will provide a rapid and motion-robust free-breathing liver PDFF and R_2* quantification that can benefit patients with limits breath-holding capacity. Additionally, improving breath-holding liver PDFF and R_2* quantification at 0.55T MRI systems can increase accessibility for populations with obesity and at risk for fatty liver disease.

1.5.1 Aim 1: Phase-Preserving Beamforming-Based Streaking Reduction Method for Free-Breathing Radial MRI

Chapter 2 presents a phase-preserving beamforming-based technique to reduce radial streaking artifacts caused by system imperfections. This study investigated a distinct beamforming formulation that allows phase fidelity to be preserved while suppress streaking artifacts. A pipeline with automatic interference patch selection was also developed to remove the need of manual intervention. The integration of beamforming and compressed sensing reconstruction was further demonstrated in reconstruction of self-gated free-breathing PDFF and R_2* quantification.

1.5.2 Aim 2: Rapid Uncertainty-Aware Deep Learning Reconstruction for Free-Breathing Liver Fat and R_2* Quantification

Chapter 3 presents a deep learning network that reconstructs liver PDFF and R_2* maps from self-gated free-breathing stack-of-radial MRI and provides uncertainty estimation maps that

can be used for predicting quantification errors. This end-to-end deep learning network consists of an artifact suppression module and a parameter mapping module which can suppress artifacts and perform signal fitting. The novel component in this network, uncertainty map for the quantification parameter, further enhances the reliability of deep learning-based reconstruction with the capability of predicting quantification errors.

1.5.3 Aim 3: Improved Accelerated Free-Breathing Liver Fat and R_2* Quantification using Compressed Sensing with Non-Rigid Compensation

Chapter 4 presents a compressed sensing reconstruction framework with non-rigid motion compensation for accelerated free-breathing liver PDFF and R_2* quantification. In this work, deformation vector fields with phase correction terms were used to describe the non-rigid motion information between motion states. Using the non-rigid motion warping operator into a compressed sensing model can lead to sharper quantitative maps with less streaking artifacts.

1.5.4 Aim 4: Accurate Liver Fat and R_2* Quantification at 0.55T using Image and *k*-Space Denoising Techniques

Sub-aim 4.1: Evaluation of Image-Based Locally Low-Rank Principal Component Analysis Denoising in Fat and R_2* Quantification at 0.55T

Chapter 5 evaluates two image-based locally low-rank principal component analysis denoising techniques for liver PDFF and R_2* quantification at 0.55T. This study used a Monte Carlo simulation to investigate the quantification accuracy and precision across different scan acquisition parameters. Based on the simulation results, a multi-echo gradient-echo protocol for liver PDFF and R_2* quantification at 0.55T was designed. The performance of two locally low-

rank principal component analysis-based denoising algorithms were evaluated in phantoms and in *in vivo* liver datasets. This study found that both denoising methods can improve accuracy and precision of PDFF and R_2* quantification at 0.55T.

Sub-aim 4.2: Development of Multi-Coil Multi-Contrast k-Space Denoising Technique for Fat and R_2* Quantification at 0.55T

Chapter 6 presents a novel k-space denoising technique to denoise multi-coil multi-contrast MRI. Using spectral property of block-Hankel matrices constructed by k-space samples, the additive Gaussian noise can be effectively suppressed. The k-space denoising technique can be directly applied in the originally-acquired k-space data and can be applicable for many multi-coil multi-contrast datasets. This study showed that the k-space denoising technique can improve image sharpness when compared with image-based denoising methods in the application of liver PDFF and R_2* quantification at 0.55T.

CHAPTER 2

Phase-Preserving Beamforming-Based Streaking Reduction Method for Free-Breathing Radial MRI

2.1 Introduction

Radial acquisition has been increasingly used in free-breathing abdominal MRI applications[57,58] due to its inherent motion robustness. However, radial acquisition can be sensitive to system imperfections[59,60]. The resulting streaking artifacts can impact image quality or quantification accuracy in quantitative liver MRI. Gradient delay correction methods[61] based on radial spoke alignment have been proposed to correct k-space trajectories. However, this approach cannot fully resolve the effects of system imperfections, such as gradient non-linearity and B_0 field inhomogeneity, and residual streaking artifacts can still occur. This usually becomes accentuated in areas more distant to the isocenter (e.g., especially arms in abdominal scans) and the resulting streaking artifacts can obscure liver features.

Different approaches have been proposed to suppress the streaking artifacts resulting from system imperfections, including 1) coil selection-based methods[62] that automatically choose images from coils with less artifacts and 2) beamforming-based methods[63] that combine images from all coils with specific weights to suppress streaking artifacts. The first method only chooses a subset of coils and can impact the overall signal-to-noise ratio (SNR) in final coil-combined images. Previous work has demonstrated that beamforming-based methods can provide better radial streaking reduction[63]. However, previous beamforming-based methods did not explicitly consider phase and did not evaluate the artifact-suppression performance on phase, which is important for applications including fat quantification[57] and temperature mapping[64].

Additionally, a major challenge of the previous beamforming-based methods is the need to manually select interference regions that one wants to suppress. This hinders the widespread application of such a method for streaking reduction in radial MRI.

In this work, we developed a different beamforming formulation that can suppress streaking artifacts while preserving accurate phase information. We further developed an automatic interference patch selection technique which involves deep learning-based segmentation to avoid the need for manual input in beamforming-based streaking reduction.

2.2 Methods

2.2.1 Adaptive Coil Combination

Here, we briefly introduce the theory of adaptive coil combination[65] which is closely related to the beamforming-based streaking reduction technique that we will introduce in subsequent sections.

We assume the received signal in ith coil is

$$y_i = s_i x + n_i \text{ (Eq. 2-1)}$$

where x represents the underlying magnetization, s_i represents ith coil sensitivities and n_i represents the noise. As the MRI signal is complex-valued, all the variables considered here are complex-valued. The adaptive coil combination method seeks to find coil combination weights w_i such that the coil-combined image

$$m = \sum_i w_i y_i = \sum_i w_i s_i x + w_i n_i \text{ (Eq. 2-2)}$$

has the maximized SNR. An optimization problem is formulated in each signal patch:

$$\underset{w}{\operatorname{argmax}} \frac{E(|w^H(s_i x)|^2)}{E(|w^H n|^2)} = \frac{w^H R_z w}{w^H R_n w} \text{ (Eq. 2-3)}$$

where $E(.)$ represents expectation operator, R_z and R_n represent covariance matrices of received signal sx and noise/interference n which can be estimated from the multi-coil images. It has been demonstrated in previous work that the analytic solution of w is $F(\hat{R}_n^{-1}\hat{R}_z)$, where $F(.)$ extracts the dominant eigenvector [63].

2.2.2 Phase-Preserving Beamforming-Based Streaking Reduction

Similarly, for beamforming-based coil combination, we assume the received signal in the i[th] coil is $y_i = s_i x + n_i$. The only difference is that now n_i represents the interference in the i[th] coil (i.e., the undesired radial streaking artifacts caused by system imperfections). The previously proposed beamforming-based method[63] finds coil combination weights that maximize the signal-to-interference ratio (SIR) instead of adaptive coil combination methods that maximizes the SNR. However, a potential problem in this max-SIR formulation is that phase information is not explicitly considered. Any weight $we^{j\varphi}$ with an arbitrary phase offset φ is also an optimal solution to the optimization problem.

$$\frac{(we^{j\varphi})^H R_z (we^{j\varphi})}{(we^{j\varphi})^H R_n (we^{j\varphi})} = \frac{w^H R_z w}{w^H R_n w} \quad \text{(Eq. 2-4)}$$

The resulting phase will be dependent on the numerical algorithm used to solve the eigenvalue problem. While it may not affect applications that only consider magnitude images, it may contribute to errors in applications when phase is of interest.

Here, we present a new formulation that is based on the minimum-variance distortionless response (MVDR) beamformer in antenna theory[66]. This method finds weights *w* by solving the optimization problem

$$\underset{w}{\operatorname{argmin}}\, w^H R_n w \quad subject\ to \quad \sum_i w_i s_i = 1 \quad \text{(Eq. 2-5)}$$

The constraint $\sum_i w_i s_i = 1$ corresponds to a "distortionless response" which will preserve the signal from a specific direction in a complex domain. The analytic solution to this MVDR problem is $\frac{\hat{R}_n^{-1} s}{s^H \hat{R}_n^{-1} s}$. While s is typically unknown, is can be estimated by extracting the principal component from local patches[65].

We also extended the beamforming techniques to 3D, where the interference region includes patches from several axial slices (**Figure 2-1**). This leads to smoother variation of signal intensity in the interference region, avoiding signal inconsistency in the final reconstructed 3D images.

2.2.3 Automatic Identification of Interference Patches

Previous beamforming-based methods[63,67] required manual selection of interference patches which can prolong the reconstruction processing time. Therefore, we developed an automatic interference patch identification method that can be easily incorporated into the reconstruction pipeline.

A deep learning network, U-Net[68], was trained to segment the images into the body, the left arm, the right arm and the background. Our training data consisted of 20 axial free-breathing abdominal MRI scans using a multi-echo stack-of-radial sequence. After deep learning-based segmentation, two interference patches were automatically selected by choosing the patches with the largest signal intensities in the two arms in each axial slice. The entire pipeline is shown in **Figure 2-1**.

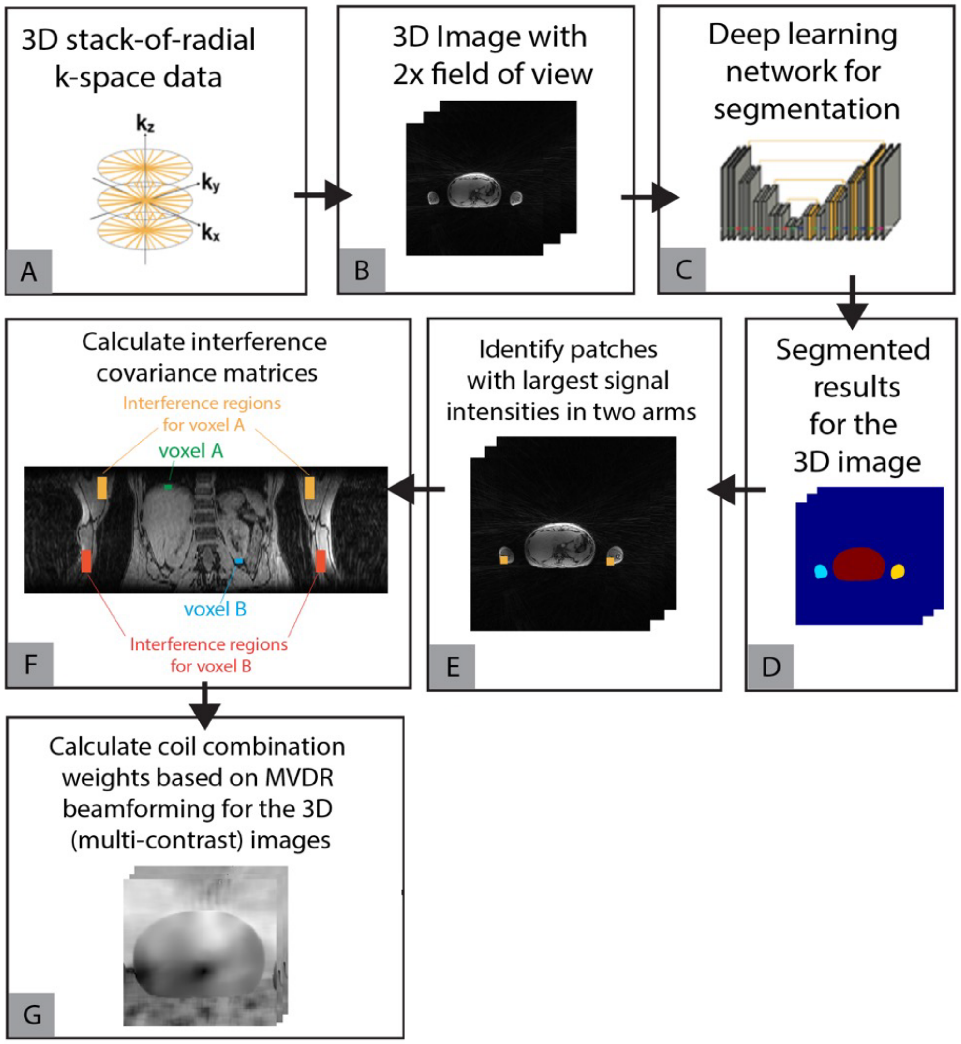

Figure 2-1. Reconstruction pipeline of the phase-preserving beamforming-based radial streaking reduction method with automatic interference patch identification.

2.2.4 Data Acquisition and Image Reconstruction

In a Health Insurance Portability and Accountability Act (HIPAA)-compliant study approved by the local institutional review board, 30 adults underwent abdominal scans on a 3T scanner (MAGNETOM Skyra or Prisma, Siemens Healthineers, Erlangen, Germany). Written informed consent was obtained before scans. We used a 3D multi-echo stack-of-radial gradient echo sequence to acquire data during free-breathing acquisitions. The following scan parameters were used: TEs = [1.23, 2.46, 3.69, 4.92, 6.15, 7.38] ms, TR = 8.85 ms, flip angle = 5°, field-of-

view (FoV) = 300x300 to 460x460 mm^2, slice thickness = 5 mm. Gradient delay correction using radial spoke alignment[57,61] was applied before image reconstruction and coil combination.

The reconstruction was done in MATLAB (R2021a, MathWorks, Natick, Massachusetts). We used the MATLAB built-in "svd" function in the beamforming coil combination (for both Max-SIR and MVDR beamforming).

2.2.5 Evaluation of Streaking Reduction Performance

We compared 3 different coil combination algorithms: 1) adaptive coil combine (ACC) [65], 2) max-SIR beamforming[63], and 3) MVDR beamforming. Beamforming-based methods require identification of an interference source (e.g., arms in abdominal scans). All 3 approaches required estimation of local signal covariance matrices. Different patch sizes (5x5, 11x11 and 17x17) were compared for local patch extraction.

To assess the performance of streaking reduction, we used a metric known as cancellation ratio[69] = $\frac{w_q^H R_n w_q}{w^H R_n w}$, where w_q is a quiescent vector, w is the calculated coil combination weights, and R_n is the covariance matrix for interference. We also compared phase consistency along cross-section lines on phase images.

2.2.6 Feasibility of Beamforming-Based Coil Combination in Motion-Resolved Free-Breathing MRI

The beamforming-based method can also be compatible with compressed sensing reconstruction by using the obtained coil combination weights as the coil sensitivity maps. We reconstructed self-gated free-breathing liver PDFF and R_2* maps using motion-resolved

reconstruction and different coil combination methods. The optimization problem for the motion-resolved reconstruction is:

$$x^* = argmin_x \|FSx - y\|_2^2 + \lambda_1 TV^{motion}(x) + \lambda_2 \sum_{echo,state} \left\| Wavelet(x_{echo,state}) \right\|_1 \quad \text{(Eq. 2-6)}$$

where F represents the non-uniform fast Fourier Transform (NUFFT) operator, S denotes beamforming-based coil combination weights, x is the reconstructed multi-echo images, y is the acquired k-space data, and λ_1 and λ_2 are regularization parameters. The regularization parameters were chosen manually to balance between undersampling artifact reduction and image sharpness. The PDFF and R_2* maps were calculated by fitting to a 7-peak fat model[70] with a single R_2* decay term.

2.3 Results

Figures 2-2 and 2-3 compare the magnitude and phase of the first-echo coil-combined images using different methods. Max-SIR beamforming resulted in phase jumps that do not come from phase wraps (red arrows in the figures). The proposed MVDR beamforming provide consistent phase information as in results from adaptive coil combination. A small patch size of 5x5 for calculation of signal covariance matrices can be sufficient for artifact suppression in magnitude images. However, the experimental results showed that a larger patch size (e.g., 17x17) is required for suppressing streaking artifacts in phase images.

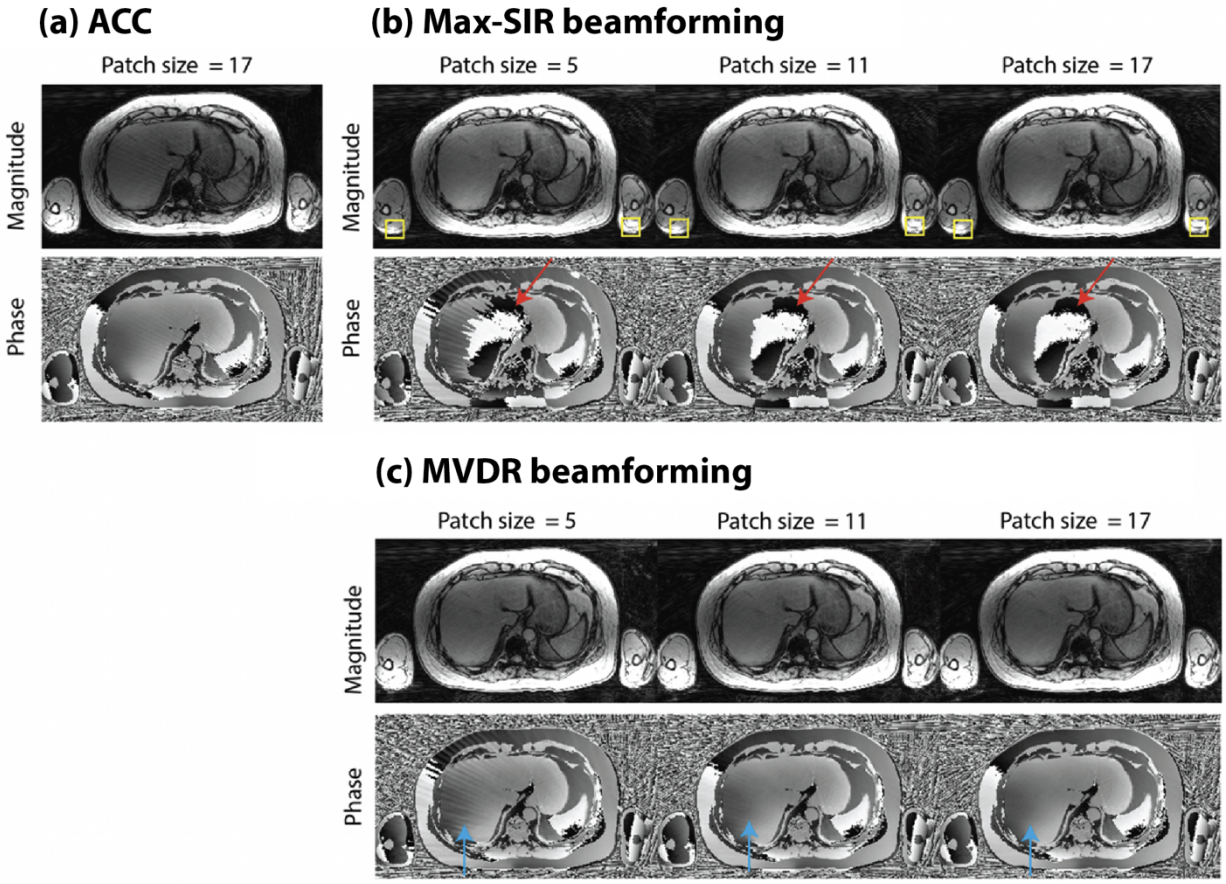

Figure 2-2. Coil-combined magnitude and phase images using **(a)** the adaptive coil combination, **(b)** the max-SIR beamforming, and **(c)** the proposed MVDR beamforming. Yellow boxes represent the patches automatically identified for interference covariance matrix calculation. The same patches were used for max-SIR beamforming and MVDR beamforming. Max-SIR beamforming results show rapid-changing phase (red arrows) variation. A larger patch size is needed to reduce streaking artifacts in phase images (blue arrows).

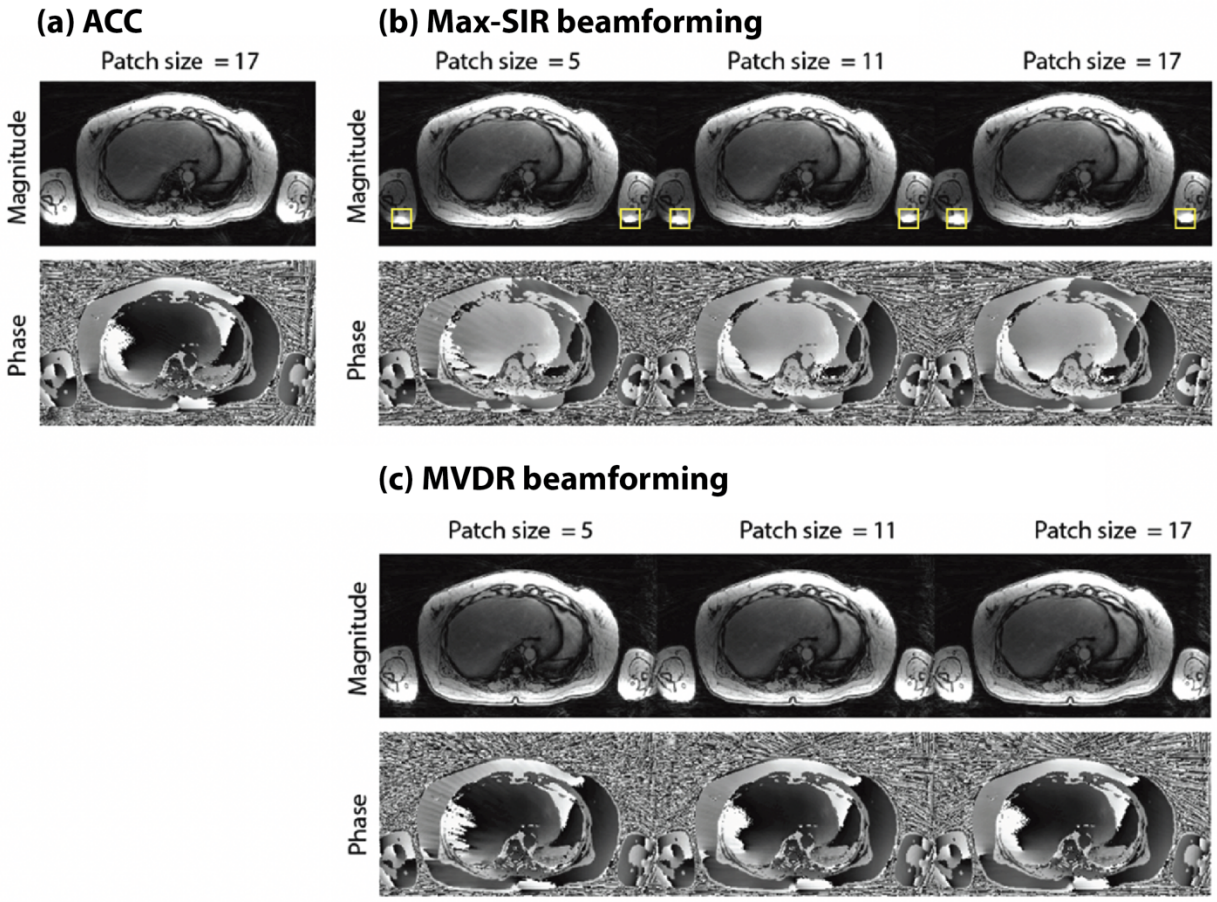

Figure 2-3. Another comparison of coil-combined magnitude and phase images using **(a) the** adaptive coil combination, **(b)** the max-SIR beamforming, and **(c)** the proposed MVDR beamforming. A smaller patch size is sufficient for suppress streaking artifacts in magnitude images. However, residual streakings can still be observed in results using a smaller patch size.

Figure 2-4 compares the phase profiles from different reconstruction methods. In this case, an unnatural phase jump can be observed in the max-SIR beamforming results. The MVDR beamforming has a similar phase profile as the adaptive coil combination results, and with less streaking artifacts in the phase images.

Figure 2-5 compares the cancellation ratio for these 3 methods. Both max-SIR and MVDR beamforming showed increased cancellation ratio, demonstrating improved streaking artifact suppression performance.

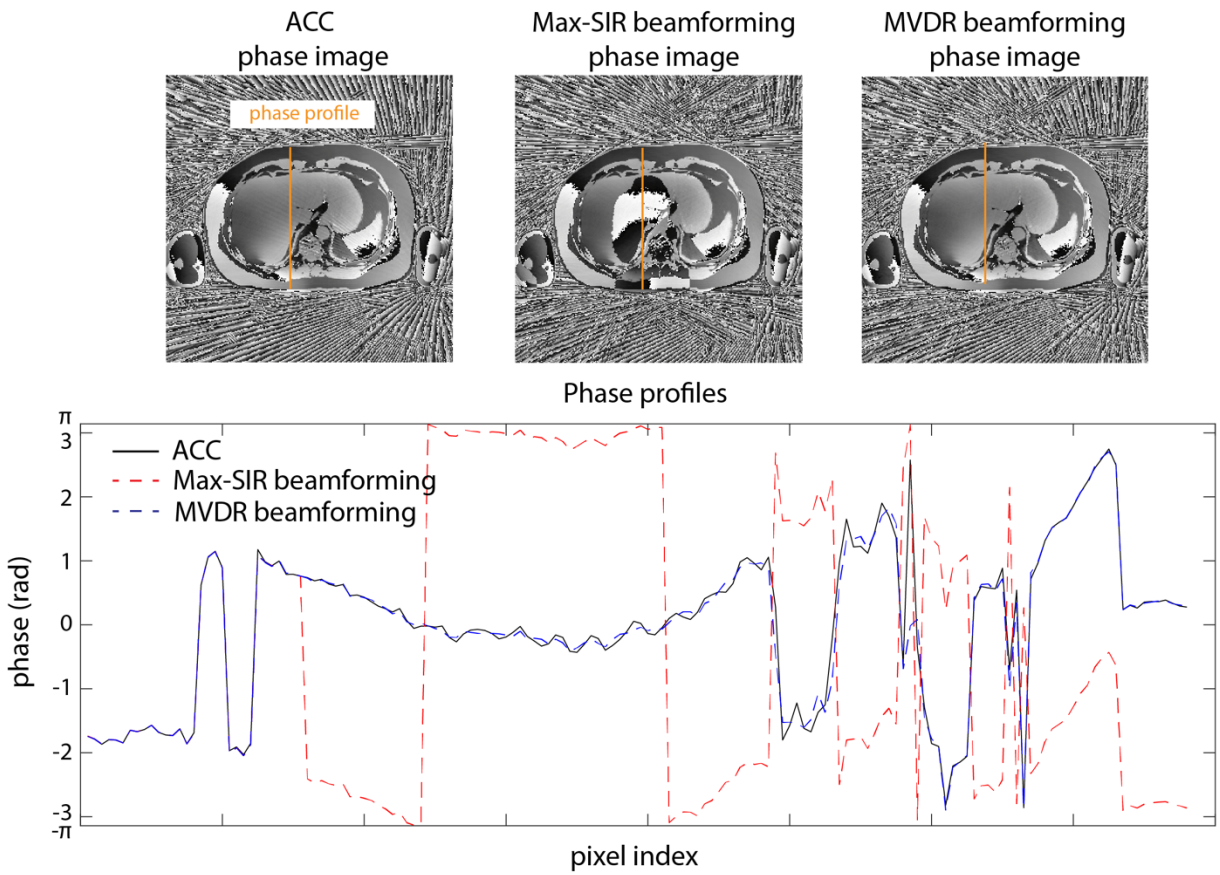

Figure 2-4. Phase profiles in phase images from ACC, Max-SIR beamforming and MVDR beamforming.

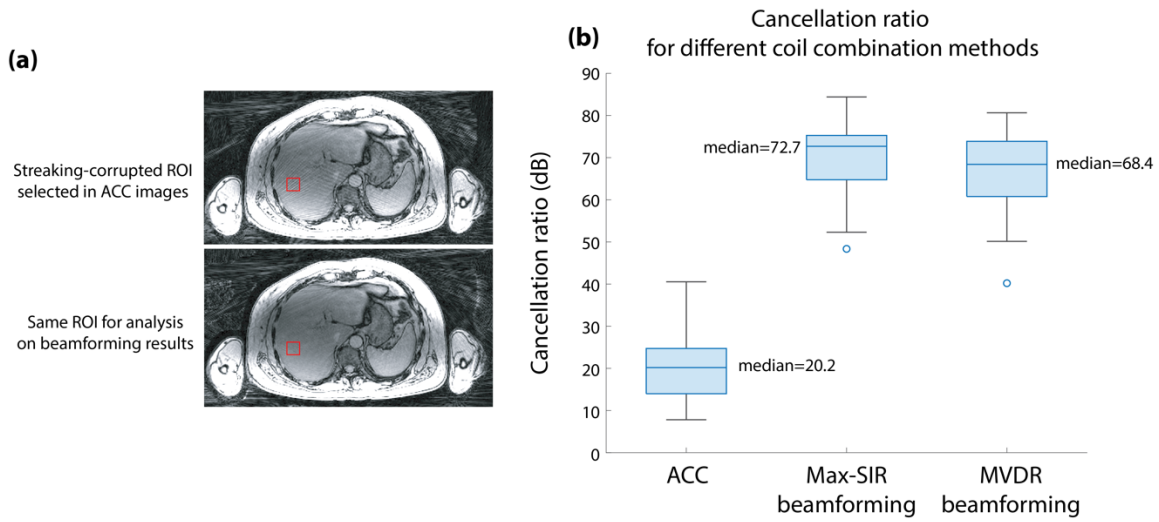

Figure 2-5. Box plot for cancellation ratios in different coil combination methods.

The streaking artifacts from the arms are evident with radial undersampling and motion self-gating[32] (red arrows) (**Figure 2-6**). Using beamforming instead of conventional adaptive coil combination suppresses the streaking specifically from the arms (orange arrows). When using motion-resolved reconstruction (reconstructed with optimization problem in Eq. 2-6) with conventional adaptive coil combination, the specific artifact patterns from the arms cannot be fully suppressed (blue arrows) and can affect PDFF and R_2* quantification accuracy. Combining compressed sensing and beamforming generated images and quantitative maps with most of the streaking artifacts suppressed (green arrows).

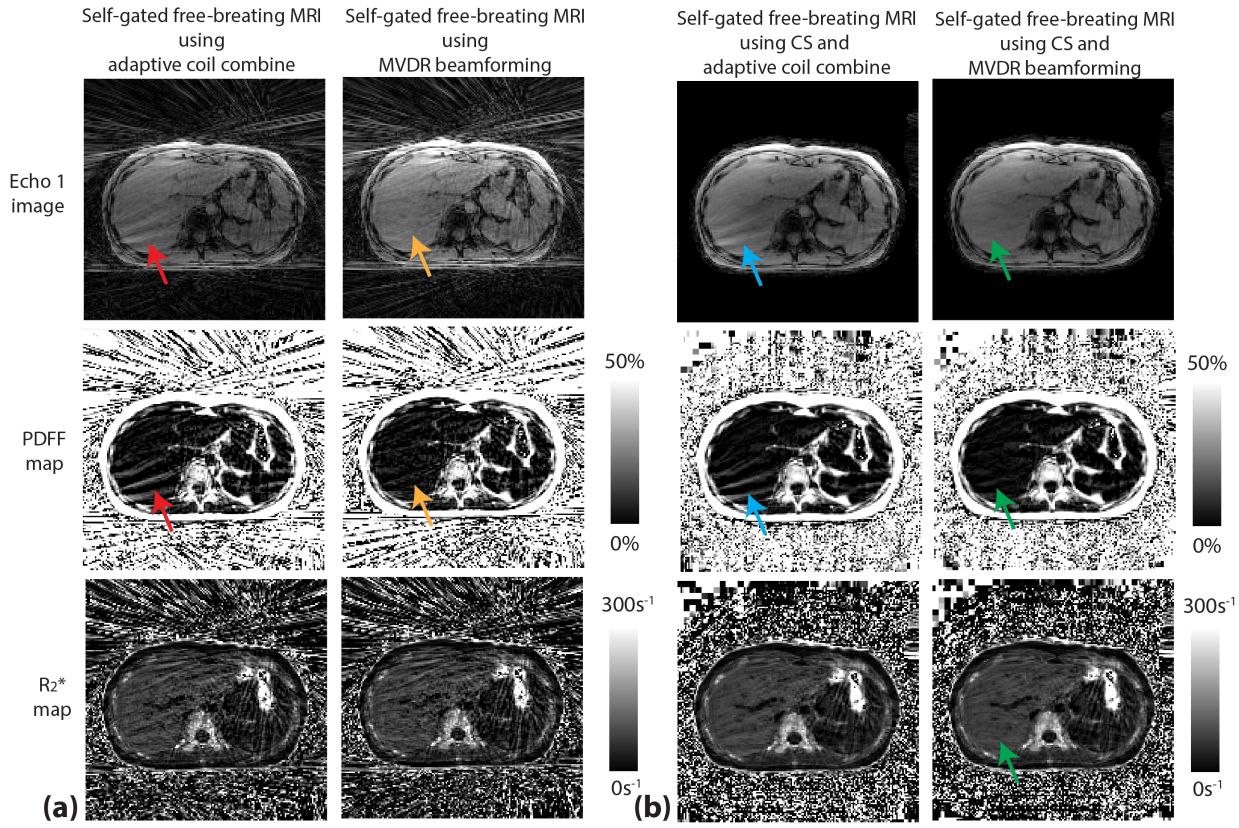

Figure 2-6. Images and PDFF/R_2* maps using different reconstruction methods. **(a)** Results from self-gated free-breathing MRI using conventional adaptive coil combination and the proposed MVDR beamforming pipeline. **(b)** Results from motion-resolved CS reconstruction using conventional adaptive coil combination and the proposed beamforming pipeline.

2.4 Discussion

Compared with previous works that only investigated beamforming-based streaking reduction in magnitude images using radial MRI acquisitions, we investigated beamforming on both magnitude and phase images and proposed a different beamforming formulation that preserves consistent phase information. Although the performance of interference suppression decreased a little for the MVDR beamformer compared with the max-SIR beamformer in terms of cancellation ratio, MVDR provides consistent phase information that is important in phase-sensitive applications.

We found that magnitude and phase images have different sensitivities to the patch size for signal covariance matrix calculation. The streaking reduction performance in the magnitude images is similar from patch sizes 5x5 to 17x17. Since a larger patch size requires longer computational time, a small patch size will be sufficient if only magnitude images are required. On the other hand, a larger patch size is required to effectively suppress the streaking artifacts in the phase images. The computational bottlenecks for these coil combination methods are the repeated calculations of singular value decomposition. The use of parallel processing and high-performance hardware can reduce the computational time.

The automatic interference patch selection pipeline is suitable for abdominal scans with standard axial planes where the streaking artifacts usually come from the arms. For abdominal scans with sagittal, coronal, or oblique planes and for scans in other body parts, different deep learning segmentation models may be trained to automatically select the interference patches. Even without an automatic patch selection method, the MVDR beamforming method can still be applied to suppress the streaking with manual identification of the interference patches.

The proposed beamforming-based coil combination method for streaking reduction can be easily adapted to different reconstruction methods, including constrained reconstruction or deep learning-based reconstruction, by replacing the coil sensitivity maps with the calculated beamforming coil combination weights. Further investigation on streaking reduction performance in different radial MRI applications, especially in phase-sensitive applications, will be investigated in the future.

2.5 Conclusion

In this study, we proposed a 3D phase-preserving beamforming-based coil combination method with an automatic interference patch selection pipeline for coil combination in radial MRI. The proposed method effectively suppressed streaking artifacts from system imperfections while providing robust phase information.

Part of this work has been published or included in work under review:

[1] **Shu-Fu Shih**, Holden H. Wu, "A Beamforming-Based Coil Combination Method to Reduce Streaking Artifacts and Preserve Phase Fidelity in Radial MRI", ISMRM 2022 London. #1697

[2] **Shu-Fu Shih**, Sevgi Gokce Kafali, Kara L. Calkins, Holden H. Wu. "Uncertainty-Aware Physics-Driven Deep Learning Network for Free-Breathing Liver Fat and R_2* Quantification using Self-Gated Stack-of-Radial MRI". Magnetic Resonance in Medicine 2023; 89(4): 1567-85. doi: 10.1002/mrm.29525

[3] **Shu-Fu Shih**, Sevgi Gokce Kafali, Timoteo I. Delgado, Kara L. Calkins, Holden H. Wu. "Accelerated Free-Breathing Liver Fat and R_2* Quantification using Non-Rigid Motion Compensated Compressed Sensing Reconstruction". (*In preparation*)

CHAPTER 3

Uncertainty-Aware Physics-Driven Deep Learning Network for Free-Breathing Liver Fat and R_2* Quantification

3.1 Introduction

Chronic liver disease is a global health burden[71-73]. Liver disease is characterized by histological changes that include hepatic steatosis, inflammation, fibrosis, and iron deposition[16,74-79]. Progressive liver disease is associated with cirrhosis and hepatocellular carcinoma, and can culminate in liver failure[80]. Biopsy is considered the standard technique for diagnosing liver diseases. However, biopsy suffers from sampling bias, is invasive, and is associated with complications[12].

MRI evaluates hepatic steatosis and iron overload by quantifying proton-density fat fraction (PDFF) and R_2*, using chemical-shift-encoded multi-echo Dixon techniques that acquire and fit data to a signal model that accounts for the multi-peak fat spectrum and R_2* component[81]. Conventional Dixon techniques using a multi-echo 3D Cartesian sequence[26] are sensitive to motion and require breath-holding (10-20 sec). The breath-holding requirement limits the volumetric coverage and resolution, and can be challenging for patients[82]. Recently, a multi-echo 3D stack-of-radial technique[32,57] has been developed for free-breathing liver PDFF and R_2* quantification and demonstrated accurate results in subjects with non-alcoholic fatty liver disease (NAFLD)[36]. To compensate for respiratory motion in free-breathing radial data acquisition, self-gating is used to reconstruct images from a subset of data with consistent motion behavior. However, motion self-gating introduces radial undersampling artifacts in the images and quantitative maps. These artifacts can be mitigated by acquiring more radial spokes[83] or using

constrained reconstruction[84], but these strategies require a longer acquisition and/or computational time.

Accurate and rapid signal fitting is another challenge in PDFF and R_2* quantification. Due to the non-convex structure of the signal model and ambiguities in resonant frequencies of water/fat protons with respect to B_0 field variations, signal fitting can converge to a local minimum solution and lead to fat-water swaps. State-of-the-art graph-cut (GC)-based methods[85,86] impose smoothness constraints on the field map and use optimization algorithms to reduce the occurrence of fat-water swaps. However, the GC-based algorithms are computationally expensive with computation time on the order of 10 sec/slice[85].

Compared with iterative constrained reconstruction methods for MRI, such as compressed sensing (CS)[35,87], deep learning (DL)-based methods can rapidly enhance or reconstruct images from undersampled data by leveraging datasets from prior scans. Previous studies have developed novel DL networks for MRI enhancement or reconstruction from undersampled Cartesian data[88,89]. Although there were DL networks developed for undersampled radial MRI[90-93], there is a lack of investigation regarding multi-echo radial MRI for PDFF and R_2* mapping. On the other hand, DL has also been used to replace the computationally expensive fat-water signal fitting process. Different network architectures[94-97] and loss functions[98] have been proposed to separate fat/water signals or generate PDFF/R_2* maps. However, these methods only investigated fully-sampled Cartesian data and did not consider radial acquisition nor data undersampling.

Developing, evaluating, and translating DL-based methods for quantitative MRI parameter mapping can be challenging because quantification errors can be difficult to detect by visual inspection. Confidence levels of quantification accuracy from the DL network outputs

were not typically characterized in previous studies[94-98]. Recently, there have been initial developments in incorporating uncertainty estimation in the DL networks for MR image reconstruction[99-101]. These works showed promise by investigating the relationships between estimated uncertainty scores and reconstruction errors. A recent work showed promising results of using uncertainty estimation for quantitative MRI PDFF maps obtained from DL[102]. The study indicated that the uncertainty scores were related to the noise levels in the input data. However, the relationship between the uncertainty scores and quantification accuracy was not established.

In this work, we developed an uncertainty-aware physics-driven deep learning network (UP-Net) that can rapidly calculate accurate liver PDFF and R_2* maps using multi-echo images from undersampled self-gated free-breathing stack-of-radial MRI data. UP-Net simultaneously 1) suppressed radial streaking artifacts due to undersampling after self-gating, 2) calculated accurate quantitative liver PDFF and R_2* maps, and 3) provided pixel-wise uncertainty maps for each quantitative parameter within a rapid inference time <100 ms/slice. We calibrated the UP-Net uncertainty scores and demonstrated the ability to predict liver PDFF and R_2* quantification errors using the uncertainty scores.

3.2 Methods

3.2.1 Uncertainty-Aware Physics-Driven Deep Learning Network (UP-Net)

We proposed UP-Net (**Figure 3-1**) to generate accurate quantitative maps from undersampled 2D multi-echo images and provide pixel-wise uncertainty maps which can be used to predict quantification errors. UP-Net contained two concatenated network modules for artifact suppression and parameter mapping. The first module took 2D multi-echo undersampled images x as the input and generated enhanced 2D multi-echo images $\hat{m}$ with suppressed undersampling

artifacts. For x and $\hat{m}$, multi-echo images, including both the real and imaginary components, were stacked along the channel dimension. The second module transformed $\hat{m}$ to quantitative parameter maps $\hat{p}$ and their corresponding uncertainty maps $\hat{u}$. In our case of multi-parameter fitting, $\hat{p}$ and $\hat{u}$ are 3D tensors where different 2D quantitative maps are stacked along the channel dimension. UP-Net requires reference multi-echo images and reference quantitative maps for training. Details regarding reference data generation are described in section **3.2.5**.

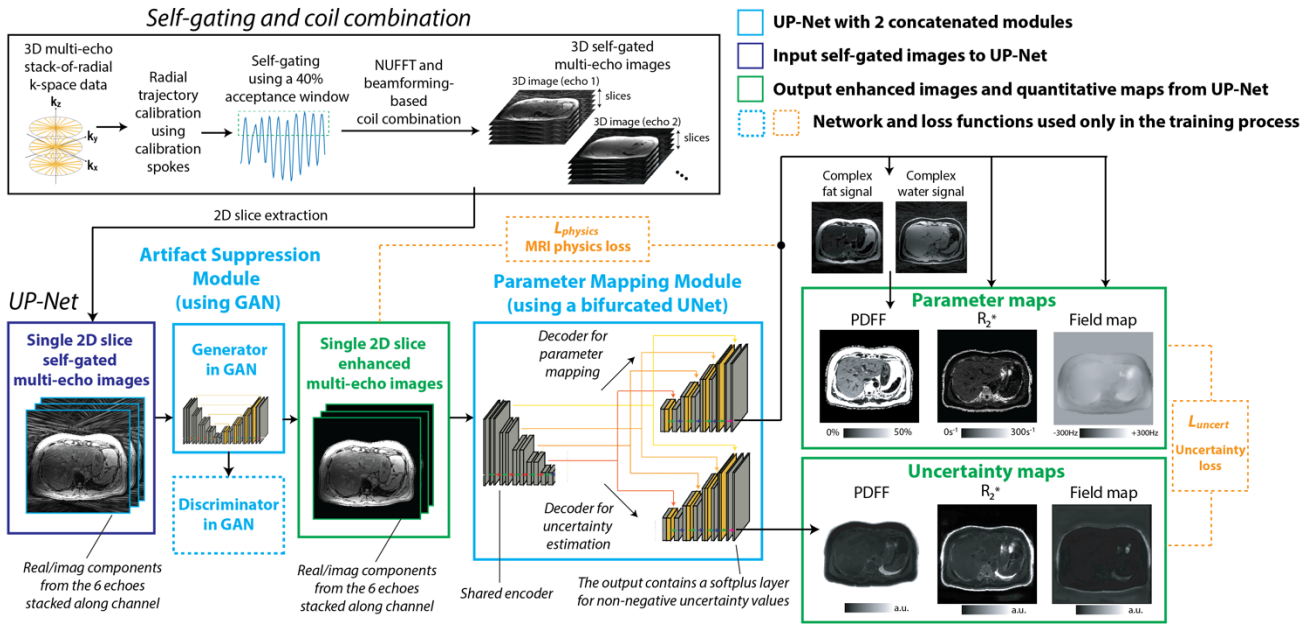

Figure 3-1. The proposed uncertainty-aware physics-driven deep learning network (UP-Net) for rapid free-breathing proton-density fat fraction (PDFF) and R_2* quantification from self-gated multi-echo stack-of-radial MR images. The artifact suppression module used a generative adversarial network (GAN) architecture to reduce the radial undersampling artifacts due to self-gating. The parameter mapping module used a bifurcated UNet structure, which had a shared encoder and two decoders, to calculate parameter maps (pixel-wise means) and uncertainty maps (pixel-wise variances). NUFFT: non-uniform fast Fourier transform.

Convolutional neural networks (ConvNet) have been proposed to effectively suppress artifacts from undersampling[24-29]. Recently, there are works showing that generative adversarial networks (GAN) can improve the quality of the reconstructed images for radial MRI compared

to conventional ConvNet[103,104]. We used a GAN architecture for the artifact suppression module. The generator was implemented using a 2D UNet architecture[68], and the discriminator was implemented using the architecture proposed in[105]. To deal with image contrast variation across subjects, instance normalization[106] was used in both the generator and the discriminator. A detailed diagram for the UP-Net implementation is presented in **Figure 3-2**.

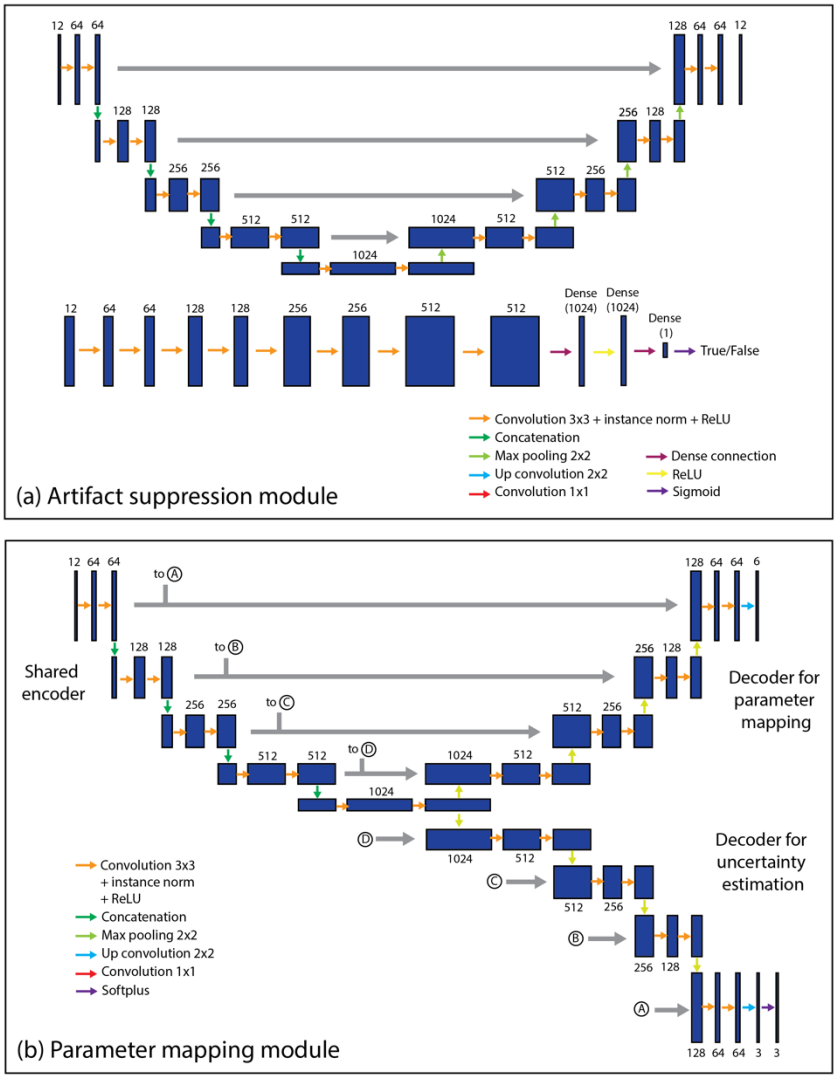

Figure 3-2. Network architectures for the **(a)** artifact suppression module and **(b)** parameter mapping module in UP-Net.

We considered the quantitative parameter output as distributions which can be characterized using pixel-wise means $\hat{p}$ and pixel-wise variances $\hat{u}$ from a Bayesian perspective[107,108]. We interpreted $\hat{p}$ and $\hat{u}$ as the quantitative maps and the corresponding uncertainty maps. For each pixel index j, a larger value of $\hat{u_j}$ indicates a wider spread of the distribution and therefore the associated $\hat{p_j}$ has higher uncertainty. By assuming a prior data distribution, the network can be trained to predict $\hat{p}$ and $\hat{u}$ simultaneously using the loss function introduced in section **3.2.2**. In light of the deeply correlated nature of $\hat{p}$ and $\hat{u}$, we used a "bifurcated UNet" architecture (**Figures 3-1 and 3-2**) for the parameter mapping module. This architecture has one shared encoder that extracts features from multi-contrast images $\hat{m}$, and two separate decoders that generate parameter maps $\hat{p}$ and uncertainty maps $\hat{u}$. Because the uncertainty score, or the variance of a distribution, should always be nonnegative, a softplus layer ($Softplus(x) = \log(1 + e^x)$) was added prior to the uncertainty map output.

3.2.2 Loss Function for UP-Net Training

We constructed a loss function with 5 components for supervised training of UP-Net:

$$L_{UP-Net} = w_1 L_{imgMSE} + w_2 L_{imgGAN} + w_3 L_{mapMSE} + w_4 L_{physics} + w_5 L_{uncert} \quad \text{(Eq. 3-1)}$$

An image mean square error (MSE) loss was used to measure the errors between enhanced ($\hat{m}$) and reference (m) multi-echo images:

$$L_{imgMSE} = \frac{1}{N_j}\sum_j \left(\hat{m}_j - m_j\right)^2 \quad \text{(Eq. 3-2)}$$

, where j represents the pixel index and N_j is the total number of pixels in the multi-echo images. We trained the GAN architecture using a Wasserstein GAN loss[109], which can be formulated as:

$$\min_G \max_D \mathbb{E}_{m\sim p_{train}(m)}[D(m)] - \mathbb{E}_{\hat{m}\sim p_G(\hat{m})}[D(G(\hat{m}))] \quad \text{(Eq. 3-3)}$$

, where G represents the generator, D represents the discriminator. The loss for updating the generator G was:

$$L_{imgGAN} = \mathbb{E}_{\hat{m}\sim p_G(\hat{m})}[D(G(\hat{m}))] \qquad \text{(Eq. 3-4)}$$

We also used an MSE loss that measures the errors between quantitative maps from UP-Net ($\hat{p}$) and reference data (p):

$$L_{imgMSE} = \frac{1}{N_j}\sum_j(\hat{p}_j - p_j)^2 \qquad \text{(Eq. 3-5)}$$

To promote learning of the signal fitting process we used an MRI physics loss:

$$L_{physics} = \frac{1}{N_j}(\hat{m} - Q(\hat{p}))^2 \qquad \text{(Eq. 3-6)}$$

where Q represents an operator that transforms the quantitative maps to multi-echo images based on the MRI signal equation. In this work where we investigated PDFF and R_2* quantification, the operator Q we used was:

$$Q(\hat{p}) = Q(W, F, R_2^*, \varphi, TE) = \left(W + F \cdot \left(\sum_{m=1}^{M} a_m \cdot e^{i2\pi f_m TE}\right)\right) \cdot e^{-R_2^* TE} \cdot e^{i2\pi\varphi TE} \quad \text{(Eq. 3-7)}$$

where W, F, R_2^*, φ represent the quantitative water maps, fat maps, R_2* maps, and B_0 field maps. A 7-peak fat model[70] with amplitudes a_m and frequencies f_m were also included. To predict quantitative parameter outputs with corresponding uncertainty scores, we used an uncertainty loss:

$$L_{uncert} = \frac{\|\hat{p}-p\|_1}{\hat{u}} + log(\hat{u}) \qquad \text{(Eq. 3-8)}$$

This uncertainty loss function is equivalent to performing maximum a posteriori (MAP) inference where a Laplace distribution[107] is assumed for each quantitative parameter in each pixel. We can also understand this loss function from a more intuitive perspective. First, in regions where the $\|\hat{p} - p\|_1$ error minimization is difficult (e.g., regions with lower signal-to-noise ratio), increased values of $\hat{u}$ can reduce the loss, therefore capturing uncertainty. Second,

the $log(\hat{u})$ term can serve as a regularization term to avoid unconstrained increase in the uncertainty score.

The relative weights for each loss component in Equation 1 can impact the results. We chose the weight combination that achieved the lowest PDFF and R_2* quantification errors in the validation set: $w_1 = 0.2$, $w_2 = 0.2$, $w_3 = 0.2$, $w_4 = 0.3$, and $w_5 = 0.1$.

3.2.3 Training Strategy for UP-Net

To shorten the convergence time for training UP-Net, we used a step-by-step training strategy.

Step 1: Pre-train the artifact suppression module using pairs of input undersampled images x and reference images m as the training data and using only L_{imgMSE} and L_{imgGAN} for the loss function.

Step 2: Pre-train the parameter mapping module without the uncertainty estimation path using pairs of reference multi-contrast images m and reference quantitative maps p as the training data and using only L_{mapMSE} and $L_{physics}$ for the loss function.

Step 3: Load the weights trained from **Steps 1** and **2**, and then train the entire UP-Net end-to-end without the uncertainty path using L_{imgMSE}, L_{imgGAN}, L_{mapMSE} and L_{model} for the loss function (i.e., not including the uncertainty loss term yet).

Step 4: Train the entire UP-Net using training sets of undersampled images x, reference images m and reference quantitative maps p with the full loss function L_{UP-Net}.

For all training steps, data augmentation for images/maps was performed by mirroring (no flip or horizontal flip) and rotating by n*90 degrees (n=0,1,2,3). This augmented the training data size to 8 times that of the original training data. In addition, we used a “phase

augmentation" strategy to further augment training data by adding a phase offset to the multi-echo input images, multi-echo reference images, and reference fat and water complex signals at the same time (**Figure 3-3**). The signal magnitudes were not changed, and the relationship between images and quantitative maps were not modified. In each epoch during training, we generated 3 more instances for each 2D slice in this manner (i.e., in addition to the original data, 3 different phase offsets were applied to generate 3 more instances). The phase offsets were randomly selected between $0\sim2\pi$. This strategy aimed to improve robustness to phase variations, which is important in separating fat/water signals.

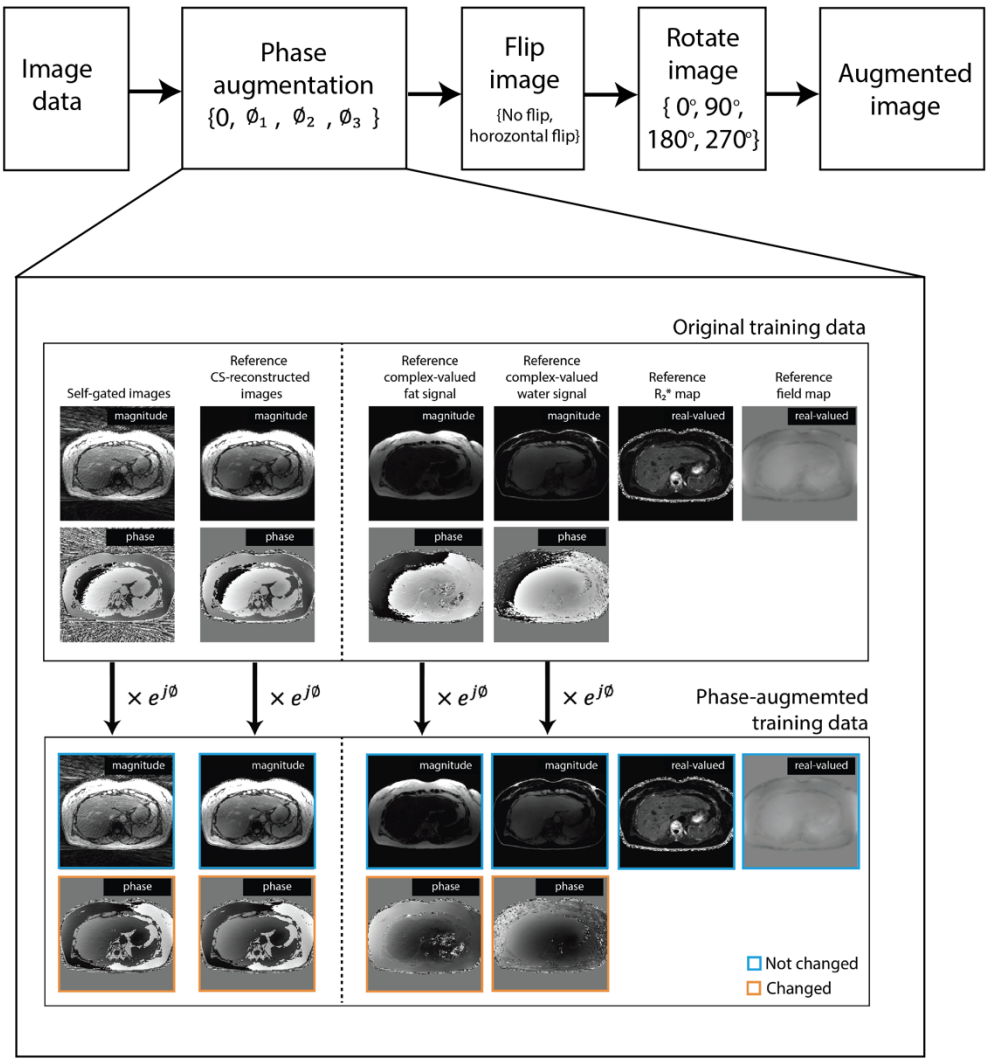

Figure 3-3. Overview of the data augmentation strategy used in this work. For phase augmentation, a phase offset (ϕ) was added to 1) self-gated images, 2) reference compressed sensing (CS)-reconstructed images, 3) reference complex-valued fat signal and 4) reference complex-valued water signal to generate phase-augmented training data. Signal magnitudes were not modified. R_2* and field map values were not changed. In each epoch during training, 3 more instances (in addition to the original data) were generated by using 3 random phase offsets ϕ_1, ϕ_2 and ϕ_3 in the range of [0, 2π].

3.2.4 Data Acquisition

In a HIPAA-compliant and IRB-approved study, we acquired MR images from 105 subjects, including healthy subjects and subjects with suspected or confirmed NAFLD, at 3T (MAGNETOM Skyra or Prisma, Siemens Healthineers, Erlangen, Germany). Fifty-seven of the

subjects were adults (34 females, 23 males; age 48.16±19.01 years; body mass index [BMI]: 26.98±5.94kg/m^2) and 48 of the subjects were children (19 females, 29 males; age 13.06±2.99 years; BMI: 22.85±8.41kg/m^2). Written informed consent, parental permission, and assent, if applicable, were obtained for all subjects prior to research procedures. We scanned using a prototype free-breathing multi-echo gradient-echo 3D stack-of-radial sequence with bipolar readout gradients (**FB Radial**, parameters in **Table 3-1**)[57]. To compare with standard breath-holding techniques, we acquired an additional breath-hold bipolar multi-echo gradient-echo 3D Cartesian sequence (**BH Cartesian**, parameters in **Table 3-1**)[26]. We separated the data into training (N=63), validation (N=21), and testing (N=21) datasets using a 3:1:1 ratio (**Table 3-2**). Subject information and data were entered into a secure database for management and analysis[110].

We trained and tested UP-Net using only FB Radial data, while the BH Cartesian data served as an external reference for evaluation of PDFF and R_2* quantification accuracy. For BH Cartesian data, images and the quantitative PDFF and R_2* maps were reconstructed using vendor-provided software on the scanner.

Table 3-1. Representative sequence parameters for free-breathing 3D stack-of-radial (FB Radial) and breath-holding (BH) 3D Cartesian axial MRI scans at 3T. N/A: not applicable.

Sequence parameters	FB Radial	BH Cartesian
TE (ms)	1.23, 2.46, 3.69, 4.92, 6.15, 7.38	
TR (ms)	8.85	
Flip angle (°)	5	5
Field of view	360-440 x 360-440 mm^2	360-440 x 360-440 mm^2
Slice thickness (mm)	5	5
Matrix size (x, y, z)	224-288, 224-288, 40-72	224-288, 224-288, 30-40
Acceleration factor	N/A	*R*=4 (parallel imaging)
Radial spokes	354-454	N/A
Scan time (min:sec)	2:28 - 4:49*	0:19#
Retrospective undersampling	*R*=2.5 (40% self-gating acceptance rate)	N/A

*Radial gradient calibration time was not included. #Prescan calibration time was not included.

Table 3-2. Dataset characteristics. NAFLD: non-alcoholic fatty liver disease. Std: standard deviation.

Datasets	Total number of subjects	Adult subjects	Pediatric subjects	Total number of 2D slices	Range of liver PDFF values
Training set	63	24 NAFLD, 11 healthy	18 NAFLD[#], 10 healthy	2528*	Min: 0.4% Max: 33.4% Mean: 10.5% Std: 9.7%
Validation set	21	7 NAFLD, 4 healthy	6 NAFLD[#], 4 healthy	812	Min: 0.9% Max: 28.4% Mean: 9.2% Std: 8.8%
Testing set	21	7 NAFLD, 4 healthy	5 NAFLD[#], 5 healthy	860	Min: 0.6% Max: 25.2% Mean: 9.8% Std: 8.4%

*Before performing data augmentation. See text in section 3.2.3 for details about data augmentation. [#]Suspected or confirmed NAFLD.

3.2.5 Reference Data Preparation for UP-Net Training

UP-Net was trained in a supervised approach, which demands high-quality multi-echo images and quantitative maps with minimal artifacts to serve as references. However, it is challenging to acquire fully-sampled data for reconstruction of motion-resolved 3D volumetric images in the abdomen. To satisfy the Nyquist sampling criteria after self-gating, longer acquisition time is needed, which may increase sensitivity to motion effects. Previous works have used CS to generate images and quantitative maps for DL network training in applications where a fully-sampled reference dataset is difficult to acquire[111,112]. Following a similar strategy, we acquired nominally fully-sampled stack-of-radial data before applying motion self-gating, and used CS to reconstruct motion self-gated images with suppressed undersampling artifacts.

The workflow for generating the training data for UP-Net is shown in **Figure 3-4**. Gradient delays were calibrated to correct the radial trajectory for FB Radial data

reconstruction[16]. We extracted a projection-based self-navigator from the $k_x = k_y = 0$ line in k-space[35] to track respiratory motion along the z dimension. A sliding window approach was applied along the motion dimension to bin the k-space data into 6 respiratory motion states where each bin contained 40% of the entire k-space data (effective data undersampling factor = 2.5 in each state). We estimated coil sensitivity maps using the phased array beamforming technique developed in Chapter 2[113], which has been shown to suppress radial artifacts resulting from system imperfections (e.g., gradient non-linearity and B_0 field inhomogeneity). We formulated the 2D CS reconstruction problem as[35]:

$$x^* = argmin_x \|FSx - y\|_2^2 + \lambda_1 TV^{motion}(x) + \lambda_2 \sum_{echo,state} \left\| Wavelet(x_{echo,state}) \right\|_1 \quad \text{(Eq. 3-9)}$$

where F represents the non-uniform fast Fourier Transform (NUFFT) operator, S denotes coil sensitivity maps, x is the reconstructed multi-echo images, y is the acquired k-space data, and λ_1 and λ_2 are regularization parameters. The regularization parameters were chosen manually to balance between undersampling artifact reduction and image sharpness. After CS reconstruction, we calculated quantitative maps (including complex fat/water components, R_2* map, and B_0 field map) by fitting the CS-reconstructed multi-echo images to a 7-peak fat model[70] with a single R_2* component (same as Eq. 3-7) using GC-based algorithms[85,86]. Local fat-water swaps still occurred in certain slices and were difficult to correct using GC-based algorithms; we excluded these slices from the training dataset. We generated body masks from the first-echo CS-reconstructed magnitude images, and applied the body masks to the CS-reconstructed images and the corresponding quantitative maps for background artifact and noise suppression. We will refer to the reference CS-reconstructed self-gated free-breathing stack-of-radial images as

FB+CS and the corresponding quantitative maps reconstructed by GC-based algorithms as FB+CS+GC.

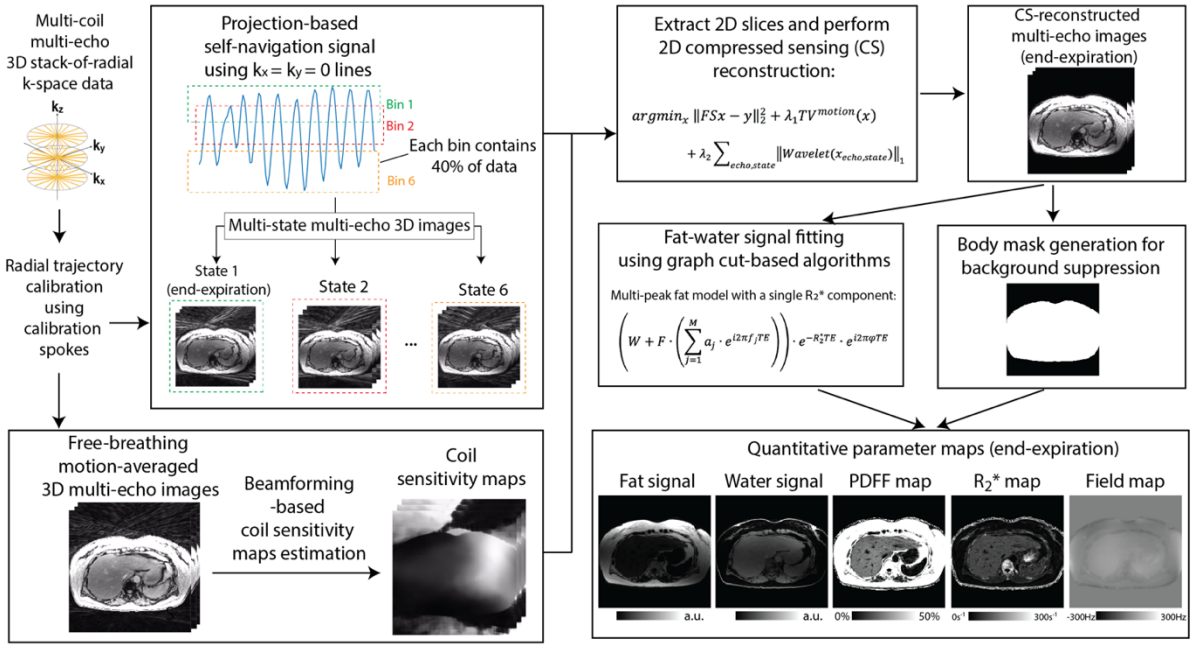

Figure 3-4. The workflow for generating reference data (multi-echo images and quantitative maps) for training UP-Net. Nominally fully-sampled stack-of-radial k-space data were binned into 6 respiratory motion states using projection-based self-navigators. A 2D compressed sensing (CS) framework with beamforming-based coil sensitivity maps was used to reconstruct multi-echo images with reduced undersampling streaking artifacts. Quantitative maps were generated by fitting the multi-echo images to a fat-water signal model with a single R_2* component. Body masks were generated from the CS-reconstructed first-echo images for background suppression.

The input images x to UP-Net were coil-combined 6-echo images using 40% of FB Radial data near the end-expiration state (**Figure 3-1**). The real and imaginary components from each echo were stacked along the channel dimension (6 echoes × real/imaginary components = 12 channels). The output from the artifact suppression module had the same data dimensions as the input images (12 channels), and were fed into the parameter mapping module. The output from the parameter mapping module contained 1) complex-valued fat and water components,

R_2* map, and field map stacked along the channel dimension and 2) three uncertainty maps for PDFF, R_2*, and field map stacked along the channel dimension. PDFF maps were generated from complex fat/water components for calculation of L_{mapMSE} and L_{uncert}, while the complex-valued fat/water components were directly used in L_{model}.

Based on PDFF and R_2* quantification accuracy in the validation dataset, the hyperparameters for the end-to-end UP-Net training were chosen as: batch size=32, initial learning rates=0.0001, and epochs=150, using the Adam optimizer.

3.2.6 Evaluation of UP-Net Image Quality and Quantification Accuracy

We evaluated the performance of UP-Net in terms of image quality and quantification accuracy of the output images and maps in the testing dataset. For image quality, we compared the enhanced image results from UP-Net with the reference FB+CS images using normalized root mean squared error (NRMSE) and structure similarity index (SSIM). For quantification accuracy, we calculated differences in PDFF and R_2* quantification results using liver regions of interest (ROIs) for 1) FB+UP-Net versus FB+CS+GC and 2) FB+UP-Net versus BH Cartesian. ROIs with area of 5-cm^2 were placed in the right lobe of the liver by a trained researcher while avoiding large vessels and bile ducts[36]. A total of 3 ROIs were placed in the upper, middle and lower liver (one ROI at each level) for each subject. Bland-Altman analysis was performed to evaluate PDFF and R_2* accuracy by calculating the mean difference (MD) and 95% limits of agreement (LoA) between different methods.

3.2.7 Evaluation of UP-Net Uncertainty Estimation

We evaluated the performance of UP-Net uncertainty estimation in terms of its ability to predict quantification errors according to the following steps.

Step 1: Complete UP-Net training.

Step 2: In the validation dataset, measure 1) quantification errors ($\sum_{i\in ROI}|\hat{p}_i - p_i|$) between UP-Net and reference FB+CS+GC results and 2) UP-Net uncertainty scores in the liver ROIs. Use a linear correlation model to generate "calibration curves" between quantification errors and UP-Net uncertainty scores for each quantitative parameter separately. Calculate Spearman correlation coefficients and test for statistical significance.

Step 3: Output UP-Net uncertainty scores for liver ROIs in the testing dataset. Transform UP-Net uncertainty scores to predicted quantification errors using the calibration curves.

Step 4: Perform Bland-Altman analysis on predicted quantification errors versus actual quantification errors in the testing dataset, with respect to FB+CS+GC results, for each quantitative parameter separately.

3.2.8 UP-Net Ablation Study

We performed an ablation study to assess the contributions of the key components used in UP-Net, including phase augmentation, GAN loss, MRI physics loss, uncertainty estimation, and joint end-to-end training strategy. After training each ablated model with the same training dataset, we compared the results in the testing dataset using NRMSE and SSIM for image quality, and absolute errors in liver PDFF and R_2* for quantification accuracy. We used the Wilcoxon signed-rank test to evaluate if the performance of the ablated network models had significant difference versus the performance of UP-Net. $P<0.01$ was considered significant.

3.3 Results

3.3.1 UP-Net Image Quality and Quantification Accuracy

Figure 3-5 shows representative first-echo magnitude and phase images from UP-Net input, UP-Net output results, and FB+CS results in two subjects with NAFLD (a 47-year-old male and a 17-year-old male). UP-Net suppressed the radial undersampling streaking artifacts in the liver and in the background (arrows in **Figure 3-5**), and achieved high SSIM compared with FB+CS. **Figures 3-6** and **3-7** show representative quantitative PDFF, R_2* and field map results in axial and coronal orientations and the corresponding uncertainty maps in two NAFLD subjects (same subjects as in **Figure 3-5**). UP-Net generated accurate PDFF/R_2*/field maps compared with FB+CS+GC references in the liver ROIs. Most regions show low quantification errors (**Figures 3-6** and **3-7**) in all 3 quantitative parameters. Regions corresponding to air usually had large quantification errors. The uncertainty maps show high intensities (red arrows in **Figures 3-6** and **3-7**) and characterize the lower confidence in these regions in air.

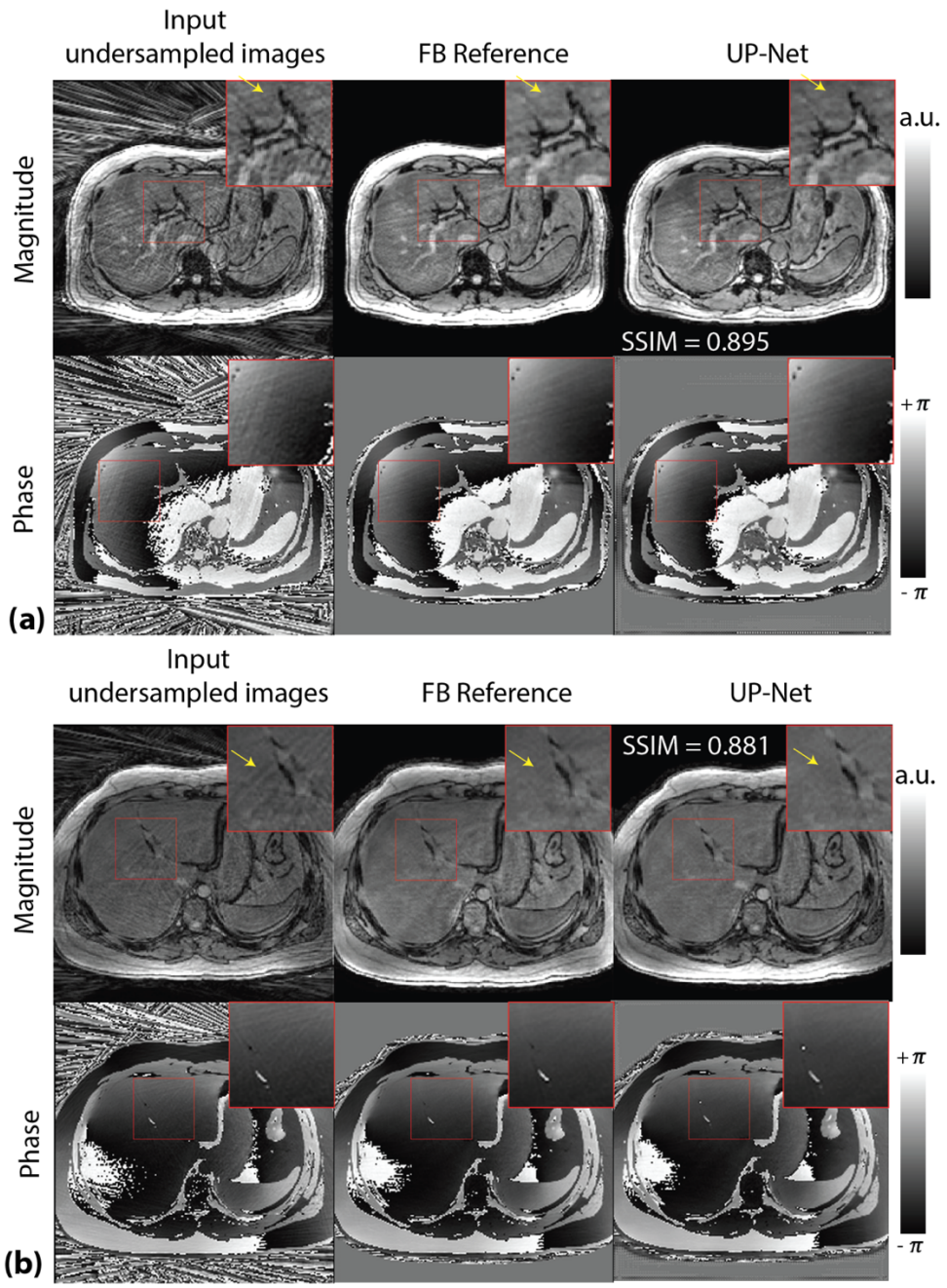

Figure 3-5. Representative free-breathing (FB) stack-of-radial first-echo images from self-gated input images, UP-Net output results, and reference images reconstructed by compressed sensing (CS). **(a)** Results from a 47-year-old male (BMI=28.0kg/m^2) in the testing set. **(b)** Results from a 17-year-old male (BMI=30.4kg/m^2) in the testing set. Structural similarity index (SSIM) values comparing UP-Net output with reference images are shown. Arrows point to streaking artifacts in the self-gated images that are suppressed in the UP-Net output and reference images. BMI: body mass index.

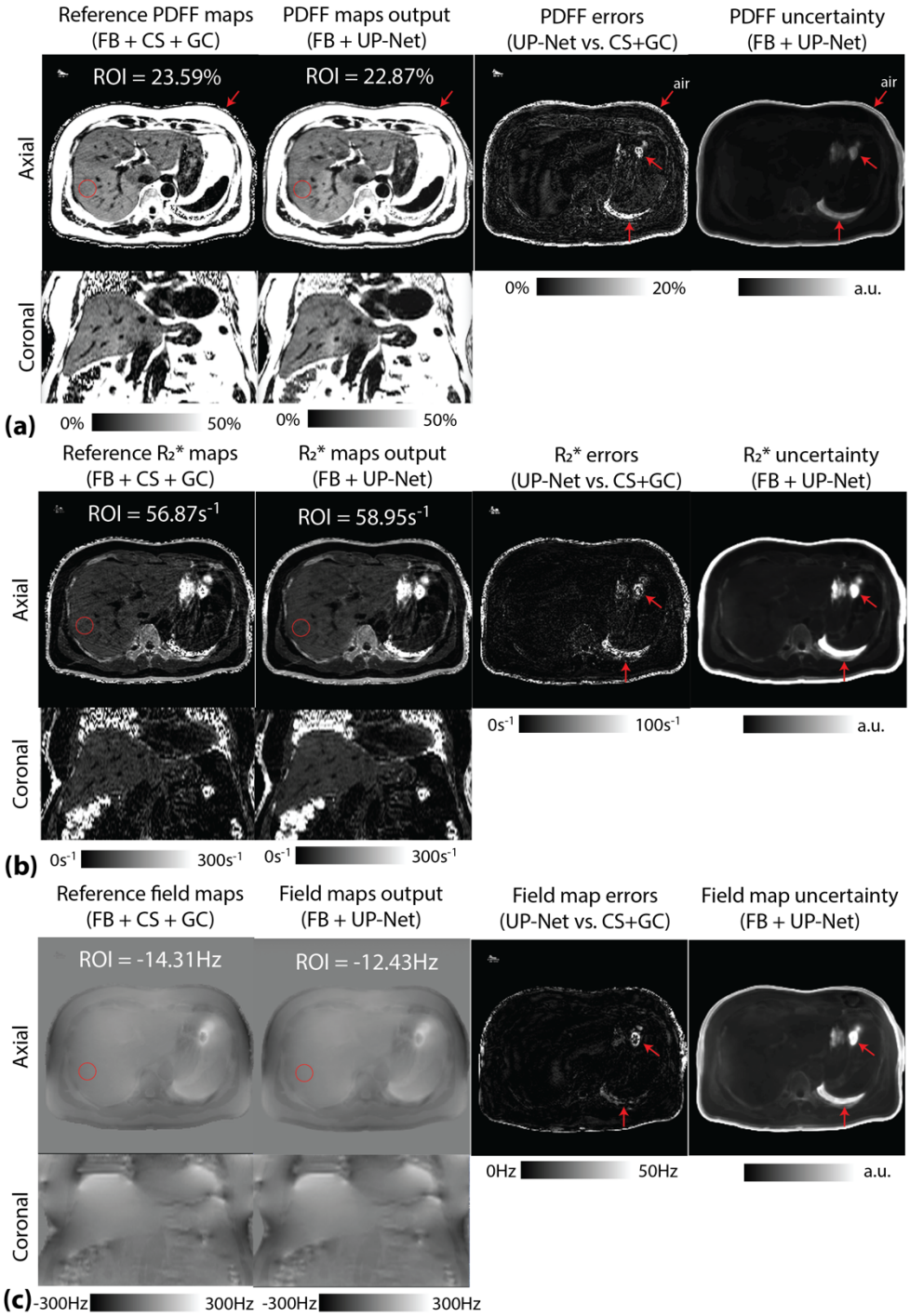

Figure 3-6. Representative free-breathing (FB) **(a)** proton-density fat fraction (PDFF), **(b)** R_2* and **(c)** field maps and corresponding uncertainty maps from the same subject in **Figure 3-5(a)**. PDFF, R_2* and field map errors were generally low when comparing UP-Net results with reference maps reconstructed using compressed sensing (CS) and graph-cut (GC) algorithms. In regions with larger quantification errors, higher UP-Net uncertainty scores were observed in all 3 quantitative maps (red arrows). Errors and higher uncertainty scores around the body were in regions corresponding to air.

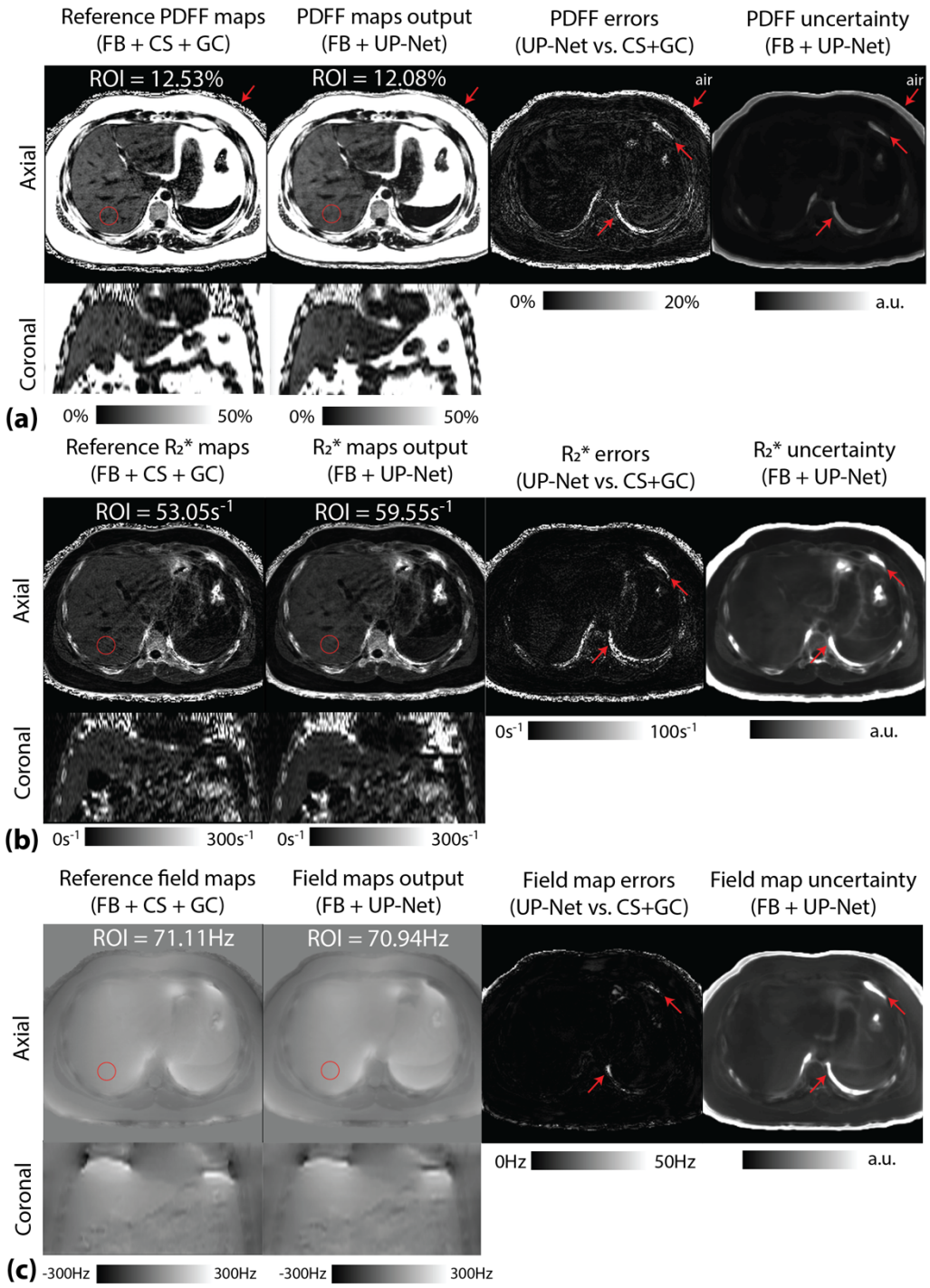

Figure 3-7. Representative free-breathing (FB) **(a)** proton-density fat fraction (PDFF), **(b)** R_2* and **(c)** field maps and corresponding uncertainty maps from the same subject in **Figure 3-5(b)**. PDFF, R_2* and field map errors were generally low when comparing UP-Net results with reference maps reconstructed using compressed sensing (CS) and graph-cut (GC) algorithms. In regions with larger quantification errors, higher UP-Net uncertainty scores were observed in all 3 quantitative maps (red arrows). Errors and higher uncertainty scores around the body were in regions corresponding to air.

Bland-Altman plots for liver PDFF and R_2* quantification accuracy are shown in **Figure 3-8**. For PDFF quantification, FB+UP-Net achieved MD = -0.36% compared with FB+CS+GC, and MD = 0.53% compared with BH Cartesian. For R_2* quantification, FB+UP-Net achieved MD = -0.37 s^{-1} compared with FB+CS+GC, and MD = 6.75 s^{-1}compared with BH Cartesian. LoA between FB+UP-Net versus FB+CS+GC was narrower than FB+UP-Net versus BH Cartesian for both PDFF and R_2* quantification.

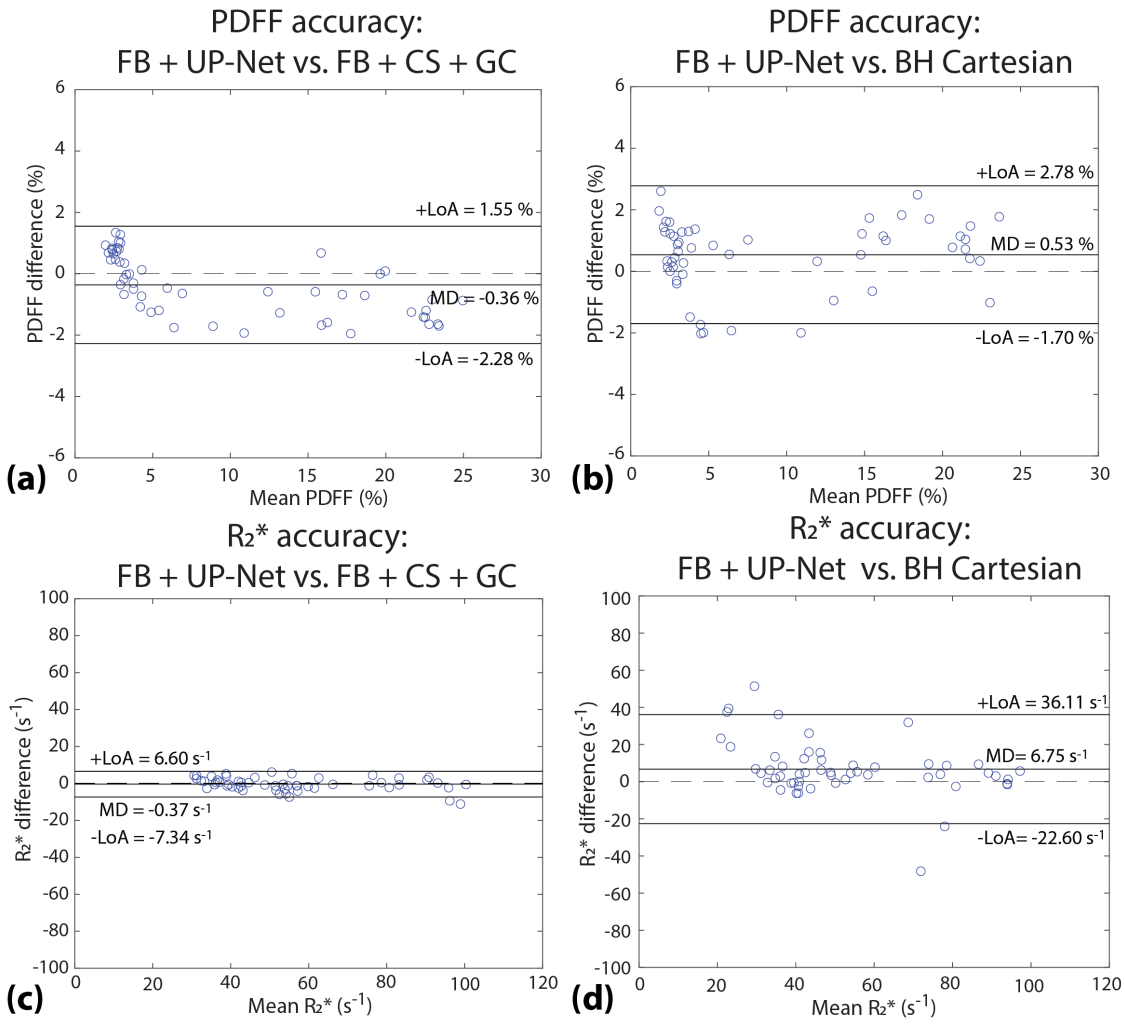

Figure 3-8. **(a-b)** Bland-Altman plots comparing liver proton-density fat fraction (PDFF) values from UP-Net output maps versus free-breathing (FB) reference maps and breath-holding (BH) Cartesian maps. **(c-d)** Bland-Altman plots comparing liver R_2* values from UP-Net output maps versus FB reference maps and BH Cartesian maps. The dashed lines represent zero difference. The solid lines represent mean differences (MD) and 95% limits of agreements (LoA).

3.3.2 UP-Net Uncertainty Estimation

Linear correlation results comparing absolute quantification errors versus uncertainty scores of three quantitative parameters in liver ROIs in the validation dataset are shown in **Figure 3-9(a)**. The Spearman correlation coefficients for PDFF, R_2* and field map were 0.358 ($p<0.05$), 0.466 ($p<0.01$), and 0.503 ($p<0.01$), respectively. These calibrated linear regression curves were used to convert uncertainty scores measured in the testing dataset to predicted quantification errors. The Bland-Altman plots for UP-Net predicted errors versus actual quantification errors in liver ROIs are shown in **Figure 3-9(b)**. MDs between UP-Net predicted errors versus actual absolute quantifications errors were 0.27%, 0.12 s^{-1}, and 0.19 Hz for PDFF, R_2*, and field map, respectively. Note that the quantification errors were all generally low to begin with.

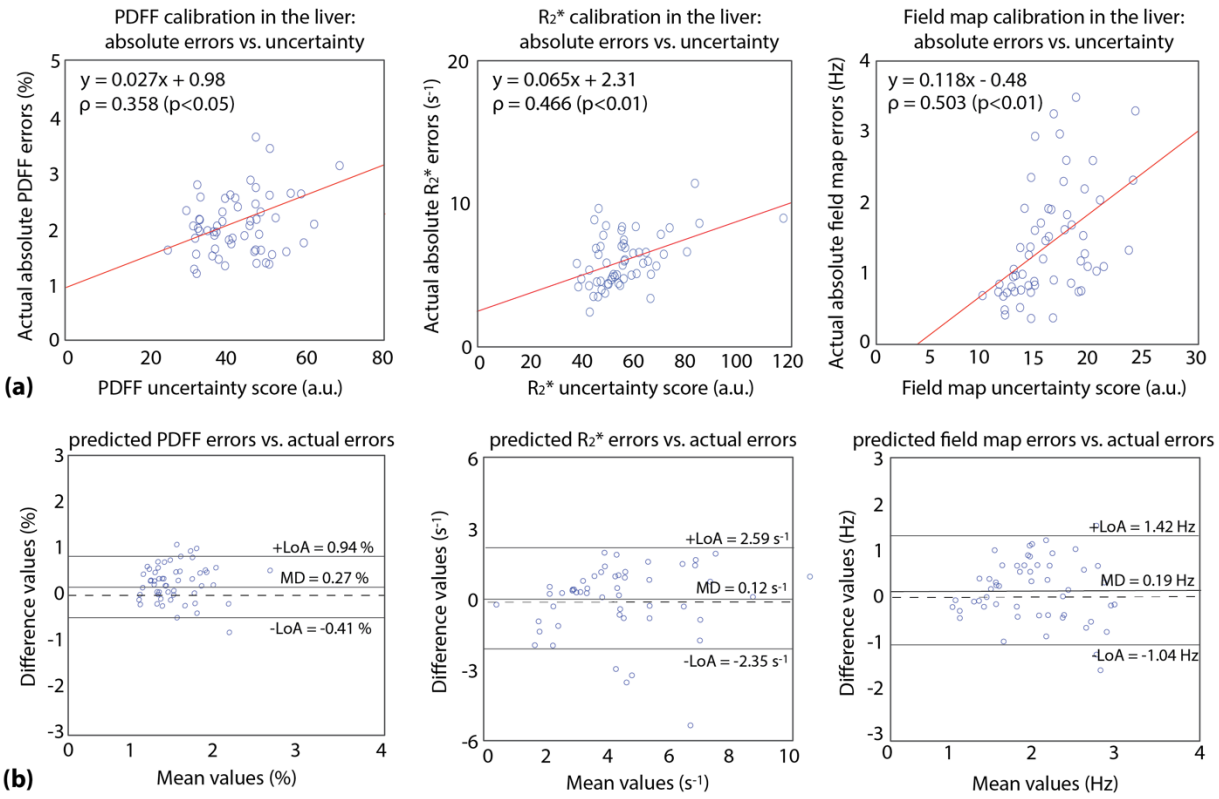

Figure 3-9. **(a)** Correlation plots between absolute quantification errors (UP-Net outputs versus reference compressed sensing and graph-cut fitting results) and UP-Net uncertainty scores in liver regions of interest (ROIs) in the validation dataset. Linear regression was performed to calibrate PDFF, R_2* and field map uncertainty scores with respect to the absolute errors. **(b)** Bland-Altman plots comparing the errors predicted from UP-Net uncertainty scores versus the actual absolute quantification errors in PDFF, R_2* and field map in liver ROIs in the testing dataset. The black dashed lines represent zero difference. The black solid lines represent mean differences (MD) and 95% limits of agreements (LoA).

3.3.3 UP-Net Ablation Study Results

Table 3-3 shows the results of our ablation study. UP-Net achieved higher mean SSIM of 0.872 and lower mean NRMSE of 0.173 compared with the ablated UP-Net models without phase augmentation or GAN loss (all $p<0.01$). Compared with the ablated UP-Net model without the MRI physics loss, UP-Net achieved lower mean PDFF error of -0.36% and lower mean R_2* error of -0.37 s^{-1} (both $p<0.01$). UP-Net without uncertainty estimation did not have significant

difference in image quality and quantification accuracy when compared with UP-Net (i.e., the addition of the uncertainty path did not degrade quantification accuracy). UP-Net without joint training achieved higher mean PDFF error of -0.46% ($p<0.01$) compared to UP-Net with joint training.

Table 3-3. Ablation study in the testing dataset for different components used in UP-Net. Structural similarity index (SSIM) and normalized root mean squared error (NRMSE) were evaluated on magnitude images, with respect to compressed sensing results. Proton-density fat fraction (PDFF) and R_2* quantification errors were evaluated in liver regions of interest, with respect to compressed sensing and graph-cut fitting results. Results are reported as mean ± standard deviation. * represents statistically significant difference ($p<0.01$, Wilcoxon signed-rank test) compared with UP-Net.

	Component					Metric			
Network	Phase Augmentation	GAN Loss	Physics Loss	Uncertainty Estimation	Joint Training	SSIM	NRMSE	PDFF Errors	R_2* Errors
1		✓	✓	✓	✓	0.851± 0.055*	0.182± 0.048*	-0.92%± 0.95%*	-0.54s^{-1}± 3.02s^{-1}*
2	✓		✓	✓	✓	0.858± 0.067*	0.194± 0.053*	-0.31%± 1.05%	-0.68s^{-1}± 3.46s^{-1}*
3	✓	✓		✓	✓	0.870± 0.049	0.178± 0.050	-1.69%± 1.49%*	-2.50s^{-1}± 5.03s^{-1}*
4	✓	✓	✓		✓	0.877± 0.048	0.176± 0.042	-0.29%± 0.88%	-0.34s^{-1}± 3.81s^{-1}
5	✓	✓	✓	✓		0.884± 0.050	0.168± 0.061	-0.46%± 1.47%*	-0.41s^{-1}± 3.02s^{-1}
UP-Net	✓	✓	✓	✓	✓	0.872± 0.053	0.173± 0.059	-0.36%± 0.98%	-0.37s^{-1}± 3.56s^{-1}

3.3.4 Processing and Reconstruction Time

Data preparation steps of gradient calibration, self-gating, NUFFT, and beamforming-based coil combination (**Figures 3-1** and **3-2**) required a total time of 30 sec/slice. Repeated forward and inverse NUFFT are the bottleneck for the CS reconstruction method. To improve computational performance, we implemented the CS reconstruction method using GPU-based NUFFT packages[58]. CS reconstruction took 3 min/slice on an Intel Xeon E5-2660 CPU with 128GB RAM and an NVIDIA v100 GPU with 32GB memory. We used the ISMRM fat-water toolbox[59] and code from previous works[21] for GC fitting algorithms, which required 15 seconds/slice on the same CPU. UP-Net required 28 hours to train on an NVIDIA v100 GPU

with 32GB memory. With the prepared data as input, UP-Net took 79 msec/slice for network inference (using same hardware as network training). A more detailed analysis of the total operation counts for each method was provided in **Table 3-4**.

Table 3-4. Comparison of the number of floating-point operations (FLOPs) for reconstructing one slice using different methods. The compressed sensing (CS) algorithm used in this work was implemented using conjugate gradient descent. The graph-cut based fitting algorithm was implemented using code from the ISMRM fat-water toolbox. The CS algorithm is an iterative method and the FLOPs count is based on the average iteration number used in this work. Number of FLOPs for UP-Net was calculated using the ptflops package (https://pypi.org/project/ptflops/) and the number of FLOPs for CS and graph-cut algorithm were calculated with the help of the Lightspeed Matlab Toolbox (https://github.com/tminka/lightspeed).

	Compressed sensing	Graph cut-based fitting algorithm	UP-Net
FLOPs	60.2 G	1.8 G	15.64 G

3.4 Discussion

We developed an uncertainty-aware physics-driven deep learning network that accurately quantifies liver PDFF and R_2* using undersampled self-gated free-breathing multi-echo stack-of-radial MRI. Compared with previous works on DL-based fat/water separation and/or R_2* mapping[94-98], our study has two main contributions. First, we investigated a DL approach for PDFF and R_2* mapping from undersampled radial MRI data. Unlike previously proposed networks that learned mapping from fully-sampled Cartesian images to fat/water signals or quantitative maps[94-98], UP-Net generates accurate quantitative maps from images impacted by radial undersampling artifacts. We incorporated artifact suppression and parameter mapping into one end-to-end network. This substantially reduced the computational time for image artifact suppression compared to time-intensive CS methods and fat-water signal fitting compared to GC algorithms. Second, our proposed network has built-in uncertainty estimation that generates

pixel-wise uncertainty maps for different quantitative parameters. Uncertainty estimation to assess the confidence levels in DL-based MRI reconstruction and quantitative parameter mapping results is a nascent direction[99-102]. We specifically investigated the application of uncertainty estimation in DL-based PDFF and R_2* quantification and demonstrated that a calibration method for the UP-Net uncertainty scores can be used to predict absolute liver PDFF and R_2* quantification errors in UP-Net parameter maps to within 1% and 3 s^{-1}, respectively, compared to actual errors with respect to reference methods.

To suppress radial undersampling streaking artifacts, we used UNet as the backbone architecture, which has been used in previous work for radial streaking reduction in 2D slices[90,91], dynamic 2D cardiac images[93], and 2D images from different respiratory phases[114]. In this work, we adapted the input/output dimensions of UNet to accommodate the 2D multi-echo images. We stacked the real and imaginary components from all of the multi-echo images along the channel dimension to preserve the consistency of the magnitude and phase input information for PDFF and R_2* quantification. We also adopted a GAN architecture and a phase augmentation strategy for image quality improvement. Due to limited memory on the GPU for network training, correlations between neighboring slices were not considered in this study. Networks that can efficiently process multi-echo 2D+slice or multi-echo 3D volumetric data could be further investigated. Although it is possible to omit the artifact suppression module and use one single network to generate quantitative maps directly from self-gated undersampled radial images, UP-Net with a modular architecture can provide more accurate quantitative maps with less radial streaking artifacts (example in **Figure 3-10**).

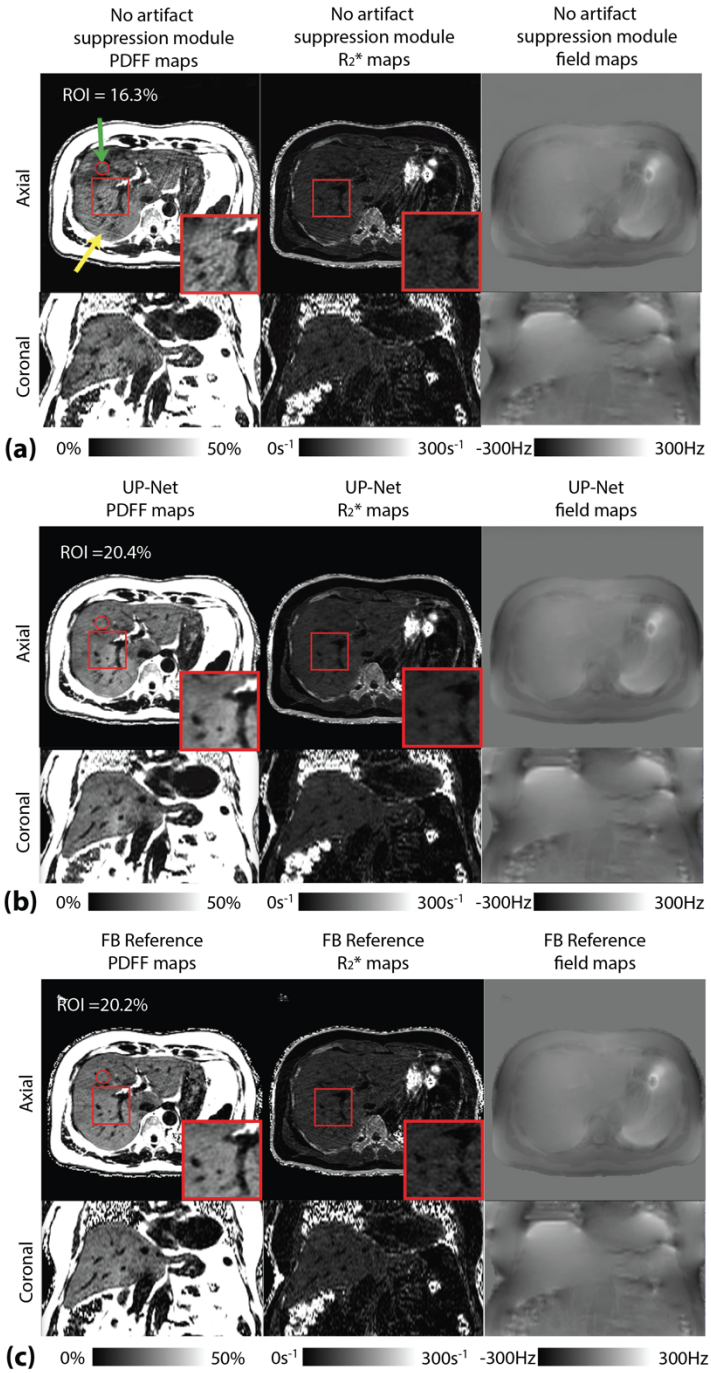

Figure 3-10. Comparison of results from **(a)** UP-Net without an artifact suppression module, **(b)** proposed UP-Net, and **(c)** reference quantitative maps using compressed sensing and graph-cut algorithms. In (a), we trained UP-Net without an artifact suppression module using pairs of self-gated multi-echo images and reference quantitative maps. This approach used a single network to suppress the radial undersampling artifacts and perform parameter mapping at the same time, which can be challenging. We found that the radial streaking artifacts were not adequately suppressed (yellow arrow) and there were PDFF quantification errors (green arrow).

In addition to rapid computational time, another potential advantage of using UP-Net or other DL-based methods for fat-water separation is reducing the occurrence of fat-water swaps. In our datasets, there were slices with local fat-water swaps (usually around the liver dome) using the GC methods. These slices required manually adjusting GC parameters, such as B_0 field map smoothness or range, to address the swaps. When training UP-Net, we excluded data with fat-water swaps and performed phase augmentation, which helped the network to learn reliable fat-water separation in the presence of B_0 field map variations. The use of UP-Net can potentially reduce the occurrence of fat-water swaps (**Figures 3-11**) and avoid the extra time/effort needed to check and fix fat-water swaps.

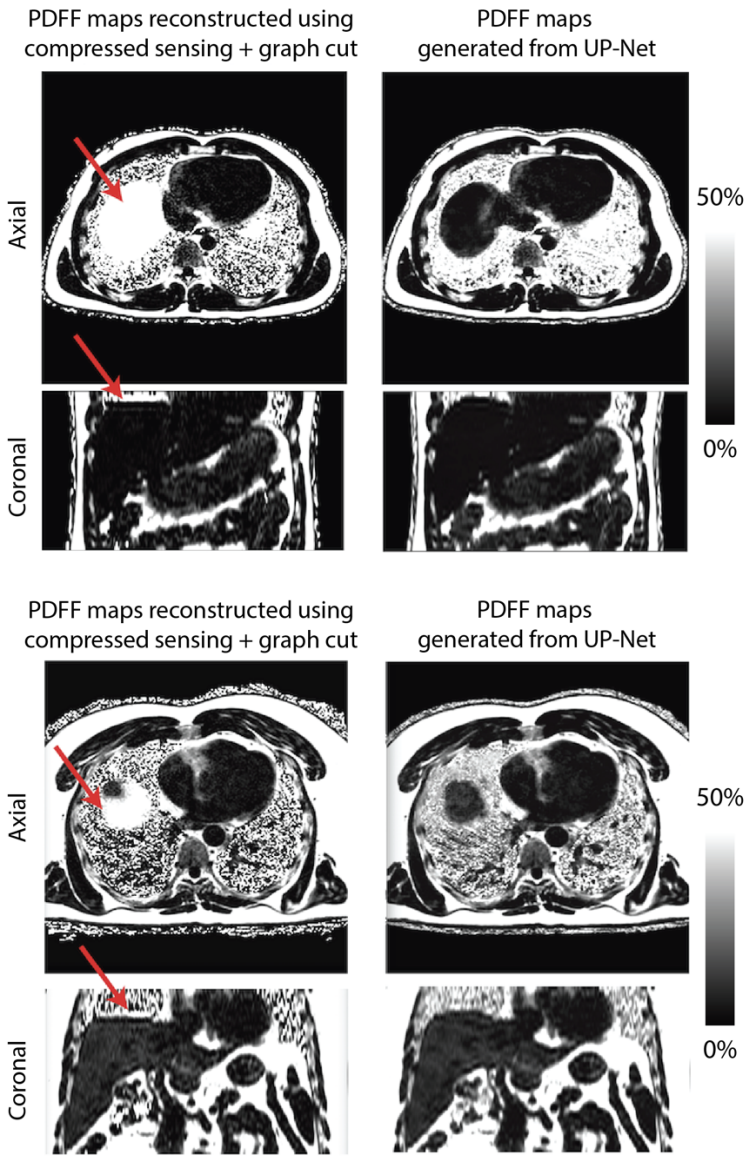

Figure 3-11. Example cases where a graph cut-based method generated PDFF maps with local fat-water swaps and UP-Net generated PDFF maps without fat-water swaps. The local fat-water swaps usually occur near the liver dome in our free-breathing MRI dataset. In these 2D slices, the liver usually occupies a small portion of the field of view and is more likely to result in local fat-water swaps (arrows) using the conventional method (compressed sensing + graph-cut based fitting). In contrast, these slices do not exhibit fat-water swaps in our UP-Net results.

One concern of DL-based fat-water separation is whether the network could perform accurate mapping for datasets with liver PDFF values outside the range in the training dataset.

UP-Net has two advantages that could allow it to generalize to these cases. First, we used an MRI physics loss that will constrain the output to follow the fat-water signal model. Second, even though the training dataset we used in this work has a maximum liver PDFF around 30%, UP-Net still learned from the signal characteristics in fat-dominant tissues (e.g., subcutaneous adipose tissue) with PDFF up to 90%. To investigate this, we created synthetic testing datasets with higher liver PDFF, and used UP-Net to perform PDFF mapping. A representative example in **Figure 3-12** shows that UP-Net can indeed quantify higher liver PDFF values (e.g., >40%) that were not included in the training dataset. Another concern of DL-based fat-water separation is whether the network can be adapted to several different body parts. Although different body parts may have different B_0 field map ranges and variations, their signal characteristics are described by the same fat-water signal model. After training UP-Net on a certain dataset (e.g., liver and upper abdomen), the fat-water signal model is implicitly learned. Through transfer learning and fine tuning, UP-Net can potentially be applied to other body parts (e.g., lower abdomen).

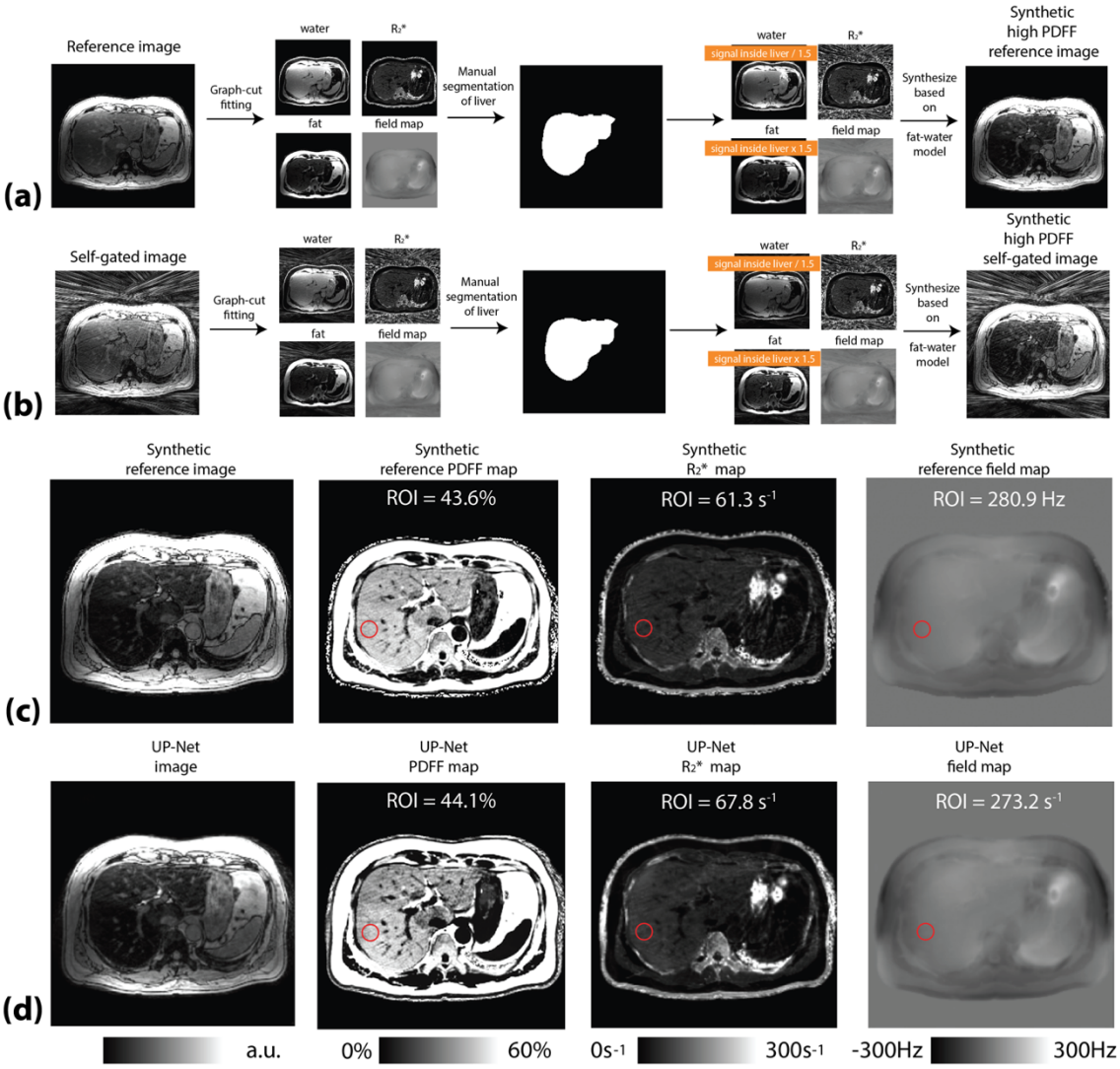

Figure 3-12. (a) Example of a synthetic testing case with higher PDFF. First, we performed parameter mapping from the dataset using a reference method with graph-cut fitting. Next, we multiplied the fat signal component within the liver by 1.5 and divided the water signal component within the liver by 1.5 to synthesize a case with higher liver PFFF (>40%). **(b)** We used the same approach as in (a) to generate corresponding synthetic self-gated images with higher liver PDFF, which were used as inputs to UP-Net. **(c)** Reference images and quantitative maps for the synthetic testing case in (a). **(d)** The UP-Net results for this higher-PDFF synthetic testing case. The quantitative values from the UP-Net results were consistent with the synthetic reference data.

Fully-sampled free-breathing motion-resolved volumetric abdominal stack-of-radial MRI data is often impractical to acquire. We used CS to generate images and quantitative maps with suppressed radial streaking artifacts. CS methods have already been validated for PDFF

quantification using undersampled Cartesian MRI[115] and for PDFF and R_2* quantification using undersampled radial MRI data[84]. For complete evaluation of our UP-Net quantification accuracy, we also compared UP-Net results with standard 3D BH Cartesian MRI. Many previous DL-based fat-water signal fitting methods were only evaluated on individual fat and water maps[94-97]. We evaluated our results on quantitative PDFF maps. Similar to a previous DL-based method for joint PDFF and R_2* mapping using Cartesian MRI[98], we also achieved low biases in PDFF, R_2*, and field map values versus reference methods. Notably, we trained and tested our method on a larger dataset (105 subjects). In contrast, a previous report considered 31 subjects[98]. Previous DL methods did not investigate their results in NAFLD subjects, while our UP-Net was trained and evaluated in a population including healthy subjects and subjects with suspected or confirmed NAFLD. In our Bland-Altman analysis of PDFF and R_2* quantification accuracy, the MD between FB+UP-Net and FB+CS+GC was smaller than the MD between FB+UP-Net and BH Cartesian. This was expected because UP-Net was trained using reference data from the FB+CS+GC method. The MD and LoA of PDFF and R_2* quantification comparing FB+UP-Net versus BH Cartesian are similar to results in previous studies comparing self-gated FB stack-of-radial MRI with BH Cartesian[36].

We carefully examined the contributions from key components in UP-Net, including phase augmentation, GAN loss, and MRI physics loss. Among these components, MRI physics loss was especially important for accurate parameter quantification. From our ablation study, the network without MRI physics loss generated larger biases in both PDFF and R_2* quantification. MRI physics loss considered the relationship between multi-echo signals and quantitative parameters and did not require reference quantitative maps. However, the MRI physics loss alone may not provide sufficient information to resolve fat-water swaps. By adding an MSE loss

for quantitative maps and training with reference non-swapped maps, we directed UP-Net to learn the spatial distribution of fat- or water- dominant pixels and reduce fat-water swaps. In applications that focus on the signal magnitude, phase information in DL results is often discarded or overlooked. Our use of a phase augmentation strategy strengthened UP-Net's ability to learn complex-valued signal relationships by including images with the same magnitude but different phase. This strategy can also be applied in applications that need accurate phase, including temperature mapping and quantitative susceptibility mapping. GAN architectures for imaging tasks is an active research topic. In this work, we used Wasserstein loss in our GAN architecture, which has previously been used in Cartesian MRI reconstruction[116]. More complicated GAN architectures and loss functions designed for medical images[117] could be investigated further.

The "black box" nature of DL-based methods for MRI is an important concern and potential barrier to clinical translation. Uncertainty estimation in DL networks[99-102] presents a promising approach to provide context and assess confidence in DL outputs for clinical applications that demand a high level of numerical accuracy, including the use of quantitative maps for diagnostic decisions. In this study, we showed that with calibration, UP-Net uncertainty scores predicted quantification errors in a separate testing dataset. These promising results have some potential applications. For example, confidence masks can be generated by thresholding the uncertainty scores and then overlaid on the UP-Net quantitative parameter maps. Radiologists can avoid making measurements and decisions in areas with higher uncertainty scores and have more confidence in using DL-generated images and quantitative maps. A recent study has demonstrated that by passing uncertainty information in concatenated tasks, the performance of the downstream task (e.g., segmentation or detection) can be improved[118]. The

uncertainty maps generated by UP-Net can potentially provide information and improve subsequent automatic liver MRI analysis, such as DL-based liver segmentation and disease classification.

This study has limitations. First, we did not investigate the influence of different data undersampling factors on UP-Net performance. We used a 40% data acceptance window (2.5-fold undersampling) on nominally fully-sampled data, as suggested in previous studies[32,36]. Self-gating data acceptance rates can be further reduced to improve motion fidelity. The number of acquired radial spokes can also be reduced to investigate additional scan acceleration. However, higher undersampling factors pose more difficulties in both generating high-quality reference data and training UP-Net. Adjustments such as adding k-space consistency layers[119] might be required for UP-Net to address higher undersampling factors. Second, we trained and tested UP-Net using data with specific number of echoes, TE, TR, and flip angle. These sequence parameters were closely related to PDFF and R_2* accuracy in the data we used. Our current analysis on the quantification accuracy and uncertainty prediction may not be directly applicable in other datasets with different sequence parameters. Third, the calculation of the UP-Net uncertainty loss term required reference quantitative maps. Therefore, the UP-Net uncertainty values reflect differences between UP-Net results and results from reference methods. Fourth, we calibrated the PDFF and R_2* uncertainty estimation in the validation dataset only using ROIs in the liver. This approach required CS and GC reference reconstruction results for calibration. In addition, different calibration curves may be needed to quantify DL uncertainty in other tissues, such as subcutaneous and visceral adipose tissues. Fifth, we used linear regression to investigate the relationship between UP-Net uncertainty scores and quantification errors. However, this approach may not be sufficient to characterize all the factors at play. PDFF measurements are

results of relative amounts of two chemical shift species and can have different inherent uncertainty at different PDFF levels. R_2* uncertainty depends on combinations of the number of echoes, the chosen echo times, and the underlying true R_2* values. Because PDFF and R_2* are incorporated together in the fat-water signal model, multi-variate models can also be considered to improve uncertainty characterization and calibration in the future.

3.5 Conclusion

In this study, we developed an uncertainty-aware physics-driven deep learning network that rapidly calculates accurate liver PDFF and R_2* maps from undersampled free-breathing self-gated multi-echo stack-of-radial images and provides pixel-wise uncertainty maps. GAN architecture, phase augmentation, and MRI physics loss improved the UP-Net image quality and quantification accuracy for liver PDFF and R_2*. We demonstrated that UP-Net uncertainty scores can be used to predict absolute quantification errors in liver PDFF and R_2*.

This work has been published in:

Shu-Fu Shih, Sevgi Gokce Kafali, Kara L. Calkins, Holden H. Wu. "Uncertainty-Aware Physics-Driven Deep Learning Network for Free-Breathing Liver Fat and R_2* Quantification using Self-Gated Stack-of-Radial MRI". Magnetic Resonance in Medicine 2023; 89(4): 1567-85. doi: 10.1002/mrm.29525

CHAPTER 4

Accelerated Free-Breathing Liver Fat and R_2* Quantification using Non-Rigid Motion Compensated Compressed Sensing Reconstruction

4.1 Introduction

MRI-based proton density fat fraction (PDFF)[120,121] can quantify fat content and can be used for non-invasive assessment, monitoring, and management of metabolic dysfunction-associated steatotic liver disease (MASLD)[122], the most common chronic liver disease[123]. On the other hand, R_2* is found to closely correlate with the iron content and R_2* mapping has been used for non-invasive diagnosis and monitoring of hepatic iron overload[124,125]. To account for the confounding effects in MRI signal models for multi-echo gradient-echo sequences, PDFF and R_2* are often jointly modeled and quantified through a multi-echo gradient-echo Dixon method[26,86].

Conventional joint PDFF and R_2* quantification techniques are mostly based on Cartesian trajectories[26]. Subjects are required to hold their breaths during the acquisition to avoid motion artifacts. However, it can be challenging for certain cohorts, such as pediatric and elderly patients, who may find it difficult to fully comply with the breath-holding requirements. In recent years, 3D free-breathing stack-of-radial Dixon MRI techniques[37,38,57] have been developed for PDFF and R_2* quantification. To compensate for respiratory motion and improve the quantification accuracy, motion gating is performed[33,83]. However, to ensure a sufficient number of radial spokes after motion gating, the scan time needs to be further prolonged[33]. To overcome this challenge, motion-resolved compressed sensing reconstruction methods[37,38,126], which apply sparsity constraints along the motion state dimension, have been investigated for accelerated self-gated free-breathing PDFF and R_2* quantification.

Recently, there are studies that investigate compressed sensing reconstruction models that explicitly incorporate non-rigid motion information during reconstruction. Studies have shown that such approaches can improve image sharpness in cardiac imaging[127] and pulmonary[128] and abdominal MRI[129], compared with previous motion-resolved reconstruction methods. Although there were some preliminary works on non-rigid motion compensated free-breathing liver MRI[129], this approach has not yet been investigated in free-breathing liver PDFF and R_2* quantification.

Another challenge in radial MRI is the sensitivity to system imperfections (as introduced and presented in Chapter 2). Different gradient delay correction techniques have been proposed to reduce gradient errors[57]. However, residual streaking artifacts can still be observed due to gradient non-linearity and off-resonance. In abdominal MRI with radial trajectories, it was observed that these streaking artifacts usually come from the arms (closer to the peripheral field of view). This problem could become worse when coupled with arm movements during the scan acquisition. A phase-preserving beamforming-based method (introduced in Chapter 2) is used to suppress these streaking artifacts while maintaining phase fidelity. An automatic interference patch selection pipeline is also incorporated to choose image patches in the two arms as interference regions.

In this work, we developed and evaluated a compressed sensing reconstruction method, which incorporated beamforming-based streaking reduction and non-rigid motion compensation, for accelerated free-breathing 3D stack-of-radial PDFF and R_2* quantification. We performed scans in six adults and six pediatrics subjects and compared the image sharpness by calculating relative maximum derivative along the superior-inferior direction around the diaphragm. We

further validated the PDFF and R_2* quantification accuracy by comparing with results from the reference breath-holding Cartesian MRI.

4.2 Methods

4.2.1 Overview of the Reconstruction Framework

An overview of the proposed reconstruction framework is illustrated in **Figure 4-1**. We first described the overall pipeline and details in each reconstruction module are provided in later subsections. Multi-echo data are acquired using a 3D stack-of-radial Dixon sequence during free-breathing acquisitions[57]. Gradient delays are corrected by aligning radial spokes using pre-scan calibration data[36,57]. A self-navigated respiratory motion signal is estimated using the central k_y=k_x=0 line[130]. The k-space data are then binned into different motion states using the self-navigation signal. A beamforming-based method is used to calculated coil sensitivity maps that specifically suppress radial streaking artifacts from the two arms[113]. Motion-resolved images are reconstructed using compressed sensing with a total variation constraint along the motion state[130] and a spatial Wavelet constraint on the images (introduced in section **4.2.2**). Images from the end-of-expiration motion state are selected as the reference motion state. Deformation vector fields (DVFs) between the reference motion state and other motion states are calculated by registering the magnitude images with the Demons algorithm[131]. A phase correction term is obtained by calculating the difference between warped phase images and the phase images from the target motion state. Warping the magnitude images and phase images using the DVFs and the phase correction term will be combined as an image warping operator. Later, we solve a compressed sensing model that incorporates this phase-corrected image warping operator for image

reconstruction. The multi-echo images were fitted[26] to a 7-peak fat model[70] with a single R_2* decay to generate the PDFF and R_2* maps.

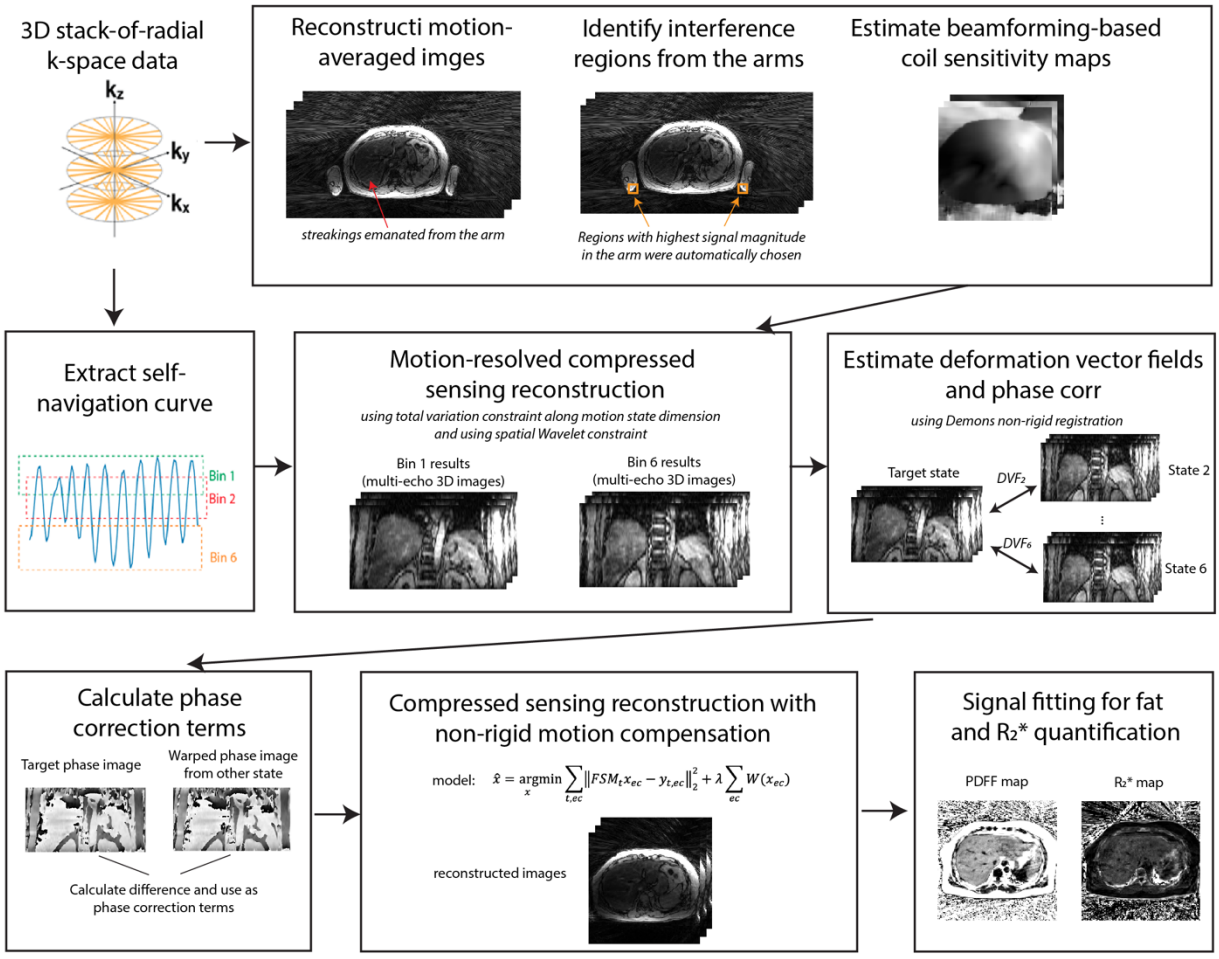

Figure 4-1. Overview of the reconstruction framework. Beamforming-based coil sensitivity maps are used during compressed sensing reconstruction for streaking artifact reduction. Deformation vector fields (DVF) between different motion states are estimated after motion-resolved reconstruction. The image warping operators contain a phase correction term to correct any phase difference resulting from B_0 variation between motion states.

4.2.2 Phase-Corrected Image Warping Operator

Construct image warping operators that faithfully transform the complex-valued images between motion states faces two main challenges. First, any residual radial streaking (e.g., from data undersampling) that leads to intensity changes can impact the accuracy of DVF estimation using an intensity-based image registration algorithm. As proposed in previous works[128], a motion-resolved reconstruction was first applied to suppress most of the undersampling artifacts before DVF estimation. In this work, we further used coil sensitivity maps calculated from the phase-preserving beamforming-based coil combination[113] method (which was introduced in Chapter 2) to suppress streaking artifacts from system imperfections. Second, B_0 variation can cause phase changes across motion states, especially near the liver-lung interface. Phase differences between motion states need to be carefully addressed when applying image warping operators on images from different motion states.

The optimization problem of the motion-resolved reconstruction used in this work is:

$$\hat{x} = \underset{x}{\operatorname{argmin}} \sum_{t,ec} \left\| FSx_{t,ec} - y_{t,ec} \right\|_2^2 + \lambda_1 \cdot TV_t(x) + \lambda_1 \cdot \sum_{ec,sl} W\left(x_{ec,sl}\right) \quad \text{(Eq. 4-1)}$$

while F represents non-uniform fast Fourier Transform (NUFFT), S represents coil sensitivity maps estimated using the beamforming-based method, $x_{t,echo}$ represents images at motion state t from the ecth echo, y_t represents the k-space data at motion state t from the ecth echo, TV_t represents total variation along the motion state, and λ represents the regularization parameter. In our implementation, the data are binned into 6 overlapping respiratory motion states, each containing 40% of the k-space data.

After the motion-resolved reconstruction, the end-expiration motion state is selected as the "reference state". The DVFs that transform images from other motion states to the reference state were calculated using the Demons image registration method[131]. In our implementation, the

Demons algorithm was used with 4 pyramid scales from coarse to fined resolutions, and each with 100 iterations.

Here, we propose a phase-corrected image warping operation that transforms images between motion states while considering the phase variations. The phase-corrected image warping operation consists of three steps: 1) magnitude image warping, 2) phase image warping, and 3) phase correction. In the first step, the magnitude image is transformed using the DVF and then a cubic interpolation is applied to generate the warped magnitude image. During phase image warping, the phase information was transformed using the DVF but with nearest-neighbor interpolation. That is, the phase of the warped image is assigned by the phase information in the nearest voxel before warping. Third, a phase correction term is added to the warped phase image to generate the corrected warped phase image. The phase correction term is estimated by comparing the warped phase image to the target phase image.

After the estimated DVFs and corresponding phase correction terms between motion states are obtained, the phase-corrected image warping operators can be used in the non-rigid motion compensated compressed sensing reconstruction.

4.2.3 Non-rigid Motion Compensated Compressed Sensing Reconstruction

We included the image warping operators introduced in the previous section and solved an optimization problem:

$$\hat{x} = \underset{x}{\operatorname{argmin}} \sum_{t,ec} \left\| FSM_t x_{ec} - y_{t,ec} \right\|_2^2 + \lambda \sum_{ec} W(x_{ec}) \quad \text{(Eq. 4-2)}$$

where F represents NUFFT, S represents coil sensitivity maps estimated using the beamforming-based method, M_t represents the phase-corrected image warping operator that transforms the reference motion state to motion state t, x is the multi-echo images from the target motion state,

W represents the 2D Wavelet transform (with Daubechies Wavelet) and λ represents the regularization parameter. The optimization problem was solved using the conjugate gradient descent method[132]. λ was empirically chosen to balance between the performance of artifact suppression and smoothing effects and the same λ was used for all our scans.

4.2.4 Experiments

In a Health Insurance Portability and Accountability Act (HIPAA)-compliant study approved by the local institutional review board, 6 adults (2 females and 4 males, age: 57±16 years) and 6 children (2 females and 4 males, age: 15±2 years) were scanned at a 3T scanner (MAGNETOM Skyra or Prisma, Siemens Healthineers, Erlangen, Germany). Written informed consent, parental permission, and assent, if applicable, were obtained for all subjects before research procedures. Each subject was scanned using a multi-echo gradient-echo golden-angle-ordered 3D stack-of-radial sequence[57] during free-breathing. Key sequence parameters included TE=(1.23, 2.46, 3.69, 4.92, 6.15, 7.38) ms, TR=8.85 ms, flip angle=5°. The detailed sequence parameters can be found in **Table 4-1**.

Table 4-1. Representative sequence parameters for free-breathing 3D stack-of-radial (FB Radial) and breath-holding (BH) 3D Cartesian axial MRI scans at 3T. N/A: not applicable.

Sequence parameters	**FB Radial**	**BH Cartesian**
TE (ms)	1.23, 2.46, 3.69, 4.92, 6.15, 7.38	
TR (ms)	8.85	
Flip angle (°)	5	5
Field of view	360-440 x 360-440 mm^2	360-440 x 360-440 mm^2
Slice thickness (mm)	5	5
Matrix size (x, y, z)	224-288, 224-288, 40	224-288, 224-288, 30
Acceleration or radial undersampling	Radial undersampling R=2 (based on Nyquist criteria)	Parallel imaging acceleration R=4
Radial spokes	178-226	N/A
Scan time (min:sec)	1:03 - 1:20	0:19

Free-breathing MRI data were reconstructed with three different reconstruction methods: 1) motion averaging + NUFFT, 2) self-gating + motion-resolved compressed sensing reconstruction with beamforming-based coil sensitivity maps, 3) self-gating + non-rigid motion compensated compressed sensing reconstruction with beamforming-based coil sensitivity maps. After image reconstruction, the multi-echo images were fitted to a signal model containing 7-peak fat spectrum[70] and a R_2* term using a multi-step adaptive fitting algorithm[26] to generate PDFF and R_2* maps.

4.2.5 Analysis and Evaluation

In the first part, we compared the results with or without the use of the beamforming-based streaking reduction coil sensitivity maps in motion-resolved reconstructed images. In the second part, we compared image sharpness between free-breathing radial MRI reconstructed with different motion compensation strategies. A metric, relative maximum derivative[128], was calculated using the maximum intensity change between the lung-liver interface along the superior-inferior dimension normalized by the mean signal intensity in the liver dome. Relative maximum derivative was calculated in images reconstructed by three different methods: motion-averaging without any motion gating, motion-resolved reconstruction, and non-rigid motion compensated reconstruction. For statistical analysis, Wilcoxon tests were performed to assess if there is any significant difference between different methods ($p<0.05$ considered significant).

For each subject, a trained researcher (with 5-year experience on analyzing abdominal MRI) placed three regions of interest (ROIs) on three axial slices while avoiding large vessels[36]. We measured the mean PDFF and mean R_2* in the ROIs. Bland-Altman analysis was performed to evaluate the agreement of PDFF and R_2* measurements between free-breathing techniques

and the breath-holding reference. Mean difference (MD) and 95% limits of agreements (LoA) for each comparison were calculated.

4.3 Results

Figure 4-2 shows the representative images reconstructed with and without beamforming-based streaking reduction. With conventional adaptive coil combination, most of the radial streaking artifacts due to undersampling can be largely suppressed after motion-resolved reconstruction. However, streaking artifacts from the arms can still exist. With sensitivity maps estimated using the beamforming-based method, specific streaking patterns emanating from the arms were suppressed.

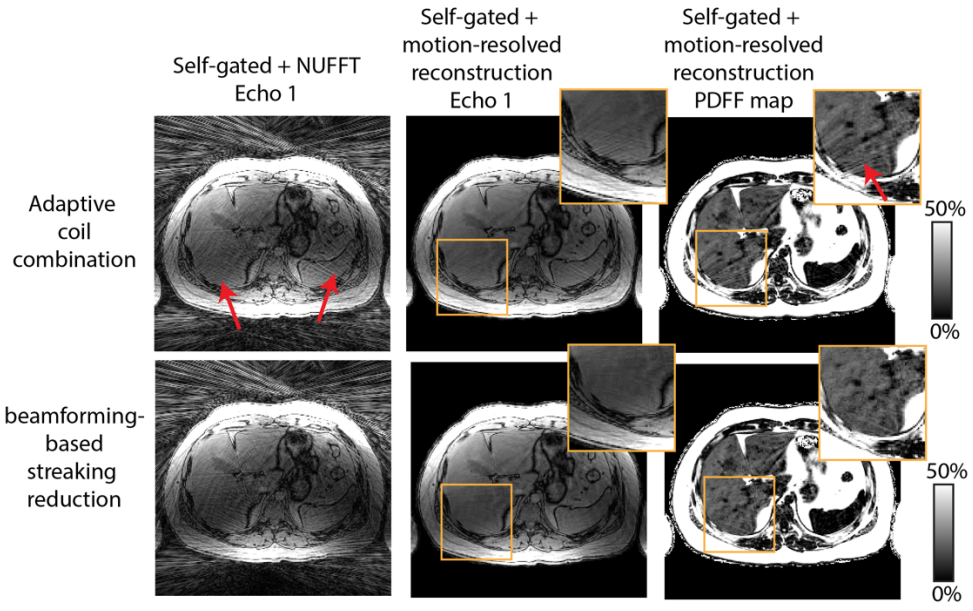

Figure 4-2. Representative example of motion-resolved reconstruction results using conventional adaptive coil combination or beamforming-based streaking reduction. With beamforming-based coil combination, the specific streaking patterns from the arms were suppressed in the (undersampled) self-gated images. After motion-resolved reconstruction, residual artifacts from the arms still exist in conventional methods and impact quantification maps.

Figures 4-3 and 4-4 show the representative reconstruction results of the proposed non-rigid motion compensation method versus breath-holding Cartesian MRI and self-gated + motion-resolved reconstruction. Both motion-resolved and non-rigid motion compensated reconstruction results suppressed most of the streaking artifacts in the echo images. Non-rigid motion compensated reconstruction provided sharper quantitative maps with reduced artifacts compared to results from motion-resolved reconstruction.

Bland-Altman analysis results are shown in **Figure 4-5**. The MDs of PDFF and R_2* between free-breathing motion-resolved reconstruction and the breath-holding reference were -0.15% and -0.35 s^{-1}, respectively. The MDs of PDFF and R_2* between free-breathing non-rigid motion compensated reconstruction and the breath-holding reference were 0.06% and 1.05 s^{-1}, respectively. The MDs are all small in either motion-resolved reconstruction or non-rigid motion compensated reconstruction results. The LoA of PDFF and R_2* measurements between free-breathing motion-resolved reconstruction and the breath-holding reference were [-3.14%, 3.05%] and [-13.2 s^{-1}, 14.4 s^{-1}]. The LoA of PDFF and R_2* measurements between free-breathing motion-resolved reconstruction and the breath-holding reference were [-2.40%, 2.28%] and [-11.4 s^{-1}, 13.5 s^{-1}]. The narrower LoA showed that non-rigid motion compensated can provide closer agreement with the breath-holding Cartesian-based reference technique.

The results of image sharpness measurements, in terms of the relative maximum derivative in the lung-liver interface, are shown in **Figure 4-6**. Motion-resolved reconstruction and non-rigid motion compensated reconstruction both had significantly higher relative maximum derivative (both $p<0.01$). Non-rigid motion compensated reconstruction has a higher relative maximum derivative than that in motion-resolved reconstruction results ($p=0.04$).

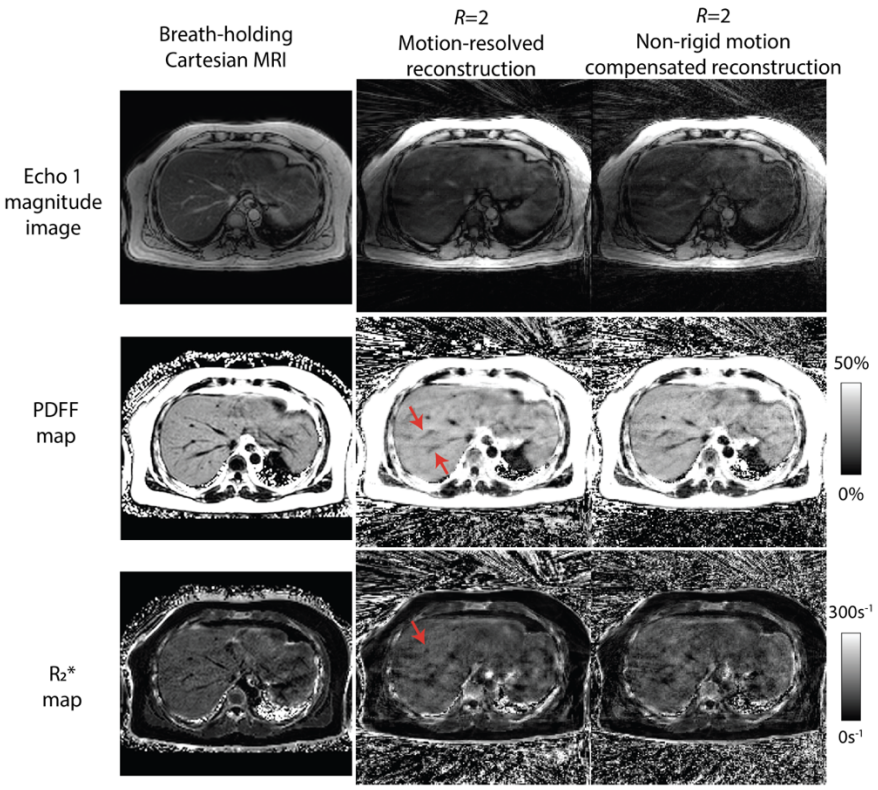

Figure 4-3. Representation reconstruction results comparing breath-holding Cartesian MRI and free-breathing MRI (R=2) with different reconstruction methods from a fatty liver subject (62 year-old male with BMI=31.4kg/m^2). Motion-resolved reconstruction can lead to slight blurring in the reconstructed PDFF and R_2* maps (red arrows).

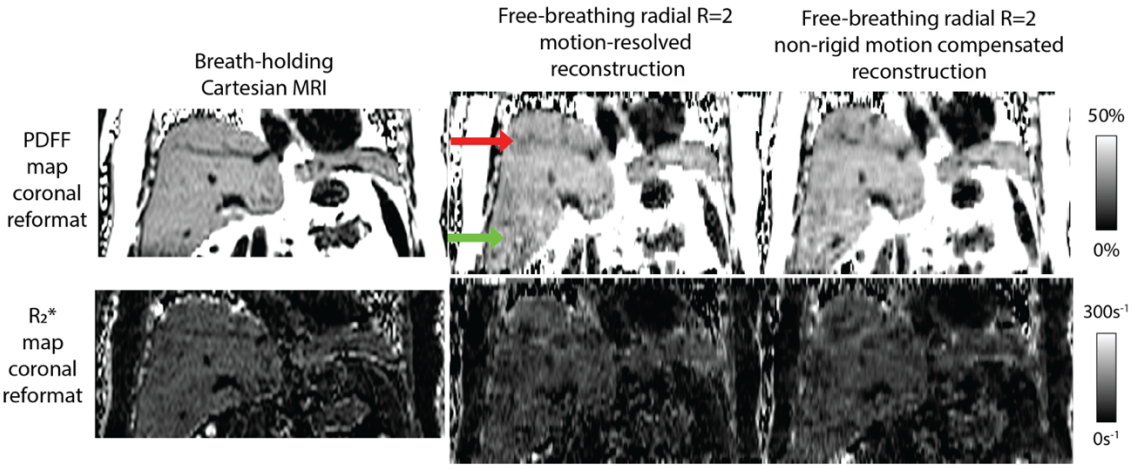

Figure 4-4. Reconstruction results comparing PDFF and R_2* maps in the coronal reformat (same subject as in **Figure 4-3**). Results from motion-resolved reconstruction show image blurring (red arrow) and residual artifacts that are not fully suppressed (green arrow).

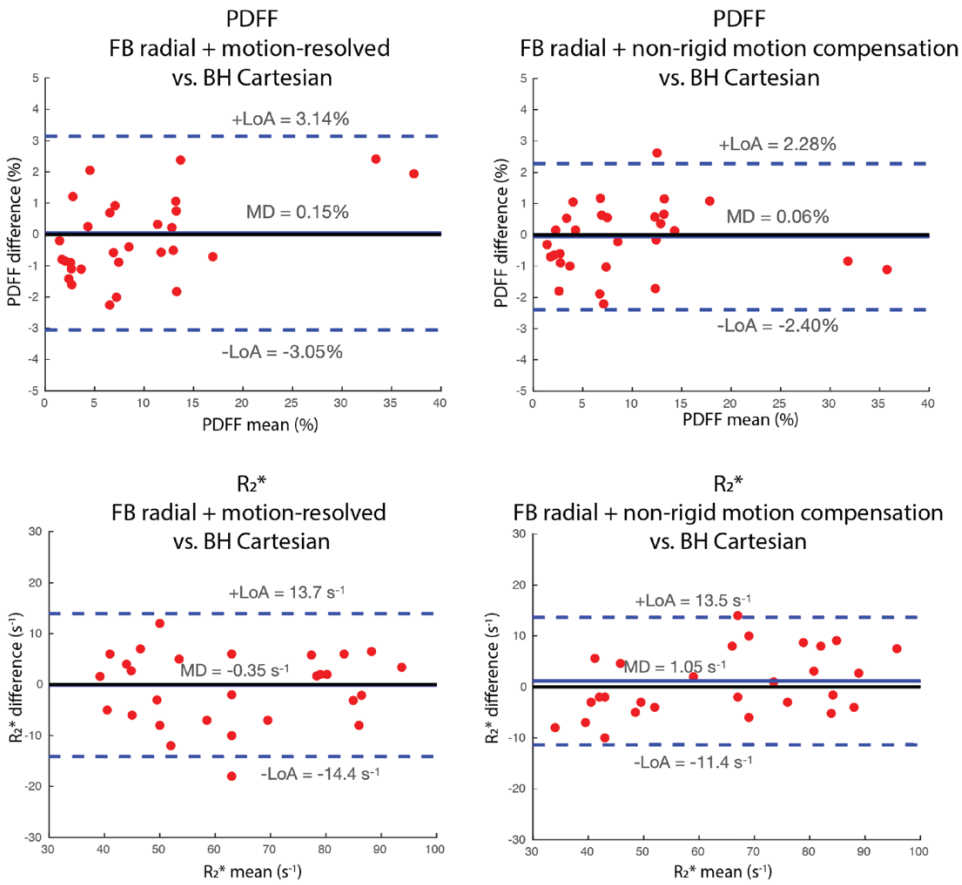

Figure 4-5. Bland-Altman plots comparing PDFF and R_2* from free-breathing MRI versus breath-holding Cartesian MRI. MD: mean difference. LoA: 95% limits of agreement.

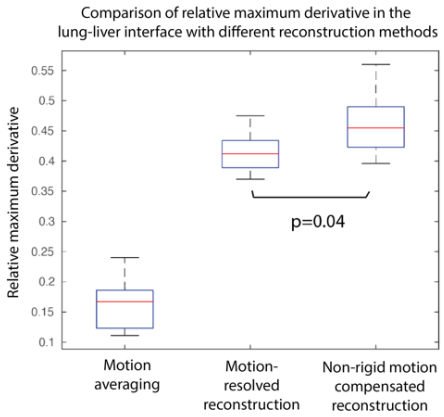

Figure 4-6. Box plot for comparison of relative maximum derivative in the lung-liver interface with different reconstruction methods.

4.4 Discussion

In this work, we presented a reconstruction framework for accelerated free-breathing self-gated PDFF and R_2* quantification. The proposed framework used beamforming-based coil combination (Chapter 2) to suppress streaking artifacts from system imperfections. Although compressed sensing can reduce the overall radial streaking artifacts from undersampling, the specific streaking artifact pattern from the arms were not fully suppressed if beamforming-based coil sensitivity maps were not used. Non-rigid motion information with a phase correction term were incorporated in the compressed sensing reconstruction model for non-rigid motion compensation in data acquired from free-breathing acquisitions.

We used the Demons non-rigid registration algorithm, which is an intensity-based method, to estimate the DVFs between different respiratory motion states. This algorithm has been commonly used in registering medical images in different applications. However, the Demons algorithm can face challenges in cases with more heterogeneous motion or in cases with lower image quality (e.g., still having residual radial streaking artifacts after motion-resolved reconstruction)[133]. Other optical flow estimation methods[134], based on L1, L2, L1-L2-combined regularizations or deep learning networks[135], developed in the image processing community also holds potential in modelling the non-rigid motion information between different motion states. As in previous works[128], we rely on a motion-resolved constrained reconstruction method to first suppress most radial streaking artifacts from data undersampling and motion-gating before performing DVF calculation. This process greatly increases the computational time for the entire pipeline for non-rigid motion compensated reconstruction. Recently, there are research works[136] that showed that deep learning networks can be trained to obtain accurate DVFs from images

reconstructed from highly undersampled k-space data and only using NUFFT. This holds potential to shorten the overall computational time of non-rigid motion compensated reconstruction.

We investigated the performance of non-rigid motion compensated reconstruction in data with radial undersampling factor of 2 (using Nyquist criteria to define "fully-sampled") and achieved scan times less than 1 minute and 30 seconds. This makes scans times of free-breathing PDFF and R_2* quantification comparable to the conventional breath-holding sequences, considering the time of giving breath-holding instructions and the wait time after breath-holding in conventional scans. The free-breathing scans without breath-holding requirements can also achieve larger volumetric coverage than the conventional breath-holding sequences. It is also possible to further reduce the free-breathing acquisition times by using a higher factor of radial undersampling factor or combining radial undersampling and k_z undersampling[137]. For the cases with more data undersampling, incorporating more sparsity constraints (in addition to the Wavelet constraints in this work) may help suppress the undersampling artifacts.

There are limitations in this study. First, there is a lack of fully-sampled motion-resolved images in free-breathing scans. To acquire such images, the acquisition time needs to be much longer, and the subject bulk motion needs to be minimal. In this work, we used quantification results from conventional breath-holding Cartesian-based PDFF and R_2* as a reference for comparison. Second, image quality evaluation by radiologists has not been investigated in this study. Further work on investigation of the diagnostic quality of the non-rigid motion compensated reconstruction results will be conducted in the future. Third, our dataset does not have subjects with high hepatic iron overload. The R_2* range investigated in this work is limited. Future work on hepatic iron overload patients is needed.

4.5 Conclusion

We presented a compressed sensing model with phase-preserving beamforming-based coil combination and non-rigid motion compensation for accelerated self-navigated free-breathing 3D stack-of-radial MRI PDFF and R_2* quantification. Non-rigid motion compensated reconstruction provides accurate PDFF and R_2* measurement compared with conventional breath-holding scans. In addition, non-rigid motion compensated reconstruction can improve sharpness, in terms of relative maximum derivative, compared with motion-resolved reconstruction.

This work is being prepared as a manuscript:

Shu-Fu Shih, Sevgi Gokce Kafali, Timoteo I. Delgado, Kara L. Calkins, Holden H. Wu. "Accelerated Free-Breathing Liver Fat and R_2* Quantification using Non-Rigid Motion Compensated Compressed Sensing Reconstruction". (*In preparation*)

CHAPTER 5

Improved Liver Fat and R_2* Quantification at 0.55T using Locally Low-Rank Principal Component Analysis-Based Denoising

5.1 Introduction

Proton density fat fraction (PDFF)[120] and R_2*[124] are powerful non-invasive MRI biomarkers for liver fat and iron accumulation, respectively. These two parameters can be quantified simultaneously using multi-echo gradient-echo Dixon MRI sequences followed by signal fitting to a model that resolves different confounding factors[23,26]. Several MRI sequences and signal fitting approaches have been developed and validated at 1.5T and 3T[23,26,36,138-141]. Recently, MRI field strengths <1.5T are being explored due to advantages such as reduced hardware and siting costs and reduction of artifacts in certain applications[41,43,46,142]. A lower-field MRI system with a larger bore diameter may also improve and comfort[143] for populations with obesity and at risk for fatty liver disease. In addition, decreased R_2* at lower fields can enable more accurate R_2* quantification in patients with high iron overload[51].

Most existing scan protocols for joint PDFF and R_2* quantification have been designed and validated at 1.5T and/or 3T. Adaptation to lower field strengths such as 0.55T requires careful investigation into the trade-offs associated with acquisition parameter choices. There are several important considerations. First, lower B_0 field strengths result in lower equilibrium polarization which reduces the signal-to-noise ratio (SNR)[41,43,46,142]. This is exacerbated when a small flip angle (FA) is used to reduce T_1-related bias in PDFF quantification[144]. Low SNR can degrade image quality and affect accuracy and precision of quantitative biomarkers[52,53,145]. Second, the smaller fat-water frequency difference at lower fields results in longer out-of-phase

(TE_{op}=6.47 ms) and in-phase (TE_{in}=12.94 ms) echo times. This increases scan time and limits sequence parameter choices. Increasing the number of scan repetitions to improve SNR, a common strategy, may be infeasible in breath-holding abdominal scans. Compromises in imaging parameters such as reducing image resolution and restricting volumetric coverage can reduce diagnostic quality.

Locally low-rank principal component analysis (PCA)-based denoising is one popular approach to suppress noise in multi-contrast MR images. By suppressing principal components associated with smaller coefficients, noise can be reduced while signal can be largely preserved. Difficulties in this type of method involve how to accurately estimate the signal rank and suppress the noise without removing the desired signal. Different approaches have been proposed to objectively estimate the noise level for effective noise suppression. One method, termed as the robust locally low-rank denoising (RLLR) technique[146], has been proposed. Using samples of random matrices from a known Gaussian distribution, the noise level in the multi-echo images can be estimated. Based on Stein's unbiased risk estimate (SURE)[147,148], the singular value threshold can be objectively obtained for noise suppression. RLLR has been shown to improve image quality for PDFF and R_2* quantification at 3T[149], but has not been studied at lower field strengths. On the other hand, random matrix theory (RMT)-based denoising[150-152] can accurately estimate noise level and remove the noise components by leveraging the spectral properties of random Gaussian matrices predicted by the Marchenko-Pastur Law[153]. This approach has shown promising noise suppression results, especially in diffusion MRI where many contrasts (i.e., multiple b-values and multiple directions) are available to construct locally low-rank patches[150-152,154-156]. There are initial studies applying

RMT-based denoising for lower-field MRI[156], but this has not yet been well studied for the application of PDFF and R_2* mapping.

In this study, our objective is to improve liver PDFF and R_2* quantification accuracy and precision at 0.55T by 1) systematically refining and validating the acquisition parameter choices and 2) investigating the performance of two locally low-rank PCA-based denoising methods, RLLR and RMT denoising. First, we performed a Monte Carlo simulation to investigate the impact of acquisition parameter choices on the accuracy and precision of PDFF and R_2* mapping at 0.55T. Using the proposed acquisition protocol informed by simulation results, we conducted experiments in a reference phantom, in the pelvis, and in the liver to compare the performance of PDFF and R_2* quantification using conventional reconstruction without denoising and with the use of RLLR and RMT denoising.

5.2 Methods

5.2.1 Acquisition Protocol for PDFF and R_2* Quantification at 0.55T

The choice of TEs and FA in the 3D multi-echo gradient-echo Dixon sequence affects PDFF and R_2* quantification accuracy[157-159]. A common choice at 3T is 6 echoes at either out-of-phase or in-phase echo times and a low FA of 3° to 5° for reducing the T_1-related bias in PDFF estimation[26]. Due to the longer out-of-phase and in-phase echo times at 0.55T, this strategy would lead to longer TEs and TR that prolong acquisition beyond the acceptable time for one breath-hold. On the other hand, the T_1-related bias is reduced at 0.55T because of the shortened T_1 values and the increased TR. A larger FA that balances between SNR and the T_1-related bias may be considered. As the R_2* values change with the field strength[51], TEs for accurate R_2* quantification should also be reconsidered. Therefore, we conducted a Monte Carlo simulation to

investigate different choices of FA, the first TE, and the echo spacing (ΔTE) with a range of reference PDFF and R_2* values at 0.55T. We limited our simulation to consider 6 echoes, a balance between sufficient number of echoes for quantification and reasonable scan time.

The signal $s(t_m)$ at the m-th TE was simulated using the signal model:

$$s(t_m) = M\left((1-F) + F \cdot \left(\sum_{j=1}^{7} a_j \cdot e^{i2\pi f_j t_m}\right)\right) \cdot e^{-R_2^* t_m} \cdot e^{-i2\pi\varphi t_m} + n \quad \text{(Eq. 5-1)}$$

where M represents the steady-state magnetization signal dependent on the TE, TR, T_1 and FA, F represents the PDFF value, a_j and f_j represent the relative amplitudes and frequencies for a 7-peak fat spectrum[70], φ represents the frequency shift due to B_0 field inhomogeneity, and n represents the complex-valued Gaussian noise.

We used T_1 of 339 and 187 ms for water and fat protons in the liver, respectively, based on previous work that measured *in vivo* relaxation times at 0.55T[42]. The simulated FA were in the range of 2° to 20°. The simulated first TEs and ΔTE were both in the range of 1.2 to 2.8 ms, considering hardware specifications of the 0.55T scanner and reasonable acquisition time of one breath-hold. The TR was set to include all the echoes and the spoiler gradient. When investigating PDFF accuracy and precision in the range of 0% to 40% (a range that covers most of the biopsy-proven metabolic dysfunction-associated steatotic liver disease [MASLD] patients with histologic steatosis grade 0 to 3[160]), the reference R_2* value was fixed at 30 s^{-1} (R_2* value at 0.55T with no iron overload[51]). When investigating R_2* accuracy and precision in the range of 20 s^{-1} to 90 s^{-1} (a range that covers mild, moderate and no iron overload at 0.55T[51]), the reference PDFF value was fixed at 5% (close to the common cutoff value for MASLD diagnosis[161]).

For each combination of parameters (FA, first TE, ΔTE, reference PDFF, and reference R_2*), 500 simulated instances were generated. For each instance, φ was randomly drawn from a range of (-100,100) Hz. The complex-valued noise was modelled as $n = n_r + i \cdot n_i$, where n_r

and n_i were independently drawn from a Gaussian distribution with the same variance σ^2. The value of σ^2 was set to be similar to the noise level in actual *in vivo* liver scans at 0.55T. To be more specific, the resulting apparent signal-to-noise ratio (aSNR), defined as signal mean divided by noise standard deviation, equaled 10 when PDFF=5%, R_2*=25 s^{-1}, and flip angle=8° in our Monte Carlo simulation.

All the simulated instances were fitted to 7-peak fat model[70] with a single R_2* decay term using a multi-step adaptive approach[26]. We measured the quantification accuracy by reporting the mean difference (MD) across instances of fitted PDFF and R_2* versus the reference values (i.e., the bias) at different parameter settings. We measured the quantification precision by reporting the standard deviation across instances of fitted PDFF and R_2* at different parameter settings.

5.2.2 Locally Low-Rank PCA-Based Denoising

Here we briefly summarize the two techniques that were investigated in this work, RLLR and RMT denoising (**Figure 5-1**), and describe how we adapt them to our specific application. More technical details can be found in previous works[146,150]. In the following paragraphs, we use p_x, p_y and p_z to represent the patch size in the three image dimensions, and use N_e and N_c to represent the number of echoes and number of coil channels, respectively.

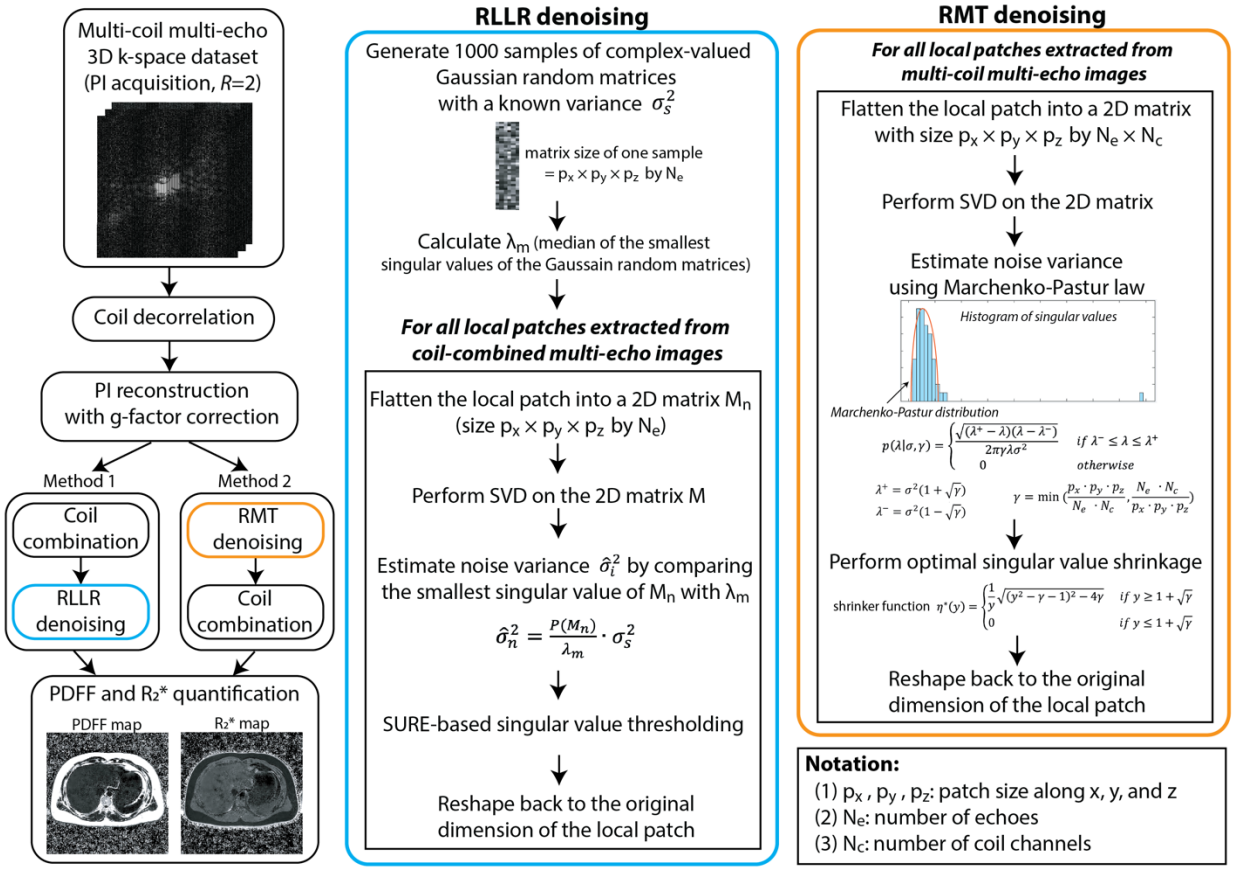

Figure 5-1. Reconstruction pipelines of the two locally low-rank PCA-based denoising methods used in this work. RLLR denoising was applied on coil-combined multi-contrast images while RMT denoising was applied on the multi-coil multi-contrast images. Both RLLR and RMT denoising methods needed to accurately estimate noise variance before performing singular value thresholding or shrinkage to suppress Gaussian noise. PI: parallel imaging. RLLR: robust locally low-rank. PDFF: proton density fat fraction. RMT: random matrix theory. SVD: singular value decomposition. SURE: Stein's unbiased risk estimate.

The RLLR denoising method constructs a 2D low-rank matrix M_n with dimensions [$p_x \cdot p_y \cdot p_z$ by N_e] from the coil-combined multi-echo images. Assuming the signal rank of M_n is smaller than N_e, the component associated with the smallest singular value is mainly noise. Before noise reduction, 2D random Gaussian matrix samples with dimensions [$p_x \cdot p_y \cdot p_z$ by N_e] were generated using a pre-determined variance σ_s^2. The median of the smallest singular values of these matrix samples, denoted as λ_m, is calculated. By comparing the smallest singular value of M_n to λ_m, the noise variance $\hat{\sigma}_n^2$ can be estimated using

$$\hat{\sigma}_n^2 = \frac{P(M_n)}{\lambda_m} \cdot \sigma_s^2 \quad \text{(Eq. 5-2)}$$

while $P(\cdot)$ extracts the smallest singular values of its argument. After estimating $\hat{\sigma}_n^2$, RLLR denoising finds the optimal value for singular value soft-thresholding by minimizing SURE[148] and obtaining the denoised matrix. All the overlapping local patches (with stride=1 along three spatial dimensions) are denoised using the same method and averaged to generate the final denoised images. Please note that previous works applied RLLR denoising on PDFF and R_2* mapping at 3T and only used a 2D low-rank matrix constructed from 2 image dimensions[146,149]. In this work, we extended the method to include the slice dimension.

The RMT denoising method relies on the Marchenko-Pastur law[153]. Let us consider a 2D random matrix X with dimensions [p by q] ($p \leq q$) whose entries are drawn from a Gaussian distribution of mean 0 and variance σ^2. The probability density function of the eigenvalues λ of the matrix $Y = \frac{1}{q}XX^T$, can be described by the Marchenko-Pastur distribution:

$$p(\lambda|\sigma^2,\gamma) = \begin{cases} \frac{\sqrt{(\lambda^+-\lambda)(\lambda-\lambda^-)}}{2\pi\gamma\lambda\sigma^2} & if\ \lambda^- \leq \lambda \leq \lambda^+ \\ 0 & otherwise \end{cases} \quad \text{(Eq. 5-3)}$$

where $\lambda^+ = \sigma^2(1+\sqrt{\gamma}), \lambda^- = \sigma^2(1-\sqrt{\gamma}), \gamma = p/q$. After constructing a low-rank matrix from local image patches, noise variance σ^2 can be estimated by comparing the distribution of the singular values of the low-rank matrix to the Marchenko-Pastur distribution. Because it requires a sufficient number of eigenvalues/singular values for accurate estimation of the noise variance, we use both echo and coil dimensions to construct low-rank matrices, which have dimensions of [$p_x \cdot p_y \cdot p_z$ by $N_e \cdot N_c$]. Once the noise variance is estimated, optimal singular value shrinkage based on Frobenius norm minimization[162] is used. All the overlapping local patches are denoised using the same method and averaged to generate the denoised multi-coil multi-echo images. Coil combination[65] is performed after RMT denoising.

Both denoising methods assume the noise is Gaussian distributed. Therefore, the reconstruction pipeline includes coil-decorrelation[163] and requires g-factor correction[164] for parallel imaging (PI)-accelerated data before denoising (**Figure 5-1**).

5.2.3 PDFF and R_2* Phantom Imaging

We validated the PDFF and R_2* quantification accuracy using a reference phantom (Calimetrix, Madison, Wisconsin) with seven PDFF-only (0% to 100%) and ten R_2*-only vials (17.7 to 1009.5 s^{-1} measured at 1.5T, provided by the vendor). Scans were performed using a whole-body 0.55T MRI system (prototype MAGNETOM Aera, Siemens Healthineers, Erlangen, Germany) equipped with high-performance shielded gradients (45 mT/m maximum amplitude, 200 T/m/s slew rate). Phased-array receiver coils (18-channel spine array and 6-channel body array) were used, and there were N_c=12 activated coil channels during the scans. To acquire phantom images with similar SNR as in the *in vivo* liver scans, we placed pads between phantom vials and the coils such that the space between the body array coil and the spine array coil was similar to the volume of an adult abdomen. We acquired data using a 3D multi-echo gradient-echo Dixon MRI research application sequence[26]. Key sequence parameters, based on findings from our Monte Carlo simulation, included N_e=6 with TEs = (2.16, 4.32, 6.48, 8.64, 10.8, 12.96) ms, TR = 14.7 ms, FA = 8°, field-of-view = 300x300 mm^2, matrix size = 192×192, and slice thickness = 5 mm. PI with acceleration factor (*R*) of 2 was used. The scan was repeated 50 times. Detailed sequence parameters are reported in **Table 5-1**. Each scan repetition was reconstructed individually, using three reconstruction methods: 1) conventional PI reconstruction (GeneRalized Autocalibrating Partially Parallel Acquisitions [GRAPPA]) without denoising, 2) PI reconstruction and RLLR denoising with an image patch size (p_x,p_y,p_z) = (5,5,5), and 3) PI

reconstruction and RMT denoising with an image patch size (5,5,5). The reconstructed images were fitted with a multi-step adaptive approach[26] accounting for fat model complexity[70] and single R_2* decay to generate PDFF and R_2* maps.

Table 5-1. Sequence parameters for phantom, *in vivo* pelvis, and *in vivo* liver MRI scans at 0.55 T. The out-of-phase and in-phase echo times in the Dixon sequences are underlined.

	Phantom		*In vivo* pelvis	*In vivo* liver
	2D multi-echo gradient echo	3D multi-echo Dixon	3D multi-echo Dixon	3D multi-echo Dixon
Acquisition orientation	Axial	Axial	Axial	Axial
Field of view (mm×mm)	300x300	300x300	400×400	380×380
TE (ms)	1.35, 3.5, 5.8, 8.0, 10.3, 12.6, 14.8, 17.1, 19.3, 21.6, 23.9, 26.1	2.16, 4.32, <u>6.48</u>, 8.64, 10.8, <u>12.96</u>	2.16, 4.32, <u>6.48</u>, 8.64, 10.8, <u>12.96</u>	2.16, 4.32, <u>6.48</u>, 8.64, 10.8, <u>12.96</u>
TR (ms)	35	14.7	14.7	14.7
Matrix size	160×160	192×192	192×192	192×192
In-plane resolution (mm×mm)	1.9×1.9	1.6×1.6	2.1×2.1	2.0×2.0
Number of slices	1	8	8	8
Slice oversampling	N/A	20%	20%	20%
Slice thickness (mm)	5	5	5	5
Flip angle (°)	15	8	8	8
Bandwidth (Hz/px)	1565	590	590	590
Parallel imaging	No	GRAPPA (R=2)	GRAPPA (R = 2)	GRAPPA (R = 2)
Averages	2	1	1	1
Scan time (min:sec)	0:12	0:19	0:19	0:19 (breath-hold)

The analysis consisted of two parts. First, we assessed the agreement of PDFF and R_2* values from different reconstruction methods versus the reference for the evaluation of accuracy. In this part, results from one scan repetition were used. We placed a region of interest (ROI) in each vial and calculated the mean PDFF and R_2*. PDFF values provided by the phantom vendor were used as the reference. To obtain the reference R_2* values at 0.55T, a single-slice 12-echo gradient-echo sequence was scanned and the images were fitted to a mono-exponential model[51]. Two R_2* vials had R_2*>250 s^{-1} (T_2*<4 ms) at 0.55T, which could not be reliably fitted using the specified protocol and were not included in the quantitative analysis. The MD and the concordance correlation coefficient (ρ_c)[165] between the measured PDFF and R_2* values versus the reference were calculated to assess agreement. Linear regression was also performed. Second, we evaluated the precision by calculating the standard deviation of quantitative measurements in each voxel across scan repetitions. The mean values of the change in PDFF and R_2* standard deviations between different reconstruction methods were reported.

5.2.4 *In Vivo* Pelvic Imaging

Quantitatively assessing denoising performance in liver scans can be challenging due to the difficulty to obtain reference high-SNR images from multiple scan repetitions. The liver position can vary across multiple breath-holds, leading to artifacts after averaging. Therefore, we performed an experiment in the pelvis to quantify accuracy and precision of *in vivo* PDFF and R_2* mapping. The experiment contained two analyses: 1) to investigate the denoising performance and the quantification accuracy under different noise levels and 2) to investigate the quantification precision by calculating the standard deviations of PDFF and R_2* measurements across scan repetitions. All *in vivo* experiments in this work were conducted under a Health

Insurance Portability and Accountability Act-compliant study protocol approved by the institutional review board. All subjects were scanned after providing written informed consent.

For the first analysis, we scanned a healthy volunteer (29-year-old male with body-mass index [BMI] 26.4 kg/m^2) using the 3D multi-echo gradient-echo Dixon MRI research application sequence[26] with 30 scan repetitions. Key parameters were the same as the phantom scans except for the field-of-view and the in-plane resolution. We averaged the multi-coil multi-echo k-space data across the 30 repetitions to generate the "reference" k-space data. We then added complex-valued random Gaussian noise with different variances to the reference k-space data to generate synthetic pelvis datasets with different noise levels. We chose the noise variances so that the synthetic images after GRAPPA reconstruction (without any denoising) had aSNR ranging from 3 to 15 (while the original reference image had aSNR=95). Here, aSNR was measured by the signal mean in a muscle ROI divided by background noise standard deviation in coil-combined echo 3 (out-of-phase) images. We performed RLLR and RMT denoising on the synthetic images after GRAPPA reconstruction. PDFF and R_2* maps were reconstructed using the same signal fitting method described earlier. We placed 3 ROIs, each with a size of 5 mm^2, in the subcutaneous fat tissue and in the muscle. Quantification accuracy was assessed by comparing mean PDFF and R_2* in these ROIs versus the quantification results in the reference data (from 30 repetitions).

For the second analysis, we scanned three healthy volunteers (3 males, age: 29.7$\pm$0.6 years, BMI: 24.5$\pm$2.6 kg/m^2) using the same sequence, each with 15 scan repetitions. Each repetition was reconstructed individually using three different methods: 1) conventional reconstruction without denoising, 2) RLLR denoising with a patch size (5,5,5) and 3) RMT denoising with a patch size (5,5,5). PDFF and R_2* maps were calculated using the same signal

fitting approach. To assess precision, we calculated pixel-wise standard deviations of PDFF and R_2* values across 15 scan repetitions. We further calculated the percentage of voxels which had reduced standard deviations of PDFF and R_2* (meaning improved precision) in denoised results compared to conventional reconstruction results.

5.2.5 *In Vivo* Liver Imaging

Eleven subjects (3 females and 8 males, age: 39.5±14.3 years, BMI: 26.3±4.0 kg/m^2) were recruited and scanned. Four of the subjects (1 female and 3 males, age: 49.5±16.8 years, BMI: 29.9±2.9 kg/m^2) had known fatty liver. All the subjects were scanned using the 3D multi-echo gradient-echo Dixon research application sequence[26] (**Table 5-1**) within a single breath-hold. Conventional reconstruction (no denoising, only GRAPPA) and reconstruction with the two denoising methods were performed. The same signal fitting approach was used to generate PDFF and R_2* maps.

For each subject, 3 circular ROIs, each with a size of 5 mm^2, were placed on 3 different axial slices in the liver while avoiding large vessels[36]. Mean and standard deviation of the PDFF and R_2* values within each ROI were recorded. Bland-Altman analysis was performed to analyze the agreement of the quantification results between the conventional reconstruction and two different denoising methods.

We performed Kruskal-Wallis tests to investigate if there were any differences in PDFF mean, R_2* mean, PDFF standard deviation and R_2* standard deviation in liver ROIs among the three reconstruction methods. $P<0.05$ was considered significant. If the Kruskal-Wallis tests indicated significant differences, additional pair-wise Wilcoxon signed rank tests with Bonferroni correction for the p-values ($p<0.05/3=0.017$ considered significance) were used to

evaluate if there was significant difference between a pair of two reconstruction methods. For all the statistical tests, only one liver ROI measurement in the mid-slice from each subject was used.

5.3 Results

5.3.1 Monte Carlo Simulation Results

The Monte Carlo simulation results are in **Figure 5-2**. A larger FA results in larger biases in PDFF due to T_1 differences between fat and water. In contrast, a smaller FA results in less precise PDFF and R_2* due to lower SNR. Shorter TEs and less T_2* weighting in the multi-echo signal also results in less precise PDFF and R_2*. Considering the quantification accuracy and precision across a range of relevant PDFF and R_2* values, we chose FA=8°, first TE=2.16 ms, and ΔTE=2.16 ms as the preferred setting. In this design, the third TE and the sixth TE corresponded to out-of-phase and in-phase echo times at 0.55T, respectively.

Based on the simulation results at a representative aSNR level, our selected acquisition protocol achieved PDFF biases of 0.2% to 2% and PDFF standard deviations of 5.4% to 7.2% for reference PDFF values ranging from 0% to 40%. At the same time, our selected acquisition protocol yielded R_2* biases of 0.2 s^{-1} to 2.2 s^{-1} and R_2* standard deviations of 10.5 s^{-1} to 17.7 s^{-1} for reference R_2*values ranging from 20 s^{-1} to 90 s^{-1}. Please note that these simulation results did not consider any denoising.

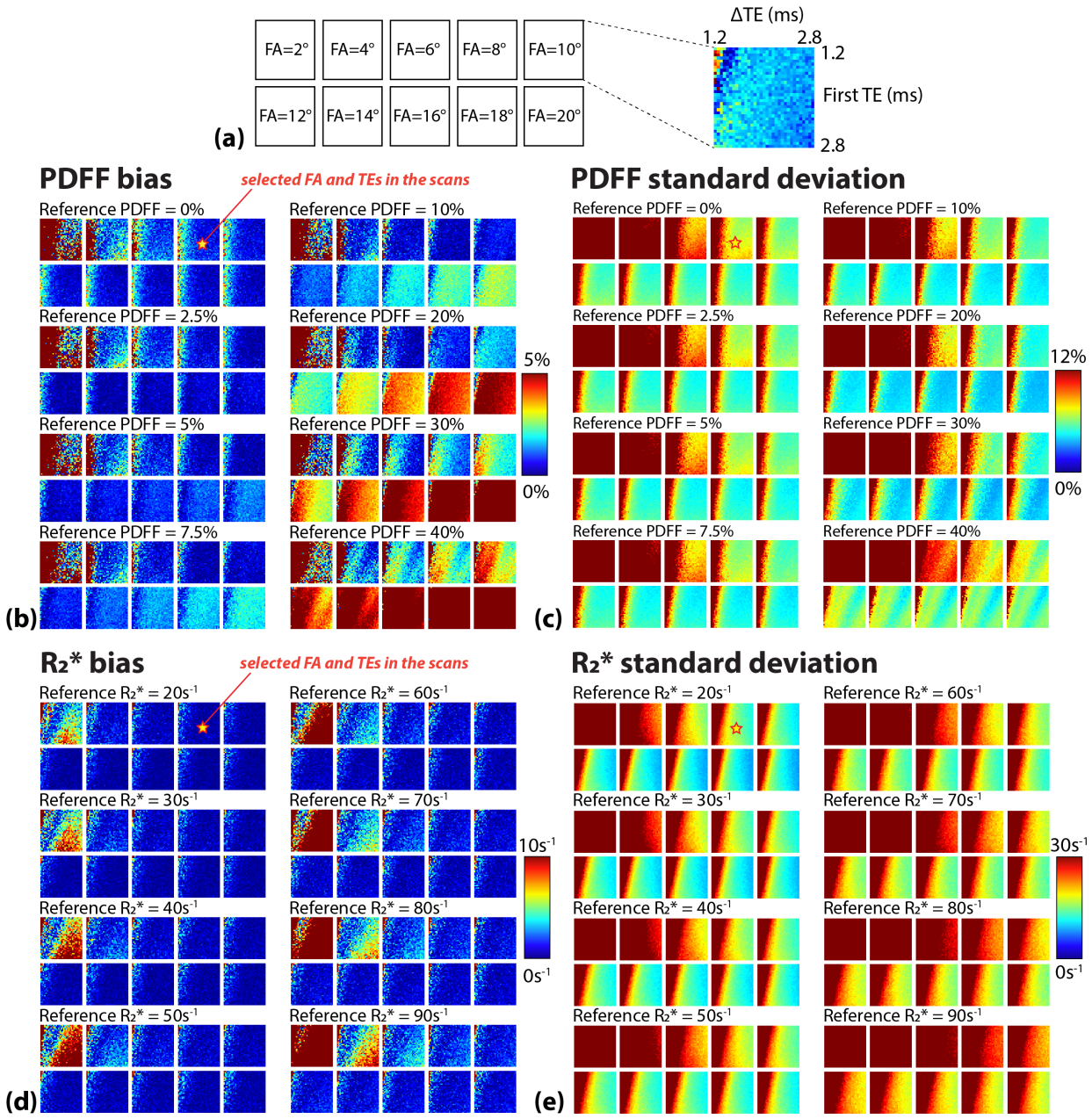

Figure 5-2. Monte Carlo simulation results regarding the accuracy and precision for PDFF and R_2* mapping using different flip angles (FA), first echo time (TE), and ΔTE at 0.55 T. To balance between accuracy and precision of parameter quantification and breath-holding scan time, we chose first FA=8°, TE=2.16 ms, and ΔTE=2.16 ms as indicated by the stars.

5.3.2 PDFF and R_2* Phantom Imaging Results

Figure 5-3(a,b) shows the phantom images from different reconstruction methods. The signal difference between denoised and non-denoised images showed minimal structured signals,

demonstrating effective noise suppression without removing desired signal. **Figure 5-3(c,d)** shows quantitative maps from one scan repetition. Without denoising, large PDFF errors and noisy PDFF and R_2* measurements were observed. Both denoising methods improved the visual quality of PDFF and R_2* maps with reduced inhomogeneity.

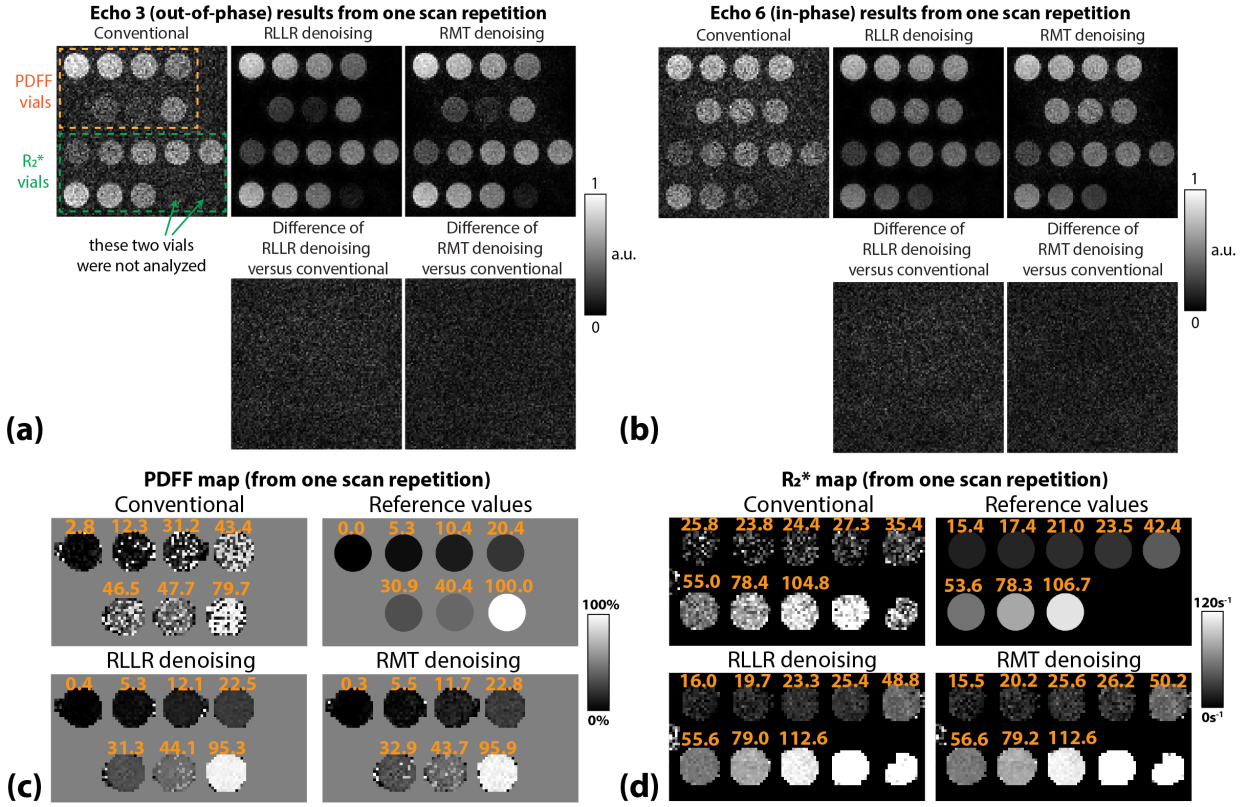

Figure 5-3. (a,b) Comparison of coil-combined echo 3 (out-of-phase) and coil-combined echo 6 (in-phase) images from different reconstruction methods All the images are displayed using the same window/level. (**c,d**) PDFF and R_2* quantification results in the reference phantom from one scan repetition. Numbers above each phantom vial show the measured mean value in that specific vial using a circular region of interest.

Compared with the reference, the MD (i.e., bias) of PDFF was 8.03% for conventional reconstruction, 0.51% for RLLR denoising, and 0.77% for RMT denoising. Compared with the reference, the MD (i.e., bias) of R_2* was 2.08 s^{-1} for conventional reconstruction, 2.76 s^{-1} for

RLLR denoising, and 3.48 s^{-1} for RMT denoising. **Figure 5-4(a,b)** shows the correlation plots of PDFF and R_2* measurements between different methods and the reference. Conventional reconstruction had ρ_c=0.845 in PDFF and ρ_c=0.984 in R_2* when compared with the reference. Compared with reference PDFF, RLLR denoising had ρ_c=0.997 with regression result y=0.956x+2.059 and RMT denoising had ρ_c=0.997 with regression result y=0.949x+2.022. Compared with reference R_2*, RLLR denoising had ρ_c=0.992 with regression result y=1.020x+2.550 and RMT denoising had ρ_c=0.994 with regression result y=1.028x+1.523. Both denoising methods achieved close PDFF and R_2* agreement with the reference. **Figure 5-4(c,d)** shows maps of pixel-wise standard deviations of PDFF and R_2* values from 50 scan repetitions. Compared with conventional reconstruction, RLLR denoising showed an average of 86% and 77% decrease in PDFF and R_2* standard deviations, respectively; RMT denoising showed an average of 77% and 67% decrease in PDFF and R_2* standard deviations, respectively.

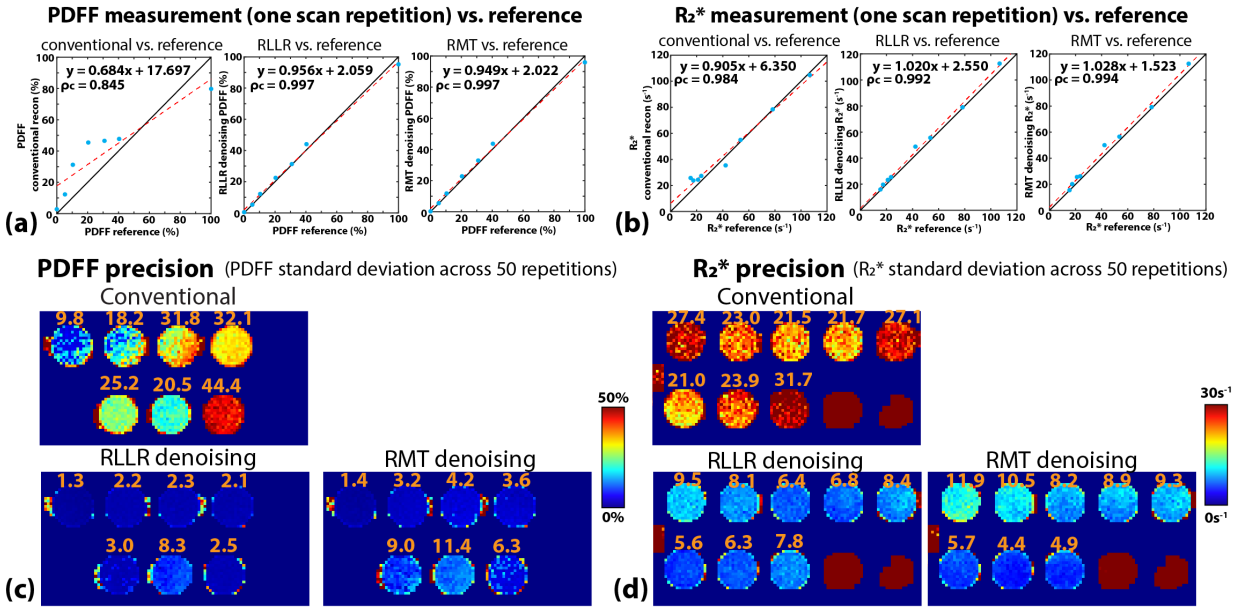

Figure 5-4. (a,b) Correlation plots that compare the mean PDFF and R_2* measurements from one scan repetition with respect to the reference values. **(c,d)** Maps showing the pixelwise standard deviation of PDFF and R_2* across 50 scan repetitions. Numbers above each phantom vial show the measured mean value in that specific vial using a circular region of interest. ρ_c: concordance correlation coefficient.

5.3.3 *In Vivo* Pelvic Imaging Results

Figure 5-5(a) shows the reference images (aSNR=95) and synthetic images with aSNR=8 reconstructed with different methods. Both denoising methods reduced PDFF quantification error and provided less noisy R_2* measurements. Without denoising, larger PDFF quantification errors were observed near the center of the body. This is consistent with the fact that the center of the body is farther away from the coil elements and the central region in the field-of-view has a higher g-factor and more noise amplification.

Figure 5-5(b) compares quantification results in three ROIs across different aSNR levels. Different ROIs exhibited different levels of sensitivity to aSNR. This can be due to differences in signal intensity magnitudes and the underlying PDFF and R_2* values in different types of tissue.

Both denoising methods reduced PDFF and R_2* errors. However, for images with aSNR less than 6, a PDFF bias of 1% to 2% still existed in two ROIs after denoising.

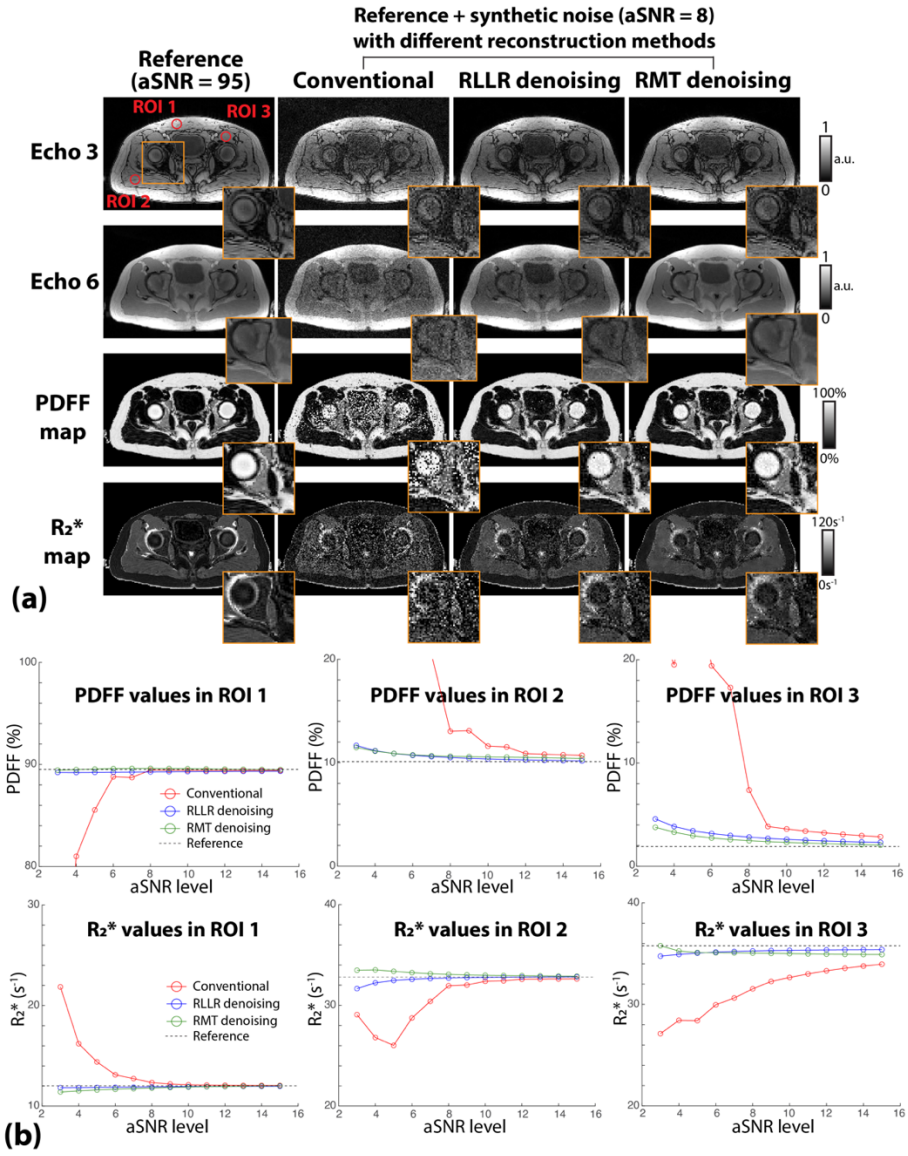

Figure 5-5. **(a)** Comparison of coil-combined images and quantitative maps in the synthetic pelvis dataset (apparent signal-to-noise ratio [aSNR]=8) reconstructed with different methods. **(b)** PDFF and R_2* measurements in three ROIs (locations depicted in **(a)**) across different aSNR levels. Both RLLR and RMT denoising achieved better quantification accuracy (closer agreement with reference results) for PDFF and R_2* than conventional reconstruction.

Figure 5-6 shows representative pelvis MRI reconstruction results and standard deviations of PDFF and R_2* measurements across 15 scan repetitions. Compared to conventional reconstruction, both denoising methods improved PDFF and R_2* precision in terms of smaller standard deviations. **Figure 5-6(b,d)** show the scatter plots of PDFF and R_2* standard deviations from one representative slice. Across all the subjects in RLLR-denoised results, the percentage of voxels with decreased PDFF and R_2* standard deviations were 97.5%±0.3% and 98.9%±0.4%. Across all the subjects in RMT-denoised results, the percentage of voxels with decreased PDFF and R_2* standard deviations were 96.9%±0.4% and 98.9%±0.5%.

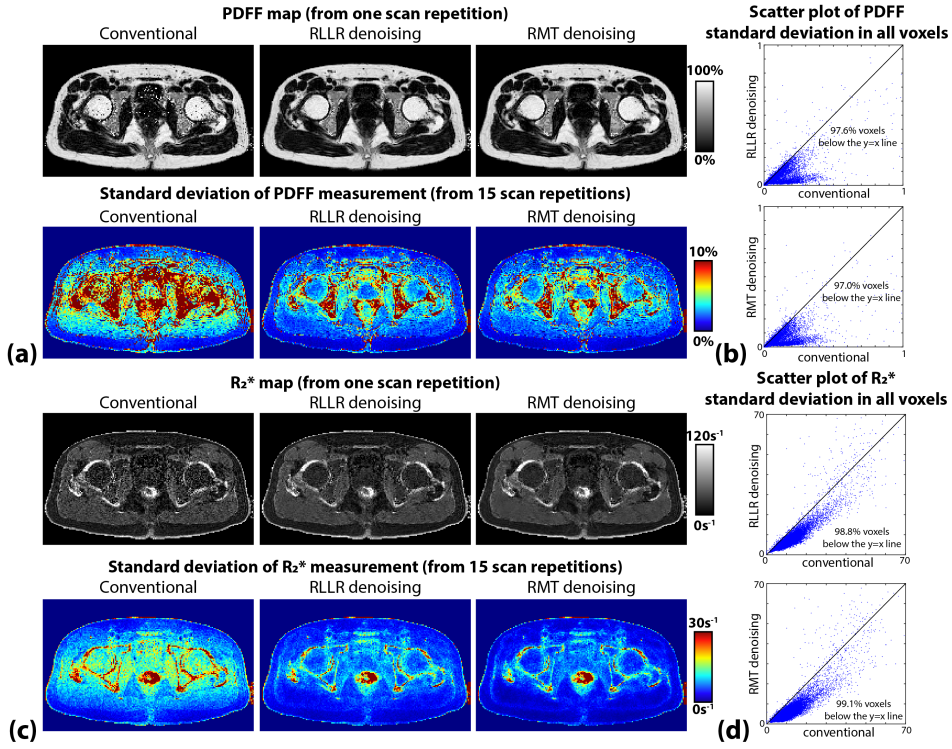

Figure 5-6. **(a)** Representative PDFF map and corresponding voxel-wise PDFF standard deviation map for different methods. **(b)** Scatter plot of PDFF standard deviation in all voxels (background voxels excluded). **(c)** Representative R_2* map and corresponding pixel-wise R_2* standard deviation map for different methods. **(d)** Scatter plot of R_2* standard deviation in all voxels (background voxels excluded).

5.3.4 *In Vivo* Liver Imaging Results

Figure 5-7 shows representative results from a fatty liver subject (45-year-old male, BMI=31.6kg/m^2). Noisy images from conventional reconstruction led to PDFF quantification error and noisy R_2* measurements. After RLLR or RMT denoising, vessels in the liver became more discernible and the PDFF and R_2* maps were less noisy.

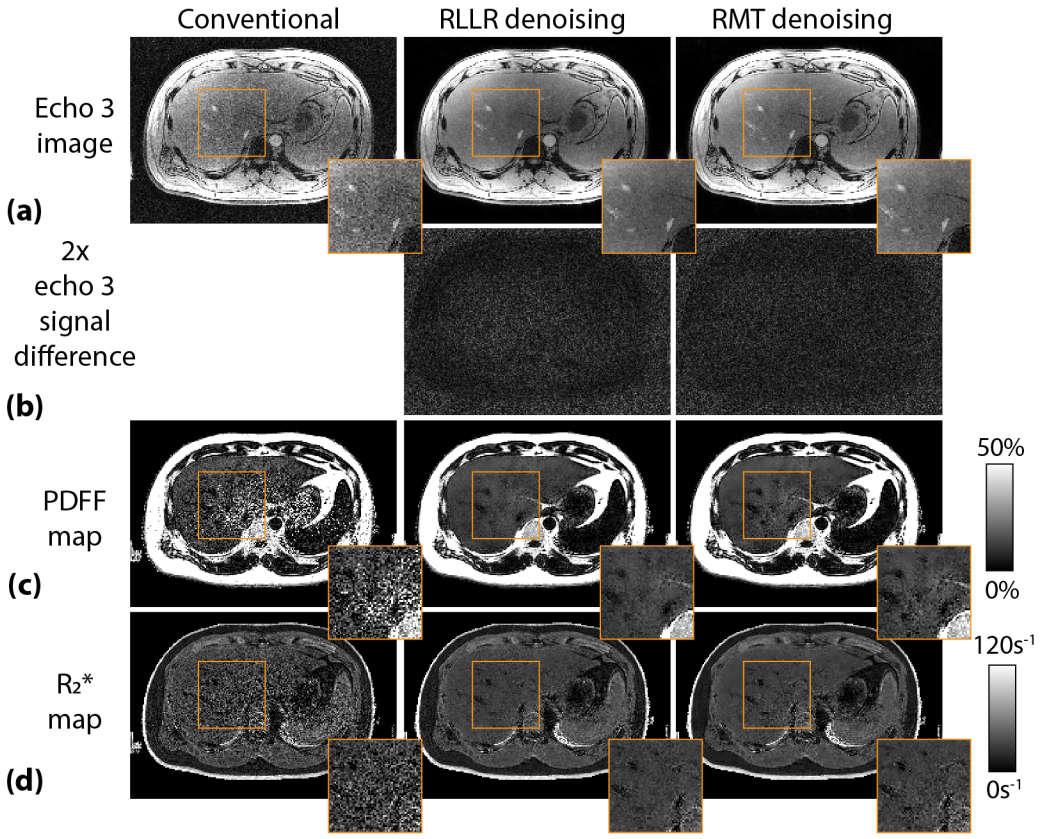

Figure 5-7. Representative result of **(a)** coil-combined echo 3 out-of-phase image, **(b)** signal difference in echo 3 image, **(c)** PDFF map, and **(d)** R_2* map from a fatty liver subject (45-year-old male, BMI=31.6 kg/m^2). The signal difference between conventional reconstructed and denoised images showed minimal tissue structures, demonstrating effective noise removal. Both RLLR and RMT denoising reduced PDFF quantification errors and provided less noisy R_2* maps.

Figure 5-8 shows Bland-Altman plots comparing liver PDFF and R_2* values from two denoising methods versus using conventional reconstruction. For PDFF, RLLR and RMT denoising showed a MD of -0.96% and -0.82%, respectively, when compared with conventional

reconstruction. This is consistent with previous findings[166] that noise would lead to a positive PDFF bias (i.e., reducing noise can reduce the bias). On the other hand, the MD in R_2* between denoised and non-denoised results were small, with values of 0.50 s^{-1} between RLLR denoising and conventional reconstruction and 0.55 s^{-1} between RMT denoising and conventional reconstruction.

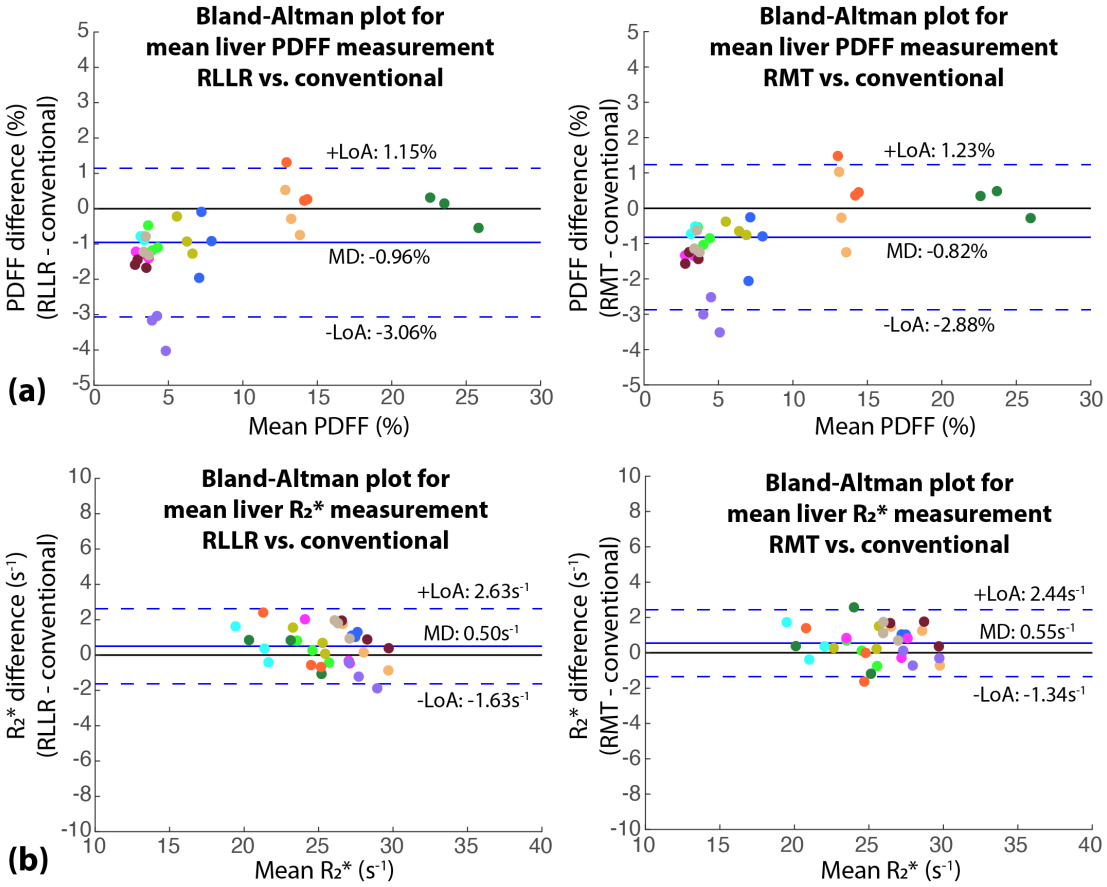

Figure 5-8. (a) Bland-Altman plots comparing mean liver PDFF measurements in results using RLLR and RMT denoising versus conventional reconstruction. **(b)** Bland-Altman plots comparing mean liver R_2* measurements in results using RLLR and RMT denoising versus conventional reconstruction. MD: mean difference. LoA: 95% limits of agreement.

Figure 5-9 shows scatter plots of PDFF and R_2* standard deviations in liver ROIs from two denoising methods versus conventional reconstruction. The mean value of PDFF standard deviations in liver ROIs were 8.80% for conventional reconstruction, and was reduced to 1.79%

and 2.00% after RLLR and RMT denoising, respectively. The mean value of R_2* standard deviations in liver ROIs was 14.17 s^{-1} for conventional reconstruction, and was reduced to 5.31 s^{-1} and 4.81 s^{-1} after RLLR and RMT denoising, respectively.

The Kruskal-Wallis ($p<0.05$ considered significant) tests did not indicate significant differences in mean PDFF ($p=0.209$) and mean R_2* ($p=0.846$) among three reconstruction methods. On the other hand, the Kruskal-Wallis tests found significant differences in PDFF standard deviations ($p<0.001$) and R_2* standard deviations ($p<0.001$) among three reconstruction methods. In pair-wise Wilcoxon tests, both RLLR denoising and RMT denoising had significant differences in PDFF standard deviations and R_2* standard deviations when compared with conventional reconstruction ($p<0.001$ for all comparisons). There was no significant difference in PDFF standard deviations ($p=0.083$) and R_2* standard deviations ($p=0.577$) between RLLR denoising and RMT denoising.

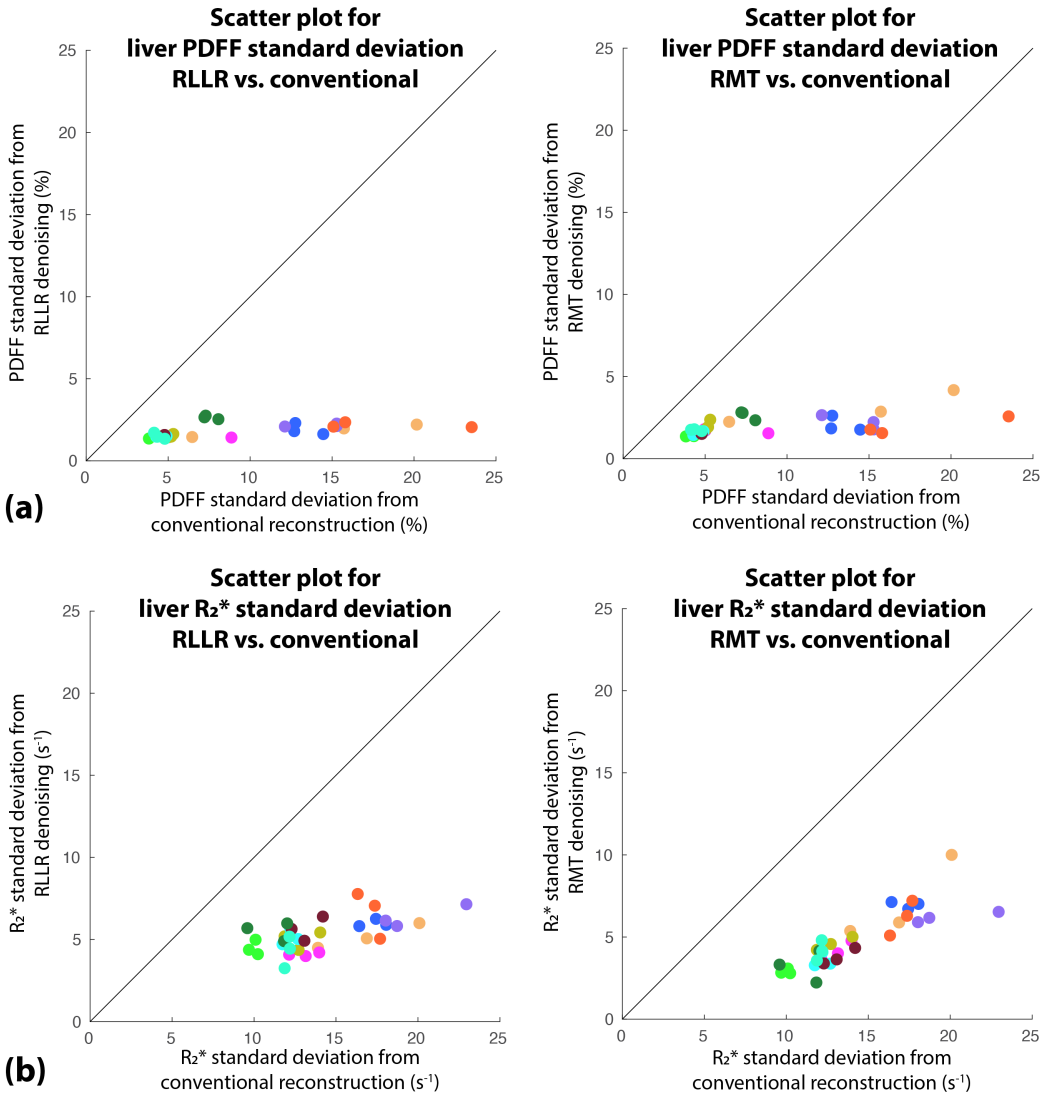

Figure 5-9. (a) Scatter plots comparing liver PDFF standard deviation in results using RLLR and RMT denoising versus conventional reconstruction. **(b)** Scatter plots comparing liver R_2* standard deviation in results using RLLR and RMT denoising versus conventional reconstruction. Both denoising methods greatly reduced standard deviations of PDFF and R_2* measurements in liver ROIs.

5.4 Discussion

In this work, we refined and validated the acquisition parameter choices for PDFF and R_2* quantification at 0.55T and investigated the performance of two denoising methods to improve the quantification accuracy and precision. Based on the Monte Carlo simulation, we designed a 6-echo protocol for quantifying liver PDFF and R_2* at 0.55T. Even with our careful

design of acquisition parameters at 0.55T, the resulting biases and appreciable standard deviations of PDFF and R_2* underscored the importance and need of denoising algorithms. Using the proposed protocol in phantom and pelvis scans, we demonstrated that both RLLR and RMT denoising improved quantification accuracy in terms of close agreements with the reference, and improved quantification precision in terms of reduced standard deviations across scan repetitions. In a cohort of eleven subjects, RLLR and RMT denoising significantly reduced standard deviations of PDFF and R_2* measurements in the liver ROIs when compared to conventional reconstruction.

To determine an acquisition protocol that can estimate PDFF and R_2* values in a range that is relevant for patient cohorts, we focused on PDFF values from 0% to 40% and R_2* values from 20 s^{-1} to 90 s^{-1}. Although this range covers PDFF in fatty liver patients and mild iron overload (45 $s^{-1} < R_2^* < 91$ s^{-1} from previous work[51]), higher R_2* in patients with severe iron might not be robustly estimated using the proposed protocol. While longer TEs with more fat-water phase difference is beneficial for fat-water separation, quantifying higher R_2* requires more echoes placed at shorter TEs. For these cases, the Monte Carlo simulation approach used in this work can be extended to include more relevant parameters and help design dedicated acquisition protocols.

In a previous multi-center multi-vendor PDFF phantom study[167], the slope of the regression line is in the range of 0.86 to 1.02 at 1.5T and 0.91 to 1.01 at 3T using vendor protocols. The intercept of the regression line was in the range of -0.65% to 0.18% at 1.5T and -0.78% to -0.21% at 3T. In our phantom experiment at 0.55T, the slopes of the regression line were 0.956 and 0.949 after RLLR and RMT denoising, demonstrating similar PDFF linearity to that at 1.5T and 3T. The intercepts of the regression line were 2.06 and 2.02 after denoising.

Even though RLLR and RMT denoising can effectively reduce the noise, a higher positive bias in PDFF is still observed at 0.55T compared with results from 1.5T and 3T.

The denoising performance of RLLR and RMT is dependent on the original image SNR, which is affected by different factors including tissue types, acquisition parameters, proximity to the coils, and g-factor distribution if PI is used. From our pelvis experiment, we found the quantification accuracy, especially for PDFF, is limited in extremely low aSNR cases. Therefore, future improvements such as better surface coils with more elements or sampling patterns with reduced g-factor penalty are also important to further improve PDFF and R_2* quantification at 0.55T. We also found PDFF and R_2* had different sensitivities to noise. Without denoising, PDFF in liver ROIs showed larger bias. On the other hand, the mean R_2* values in liver ROIs were rather consistent with or without denoising. Nevertheless, both denoising methods can provide less noisy R_2* maps for more precise measurements and better diagnostic quality.

The computational bottlenecks for both denoising methods were the calculations of singular value decomposition. In our 3D liver dataset, the average computational time for the denoising step (excluding PI reconstruction and signal fitting) was 4 minutes 20 seconds for RLLR denoising and 4 minutes 50 seconds for RMT denoising, using a MATLAB script (R2023a, MathWorks, Natick, Massachusetts) running on a 64-Core 2.7 GHz CPU (AMD Ryzen Threadripper PRO 5995WX). RMT denoising had longer computational time because the singular value decomposition was applied on larger 2D matrices. For both methods, computational time can be further reduced by optimizing the software implementation and running on high-performance hardware.

Both RLLR and RMT denoising rely on two assumptions: 1) the underlying noise is Gaussian distributed and 2) the low-rank property exists in local image patches. The

requirements are typically met in multi-contrast MR images after noise statistics are carefully corrected. Therefore, both denoising methods can be potentially applied in many other lower-field multi-contrast or quantitative MRI applications in which low SNR is a common problem. Even though the noise variance can be objectively estimated using these two methods, the choice of patch size is dependent on the effective signal rank and is usually based on empirical results, as used in this work and in previous locally low-rank denoising works[146,150-152]. One might need to adjust the patch size for optimal denoising performance for different datasets.

Deep learning-based methods are another promising approach for noise suppression[168]. Many deep learning-based denoising methods for lower-field MRI rely on supervised learning that requires a database of training data[169,170]. However, obtaining high-SNR reference training data from multiple scan repetitions may be difficult for abdominal scans due to breath-holding requirements. For these cases, the denoising methods investigated in this work can be used to generate training data.

This study has limitations. First, our studied cohort had a limited size and none of the subjects had liver iron overload (T_2* > 45 ms at 0.55T[51]). Scans in subjects with high liver iron content should be conducted in future works and the denoising performance should be further validated. Second, our phantom analysis only included fat-only and R_2*-only vials which may not reflect the actual *in vivo* environments in the liver, where both fat and iron may be present, although this condition is rare. Further experiments should be done in phantoms with different combinations of PDFF, R_2* and T_1 values[171] to investigate the denoising performance and the limitations.

5.5 Conclusion

We used a Monte Carlo simulation to design an acquisition protocol for PDFF and R_2* quantification at 0.55T with validation in phantom experiments. We showed that both RLLR and RMT denoising improved quantification accuracy in terms of closer agreement with the reference, and improved quantification precision in terms of reduced standard deviations across scan repetitions. In a cohort with healthy volunteers and fatty liver subjects, RLLR and RMT denoising both improved quantitative maps in terms of the significant decrease of PDFF and R_2* standard deviations in liver ROIs when compared with conventional reconstruction.

This work is under review:

Shu-Fu Shih, Bilal Tasdelen, Ecrin Yagiz, Zhaohuan Zhang, Xiaodong Zhong, Sophia X. Cui, Krishna S. Nayak, Holden H. Wu. "Improved Fat and R_2* Quantification at 0.55T using Locally Low-Rank Denoising". (*Under review*)

CHAPTER 6

K-space Low-Rankness Enabled Additive NoisE Removal (KLEANER) for Liver Fat and R_2* Quantification at 0.55T

6.1 Introduction

Clinical diagnosis using magnetic resonance imaging (MRI) can be significantly impacted by low signal-to-noise ratio (SNR) in the images, which may arise due to specific characteristics of certain sequences (e.g., diffusion-weighted imaging [46]) or limitations imposed by physics (e.g., lower field strengths[41,43]). Scans with multiple averages can increase SNR but lengthen the acquisition time. Image filtering[55] or constrained reconstruction[56] can suppress high-frequency components, but they can incur risks of over-smoothing the images. Deep learning methods have also been proposed to improve SNR[172]. However, deep learning methods may not generalize well to data outside of the training data distribution and the nonlinear processing in neural networks is still difficult to interpret or explain.

In recent years, image-domain random matrix theory (RMT)-based denoising[150-152,154] has demonstrated superior performance compared to conventional techniques, and has a strong theoretical foundation in RMT. The success of image-based RMT denoising relies on 1) assumption and preservation of Gaussian noise characteristics in the MR images, 2) redundancy in the image patches, often across multiple dimensions (e.g., 2D/3D image space, coil channels, and contrast weighting), to separate signal and noise in the spectral domain (i.e., singular value distributions), and 3) an objective method to estimate noise variance based on the Marchenko-Pastur law[153]. Once the noise variance is estimated, singular value thresholding[173] or shrinkage[162] can then be used to suppress the Gaussian noise-related components.

There are some considerations when applying image-based RMT denoising methods. First, because some image reconstruction steps distort noise characteristics, corrections (e.g., g-factor correction after parallel imaging (PI) reconstruction) may be required before denoising. Second, the redundancy level in images can be spatially varying and dependent on the number of coils or contrasts, the underlying tissue signal rank, and the patch size. On the other hand, k-space linear dependencies, which is a general characteristic in multi-coil MRI k-space, have long been known since the introduction of GeneRalized Autocalibrating Partially Parallel Acquisitions (GRAPPA)[174]. Techniques involving constructing a low-rank block-Hankel matrix using k-space patches have also been proposed[175-177], but mainly for undersampled MRI reconstruction.

Inspired by these works, we developed a novel k-space denoising technique, "K-space Low-rankness Enabled Additive NoisE Removal (KLEANER)," which can suppress additive Gaussian noise in multi-coil multi-contrast k-space data. We investigated the spectral property of block-Hankel matrices constructed from Gaussian noise and empirically showed its connection with the Marchenko-Pastur law. We showed that the proposed KLEANER technique can be directly applied in originally-acquired PI-undersampled k-space datasets without the requirement of g-factor correction.

We demonstrated the proposed KLEANER technique for denoising in a phantom experiment at 0.55T and in *in vivo* liver fat and R_2* quantification using gradient-echo (GRE) Dixon MRI at 0.55T. We compared KLEANER denoising with image-based RMT denoising methods that have been proposed to reduce noise and improve quantitative maps[155,178].

6.2 Methods

6.2.1 Spectral Property of Block-Hankel Matrices

Limited support in images will lead to linear dependencies among signals in k-space patches[176,179]. Therefore, a low-rank block-Hankel matrix can be constructed by stacking vectorized data extracted from all local k-space patches, which contain signal and noise components. Since this block-Hankel matrix has repeated entries along the anti-diagonal line, its noise characteristics may differ from a random matrix. Therefore, we performed a Monte Carlo simulation to investigate the spectral property of noise in such block-Hankel matrices.

The workflow of our Monte Carlo simulation is shown in **Figure 6-1(a)**. We first generated a 3D tensor with independent and identically distributed random Gaussian noise to simulate 2D multi-coil noise-only data. Data dimensions were set to be similar to the actual MRI acquisitions of interest (e.g., [k_x, k_y, coils*contrasts] = [192, 192, 50]). A 2D block-Hankel matrix was constructed using a patch size of [5, 5]. For comparison, we generated another 2D random Gaussian matrix with the same dimensions as the block-Hankel matrix. We computed and compared their singular value distributions. This process was performed with different data dimensions, and each setting was repeated 1000 times.

Monte Carlo simulation results using different data dimensions are shown in **Figure 6-1 (b)**. The block-Hankel matrix had similar noise spectral properties as the corresponding random matrix, where both distributions closely followed the Marchenko-Pastur law predictions. We performed one-sample Kolmogorov-Smirnov statistical tests with the null hypothesis (H_0) being that the singular value distribution of a block-Hankel matrix generated from our Monte Carlo simulation is consistent with the Marchenko-Pastur law prediction. Across all the settings we use in our experiment, including matrix sizes 128x128 to 256x256 and coils*contrasts = 10 to 100,

the statistical tests failed to reject H_0 ($p>0.05$). These results empirically showed that the Marchenko-Pastur distribution can describe the spectral property of a block-Hankel matrix constructed from a matrix containing random Gaussian noise.

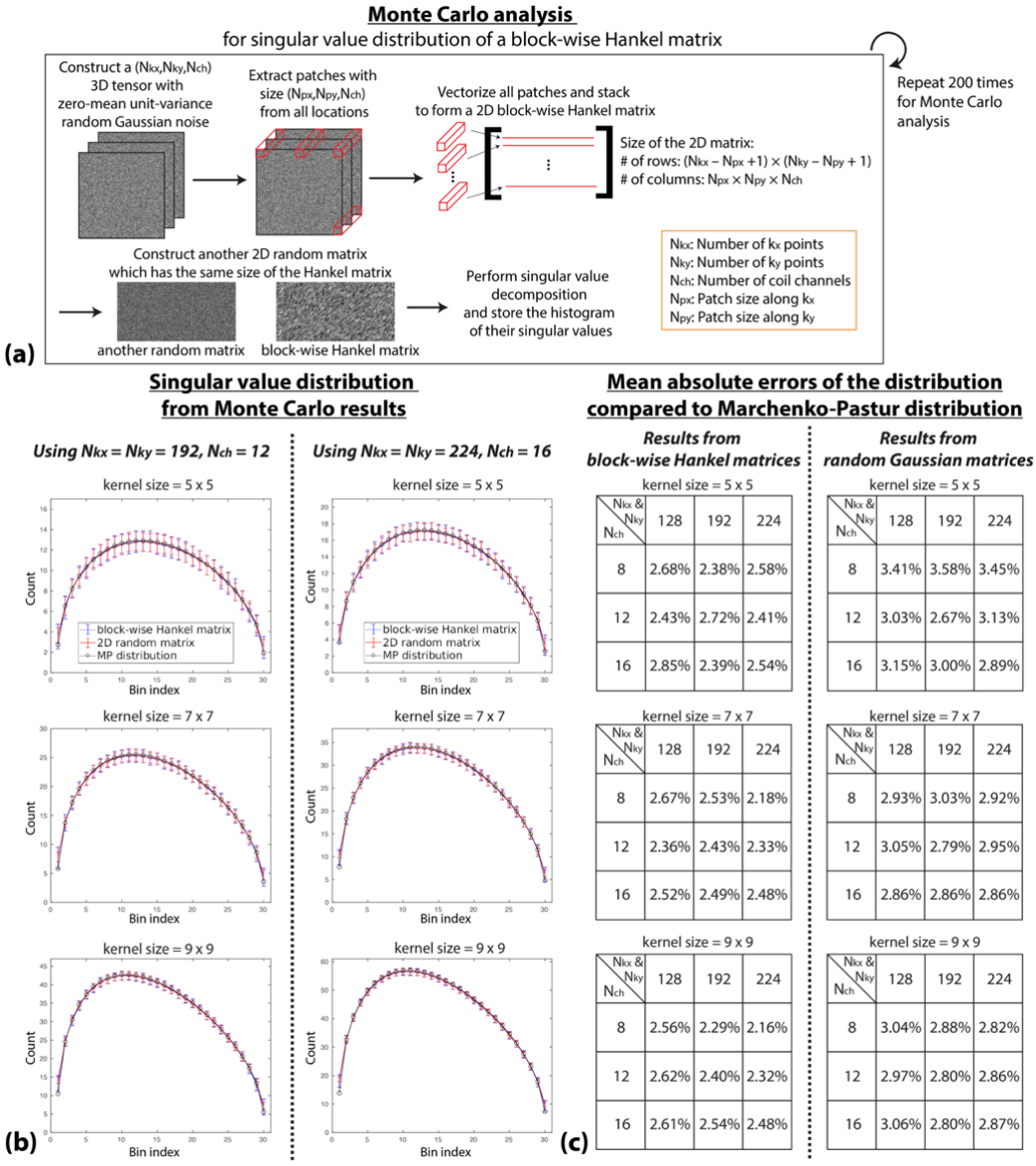

kernel size = 5 x 5

Nch \ Nkx & Nky	128	192	224
8	2.68%	2.38%	2.58%
12	2.43%	2.72%	2.41%
16	2.85%	2.39%	2.54%

kernel size = 5 x 5

Nch \ Nkx & Nky	128	192	224
8	3.41%	3.58%	3.45%
12	3.03%	2.67%	3.13%
16	3.15%	3.00%	2.89%

kernel size = 7 x 7

Nch \ Nkx & Nky	128	192	224
8	2.67%	2.53%	2.18%
12	2.36%	2.43%	2.33%
16	2.52%	2.49%	2.48%

kernel size = 7 x 7

Nch \ Nkx & Nky	128	192	224
8	2.93%	3.03%	2.92%
12	3.05%	2.79%	2.95%
16	2.86%	2.86%	2.86%

kernel size = 9 x 9

Nch \ Nkx & Nky	128	192	224
8	2.56%	2.29%	2.16%
12	2.62%	2.40%	2.32%
16	2.61%	2.54%	2.48%

kernel size = 9 x 9

Nch \ Nkx & Nky	128	192	224
8	3.04%	2.88%	2.82%
12	2.97%	2.80%	2.86%
16	3.06%	2.80%	2.87%

Figure 6-1. **(a)** Workflow of the Monte Carlo simulation for analyzing the spectral property of a block-wise Hankel matrix. **(b)** Examples of singular value distributions from a block-wise Hankel matrix and a 2D random matrix, along with the predicted Marchenko-Pastur (MP) distribution, for different simulated datasets. **(c)** Mean absolute errors between the singular value distributions of the block-wise Hankel and random matrices and the MP distribution. The low errors show that the singular value distribution from a block-wise Hankel matrix is close to the MP distribution across different kernel sizes, number of coils, and matrix sizes.

6.2.2 KLEANER Denoising

In our KLEANER denoising pipeline, (**Figure 6-2**). the multi-coil k-space data were first decorrelated[163] using pre-scan calibration data. Coil and contrast dimensions were concatenated into a single dimension. A block-Hankel matrix was constructed using multi-coil multi-contrast 2D or 3D k-space patches. For PI-undersampled k-space datasets, we first specified an undersampling pattern and identifying patches with the same pattern across the k-space data, including the autocalibration signal (ACS) region (**Figure 6-2(c,d)**). It can be applied on data undersampled with GRAPPA[174] or Controlled Aliasing In Parallel Imaging Results IN Higher Acceleration (CAIPIRINHA)[180] with different acceleration ratios. Please note that non-sampled k-space data (i.e., zeros) were not included in the constructed block-Hankel matrix as it would distort the overall noise characteristics. Based on the spectral property of a block-Hankel matrix (previous section), we estimated the noise variance using the approach outlined in previous RMT denoising methods[150]. Optimal singular value shrinkage[162] was then applied to suppress the additive Gaussian noise. Finally, the denoised block-Hankel matrix was reshaped back to the original data dimensions, and other standard reconstruction processes such as inverse Fourier transform or PI reconstruction were performed.

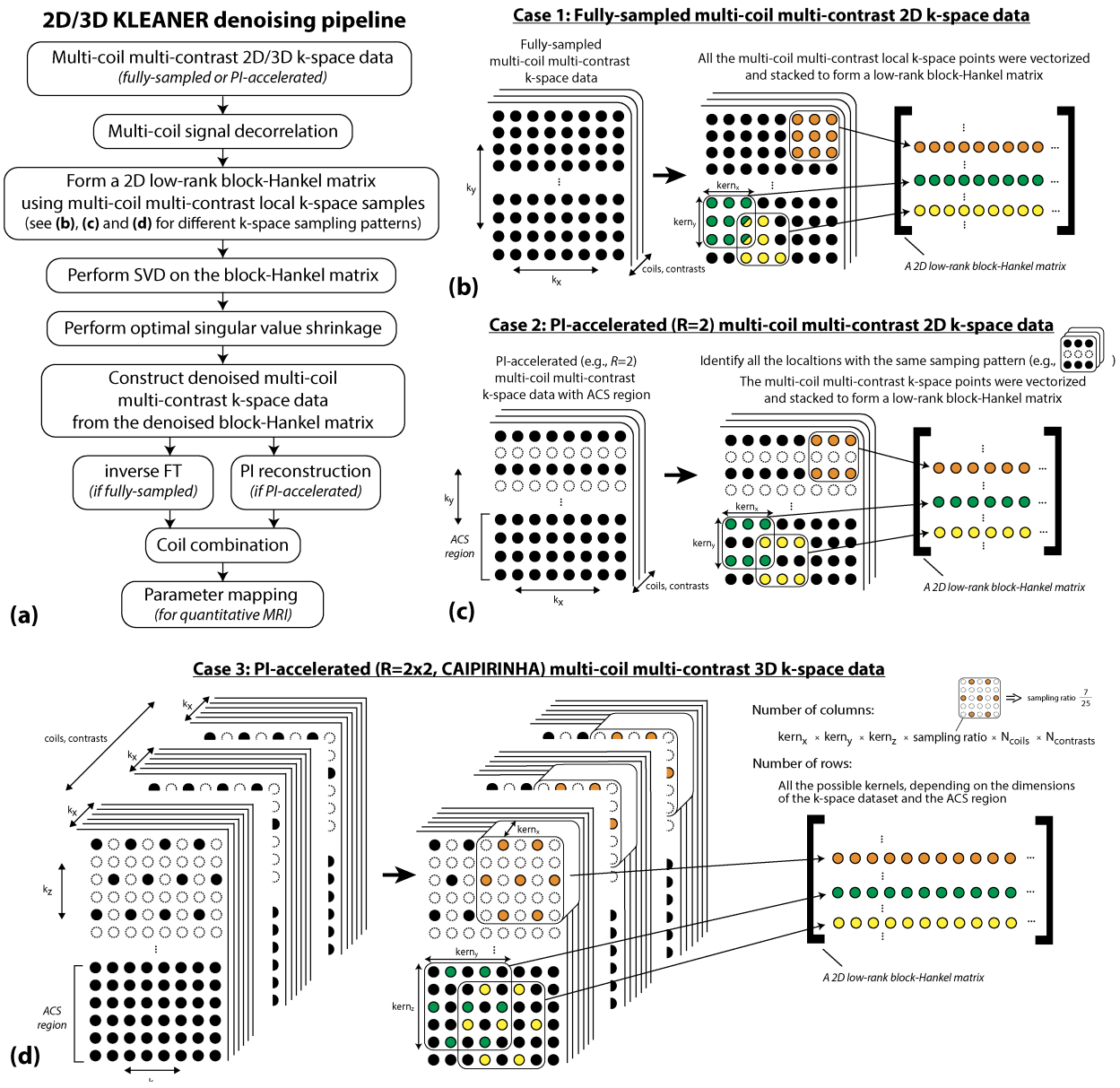

Figure 6-2. (a) KLEANER reconstruction pipeline. After signal decorrelation, a 2D low-rank block-Hankel matrix is constructed using multi-coil multi-contrast local k-space samples. Singular value decomposition (SVD) and optimal singular value shrinkage are applied on the block-Hankel matrix to suppress the additive Gaussian noise in the k-space. Data are reshaped back to the original data dimension. Standard Fourier or parallel imaging (PI) reconstruction can be used for the denoised k-space data. **(b)** Example of constructing a block-Hankel matrix from 2D fully-sampled multi-coil multi-contrast k-space data. **(c)** Example of constructing a block-Hankel matrix from 2D PI-accelerated multi-coil multi-contrast k-space data. **(d)** Example of constructing a block-Hankel matrix from 3D PI-accelerated (e.g., using Controlled Aliasing In Parallel Imaging Results IN Higher Acceleration [CAIPIRINHA]) multi-coil multi-contrast k-space data. PI: parallel imaging. SVD: singular value decomposition. FFT: Fast Fourier Transform.

6.2.3 Phantom Experiment

We scanned a standard American College of Radiology (ACR) phantom using a 3D multi-echo GRE sequence on a whole-body 0.55T system (prototype MAGNETOM Aera, Siemens Healthineers) with high-performance gradients. Phased-array receiver coils (18-channel spine array and 6-channel body array) were used, and there were N_c=12 activated coil channels during the scans. Key parameters included TE = (2.16, 4.32, 6.48, 8.64, 10.8, 12.96) ms, TR=14.8 ms, flip angle=25°, field-of-view (FoV)= 320x320 mm^2, matrix size=254x352, number of slices=10, resolution=0.8x0.8 mm^2, slice thickness=5 mm. Two scans, one with fully-sampled data and one with GRAPPA (*R*=2), were acquired. Data were processed using 3D KLEANER with a patch size of [5,5,5]. To verify that KLEANER mainly suppressed Gaussian noise, we analyzed the distribution of the complex-valued signal residuals (i.e., difference before and after KLEANER). We measured the kurtosis and skewness of the signal residual, performed Anderson-Darling normality tests ($p<0.05$ considered significant), and plotted the quantile-quantile (Q-Q) plots by comparing with a Gaussian distribution. We compared with results from 4 scan averages and with image-based RMT denoising (using a patch size of [5,5,5]). Note that for image-based RMT denoising in GRAPPA (*R*=2) datasets, PI reconstruction with g-factor correction was applied before the denoising process and images across multiple coils were used for low-rank matrix construction, as demonstrated in previous RMT denoising works[151,152]. Apparent SNR (aSNR) defined as mean signal divided by noise standard deviation[181] were measured for each method.

We further investigated the PDFF and R_2* quantification accuracy using a reference phantom (Calimetrix, Madison, Wisconsin) with seven PDFF-only (0% to 100%) and ten R_2*-only vials (17.7 to 1009.5 s^{-1} measured at 1.5T, provided by the vendor). We acquired data using

the same 3D multi-echo gradient-echo Dixon MRI research application sequence[26]. Key sequence parameters, based on findings from our Monte Carlo simulation, included N_e=6 with TEs = (2.16, 4.32, 6.48, 8.64, 10.8, 12.96) ms, TR = 14.7 ms, FA = 8°, field-of-view = 300x300 mm^2, matrix size = 192×192, and slice thickness = 5 mm. PI with acceleration factor of 2 was used. The concordance correlation coefficient (ρ_c)[165] between the measured PDFF and R_2* values versus the reference were calculated to assess agreement. Linear regression was also performed.

6.2.4 *In Vivo* Liver Experiment

In an IRB-approved HIPAA-compliant study, we scanned 10 subjects, including 4 with fatty liver. We scanned with the same 3D multi-echo GRE sequence and the same body array coil used in the phantom scan with updated sequence parameters including FoV=300x300 mm^2, matrix size=192x192, flip angle=8°, and scan time = 19 seconds (GRAPPA *R*=2, single breath-hold). KLEANER was applied on the 3D k-space data with dimensions 224x124x10x54, representing 224 frequency encoding points, a total of 124 phase encoding lines, 10 k_z encoding steps, and with 54 indicating a combined dimension from 9 coils and 6 gradient echoes. A 3D kernel size of [5,5,5] was used for 3D KLEANER denoising. We compared with results from 3D image-based RMT denoising which used a [5,5,5] patch size. Proton-density fat fraction (PDFF) maps were reconstructed by fitting the multi-echo images to a fat-water signal model with 7-peak fat spectrum[70] and a single R_2* term. Since a reference MR spectroscopy sequence for fat quantification was not yet available on the prototype 0.55T scanner, we only compared the mean PDFF values in results with or without denoising using regions of interest (ROIs) drawn in the

liver. Three liver ROIs were placed in three different axial slices in each subject while avoiding large vessels[36].

We also scanned one volunteer with the same sequence but with CAIPIRINHA (R=2x2) acquisition to demonstrate the capability of KLEANER for handling a different undersampling pattern.

6.3 Results

6.3.1 Phantom Denoising Results

Denoising results in the ACR phantom are shown in **Figure 6-3(a,b)**. The signal residual in an individual coil image only showed noise-like components, even in the GRAPPA (R=2) case with aliased signals. The kurtosis and skewness of the signal residual were close to 3 and 0, respectively. The normality test could not reject the null hypothesis (i.e., that the distribution is Gaussian), with p value larger than 0.05. Results of coil-combined images from average=1, average=4, and average=1+ two different denoising methods are shown in **Figure 6-3(c,d)**. In the GRAPPA (R=2) case, the resolution grid was largely obscured in the average=1 image. Both image-based RMT and KLEANER denoising suppressed the noise and provide similar improvements in aSNR, which were 3-fold higher than that from average=1 (no denoising).

Figure 6-4(a) shows reconstructed PDFF and R_2* maps from scan in the reference phantom. Both image-based RMT and KLEANER denoising improve the visual quality of PDFF and R_2* maps. **Figure 6-4(b,c)** show the PDFF and R_2* agreement results. KLEANER had close agreements with the reference and the image-based RMT denoising results in both PDFF and R2* (all ρ_c>0.993).

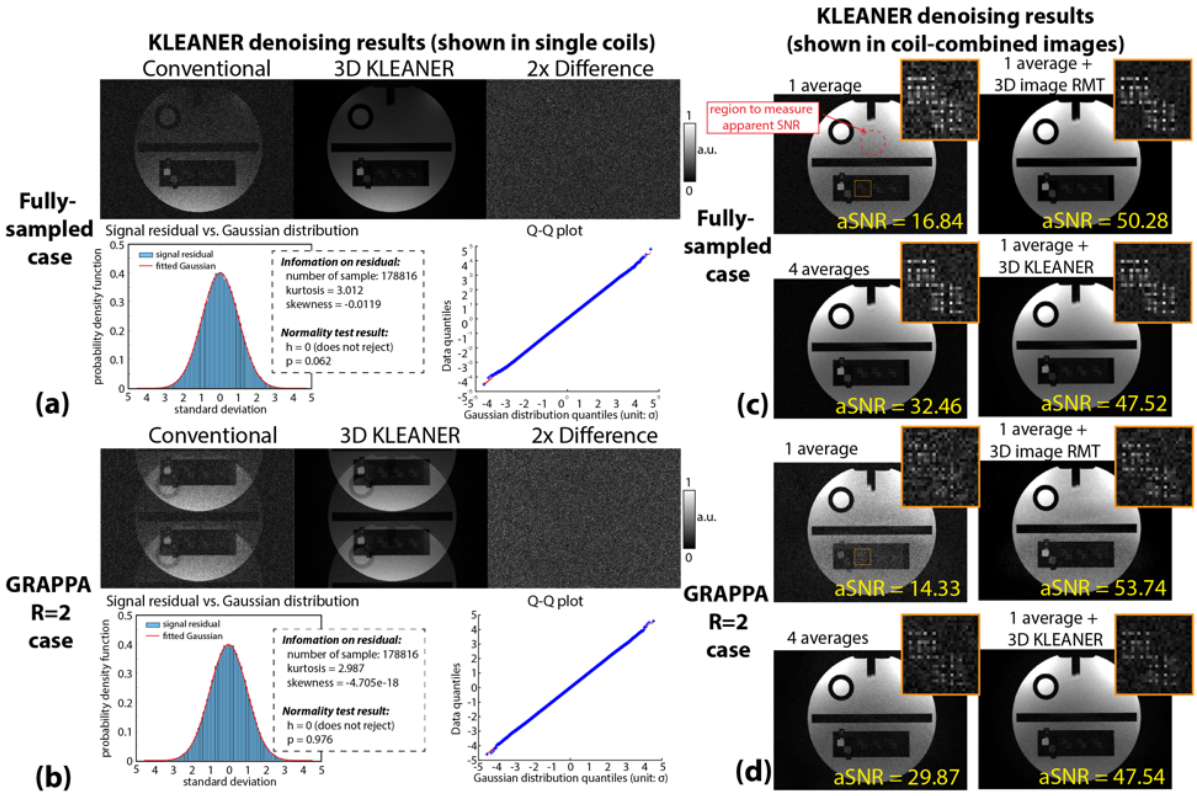

Figure 6-3. ACR phantom at 0.55T. **(a,b)** 3D KLEANER denoising results in fully-sampled and GRAPPA (*R*=2) cases. The signal residuals showed no phantom structures. Normality tests did not reject the hypothesis of Gaussian distribution. **(c,d)** Coil-combined images after reconstruction. Both image-based RMT and KLEANER showed higher aSNR than the one-average and four-average results.

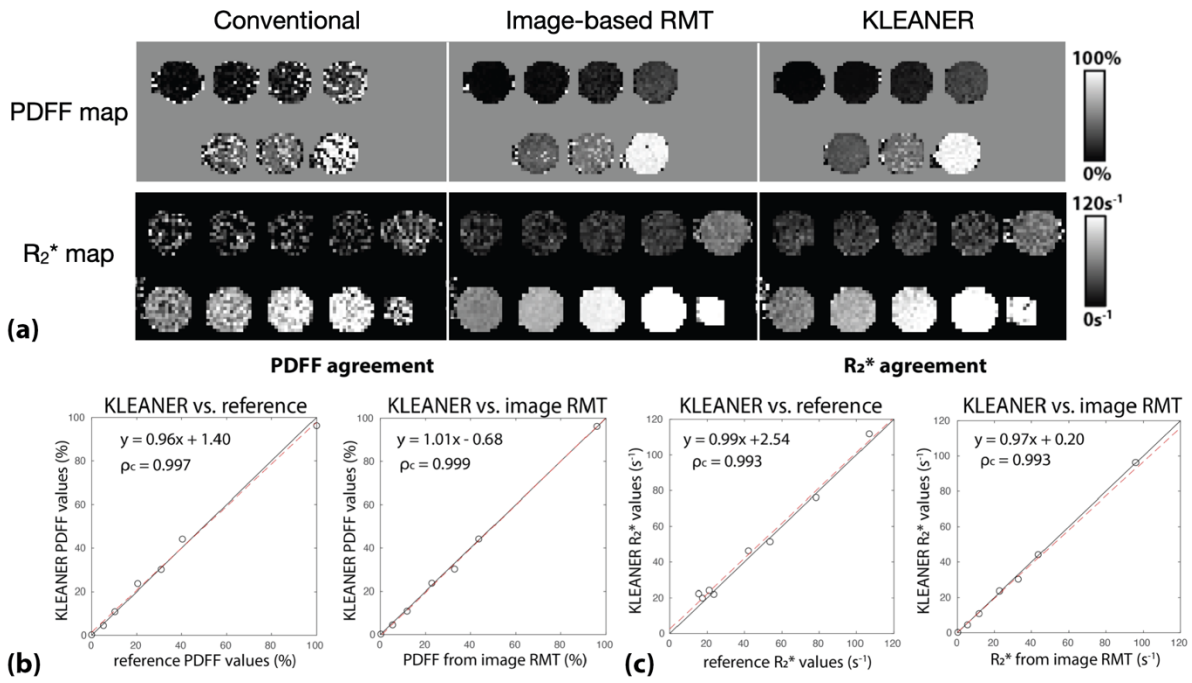

Figure 6-4. (a) PDFF and R_2* map from conventional reconstruction, image-based RMT denoising and KLEANER denoising. **(b,c)** PDFF and R_2* agreement between KLEANER denoising versus the reference and between KLEANER denoising versus image-based RMT denoising.

6.3.2 *In Vivo* Liver Denoising Results

Figure 6-5 shows *in vivo* liver denoising results in single coils. No structured tissue signal was observed in the signal residual, and the signal residual was not significantly different from a Gaussian distribution using the normality test.

Figure 6-6 compares conventional reconstruction and KLEANER results in the liver from two representative subjects with different liver PDFF levels. Noise was suppressed in both the 3rd and the 6th echo images. PDFF bias was observed in GRAPPA results, especially in the subject with low PDFF (<5%). KLEANER suppressed the noise in the multi-echo images and therefore reduced PDFF bias. In addition, KLEANER greatly reduced the noise in R_2* maps.

Figure 6-7 compares results from conventional reconstruction, image-based denoising and KLEANER denoising. The conventional reconstruction results (i.e., no denoising) exhibited PDFF quantification errors due to low SNR in the images (consistent with previous work[53]), which tended to occur around the center. Both denoising methods suppressed image noise and reduced quantification errors in PDFF maps. However, image-based RMT denoising can contribute to blurring or over-smoothing in the PDFF map.

Figure 6-8 shows the Bland-Altman plots for liver PDFF and R_2* measurement between KLEANER denoising results and image-based RMT denoising results. The MD of PDFF was 0.32% and the MD of R_2* was -0.43 s^{-1}. The small biases demonstrate close agreements of PDFF and R_2* between two denoising results.

Figure 6-9 shows the correlation plots of standard deviation of PDFF and R_2* in liver ROIs. Image-based RMT denoising had smaller standard deviations, potentially contributed to over-smoothing.

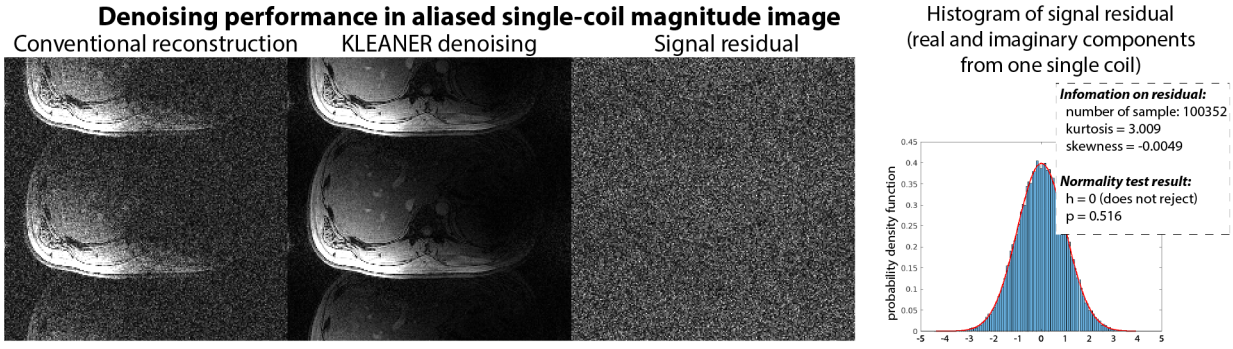

Figure 6-5. KLEANER denoising performance in an aliased single-coil image. The signal residual does not show tissue structures.

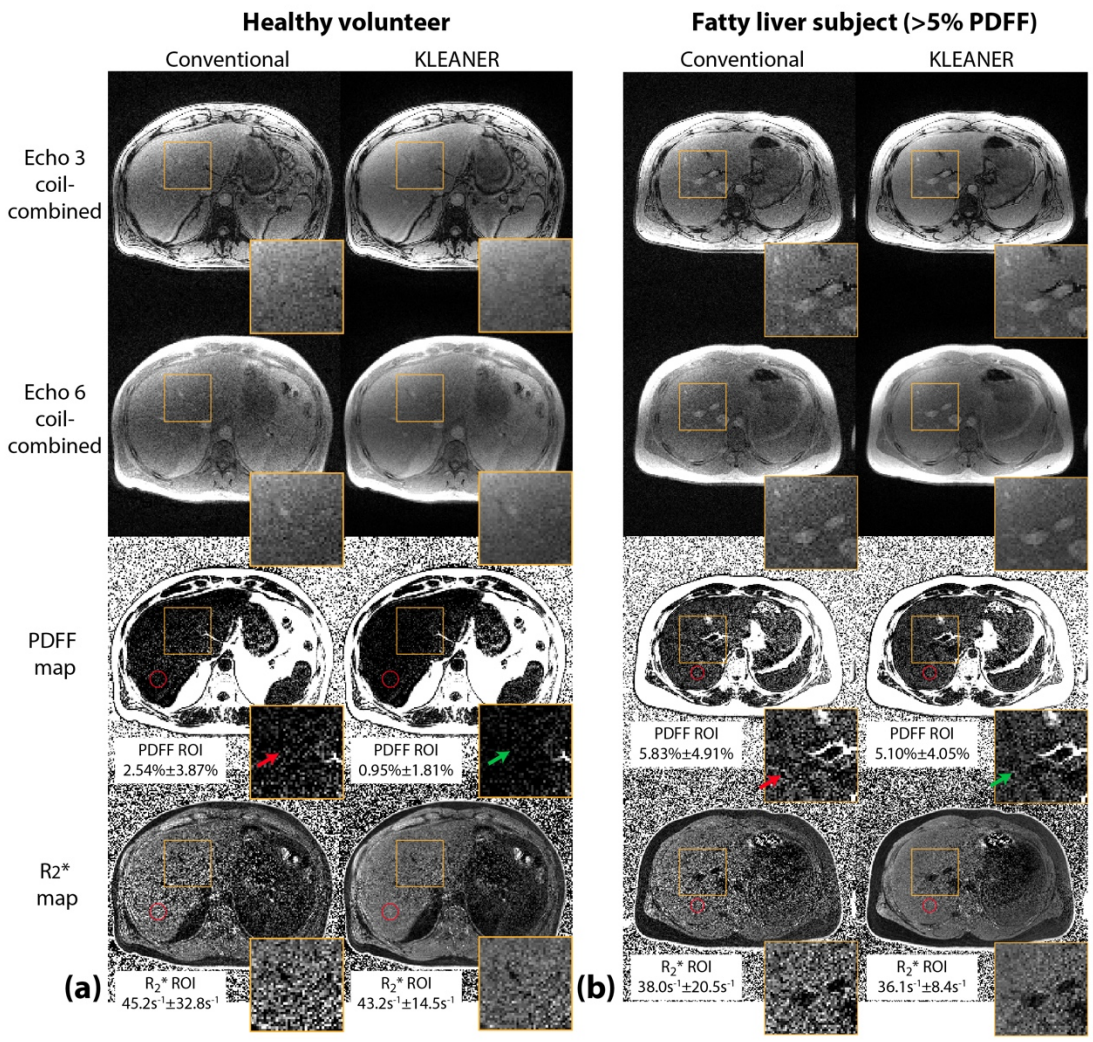

Figure 6-6. Coil-combined magnitude images, PDFF and R_2* maps from liver MRI scans (GRAPPA, *R*=2) in 2 subjects with different liver PDFF levels: **(a)** a 49-year-old male with BMI 29.1kg/m^2, **(b)** a 29-year-old male with BMI 31.7kg/m^2. KLEANER suppressed noise in the coil-combined images (3rd and 6th echo images shown). Bias in the PDFF measurements was reduced using KLEANER compared to conventional method (see green arrows versus red arrows), especially in the low PDFF case. R_2* maps were less noisy after KLEANER processing.

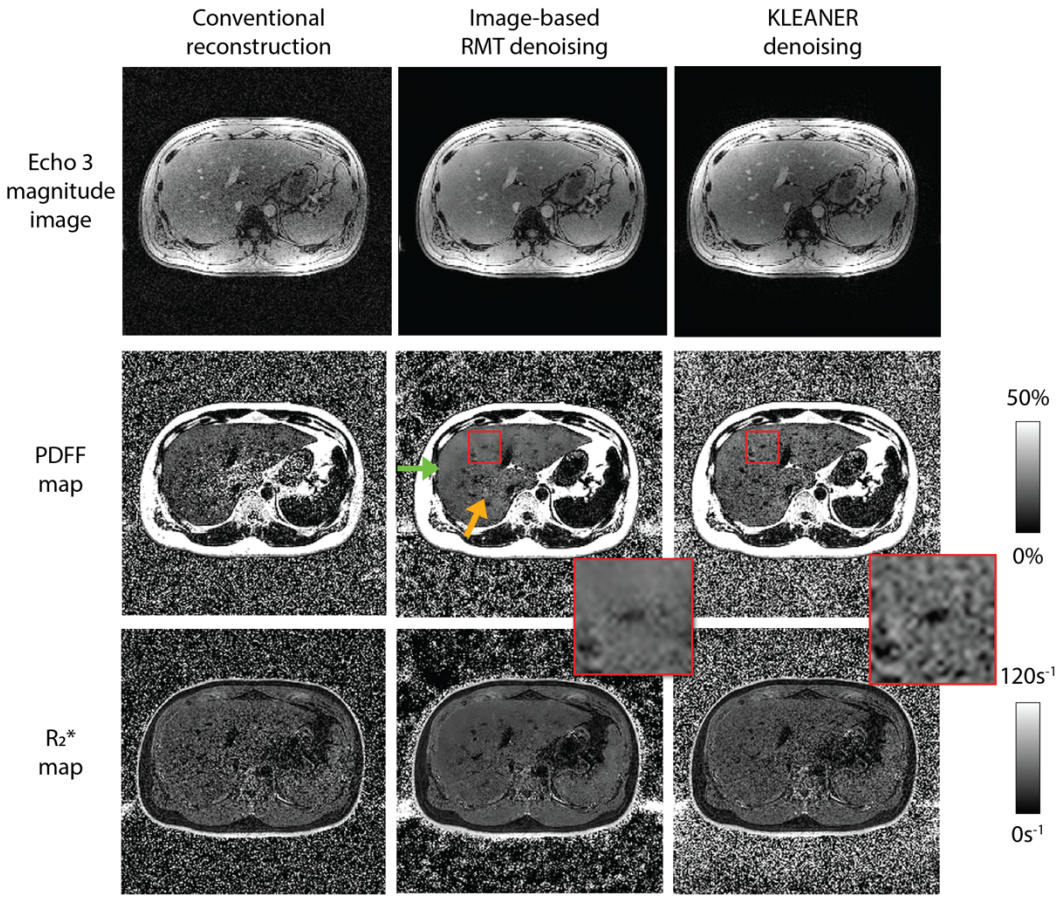

Figure 6-7. Comparison of reconstructed images from conventional reconstruction, image-based RMT denoising and KLEANER denoising. Blurring (zoomed-in patch) and inhomogeneity (green and yellow arrows) are observed in PDFF map from image-based denoising.

Figure 6-10 shows reconstruction results from a liver scan with CAIPIRINHA (R=2x2) acceleration. With CAIPIRINHA acceleration, the scan can achieve a whole-liver coverage. KLEANER denoising can effectively suppress noise in the images, reduce PDFF quantification errors, and reduce noisy measurements in the R_2* map.

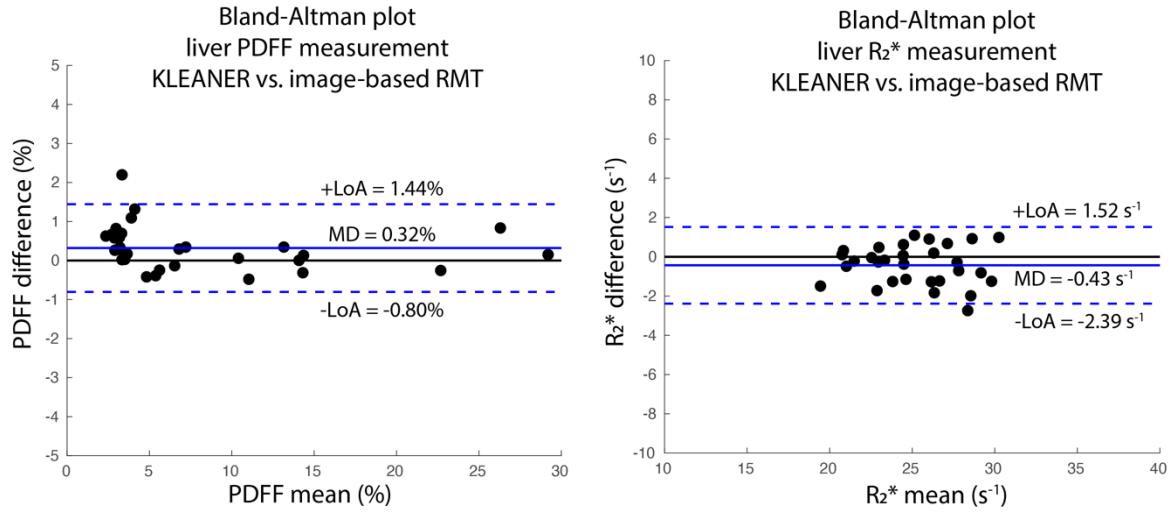

Figure 6-8. Bland-Altman plots for liver PDFF and R_2* measurements between KLEANER denoising results and image-based RMT denoising results. MD: mean difference. LoA: 95% limits of agreement.

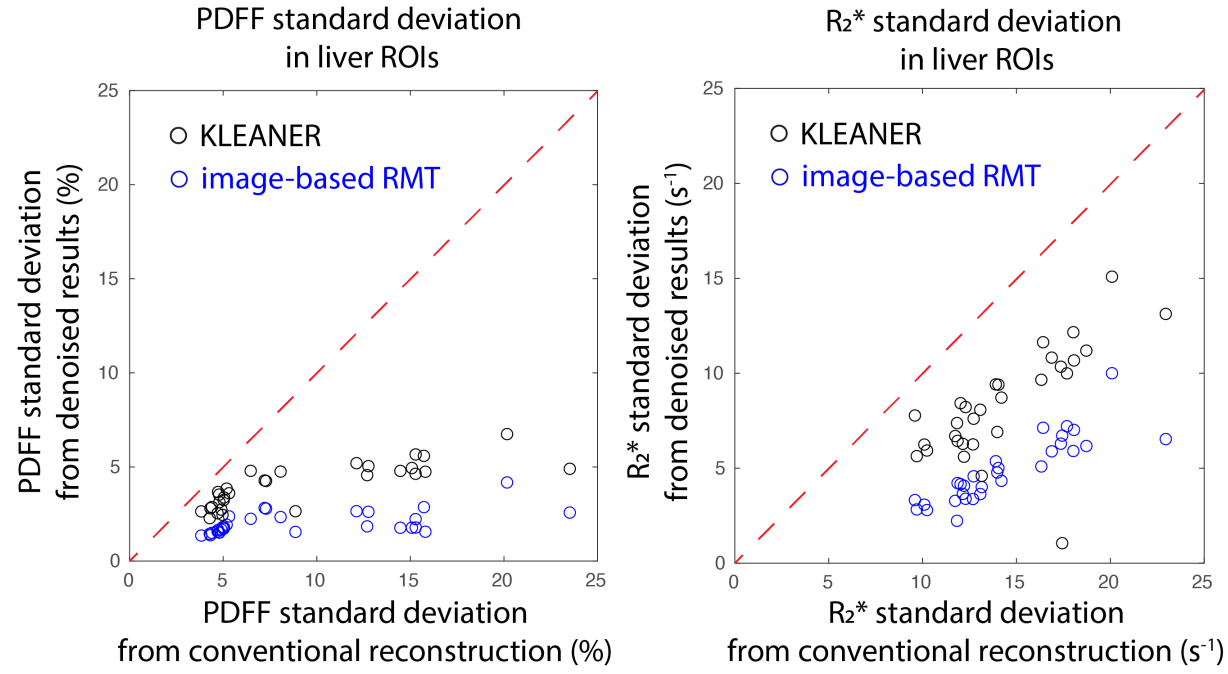

Figure 6-9. Correlation plots of PDFF and R_2* standard deviations in liver ROIs between KLEANER denoising and image-based RMT denoising versus conventional reconstruction.

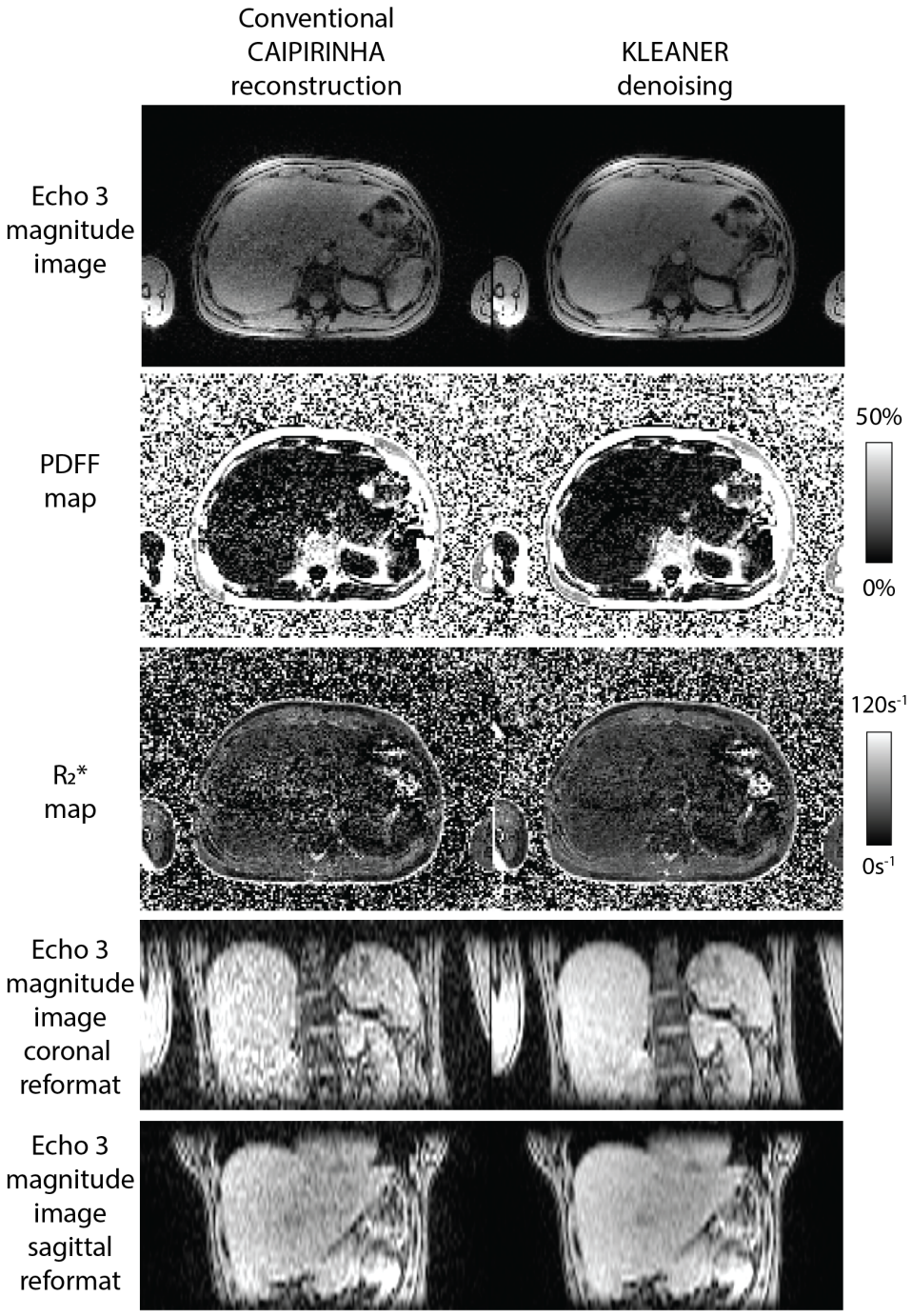

Figure 6-10. Images and quantitative maps from a liver scan with CAIPIRINHA acceleration (*R*=2x2) reconstructed using the conventional CAIPIRINHA algorithm and KLEANER denoising.

6.4 Discussion

Low SNR in MRI datasets is a fundamental limitation in many applications, and denoising continues to be an active direction of research[54]. Inspired by image-domain RMT and adopting an alternative k-space perspective on low-rank denoising for MRI, we presented KLEANER, showing its capability of removing only the additive Gaussian noise components directly in k-space. We achieved 3-fold aSNR improvement in the phantom images at 0.55T and demonstrated noise reduction and improved quantitative maps in the *in vivo* application.

The capability for k-space denoising using a low-rank block-Hankel matrix has been mentioned in the Low-Rank modelling of Local k-Space Neighborhoods (LORAKS) technique[179]. However, it was only applied on fully-sampled simulated single-coil datasets and required an iterative algorithm with manually chosen regularization parameters. In contrast, our proposed KLEANER technique is compatible with undersampled multi-coil data, non-iterative, and has an objective approach to estimate the noise level and perform singular value shrinkage for noise suppression.

In the *in vivo* results, we found that the means of the quantitative parameters were similar using either image-based RMT or KLEANER denoising. However, spatial smoothing was observed in results from image-based RMT denoising. Other recent works also pointed out potential spatial resolution issues in image-based RMT denoising from signal "leaking" across voxels[182,183]. This smoothing effect can be dependent on the underlying tissue signal rank and the patch size. KLEANER can potentially be an alternative approach to prevent smoothing. Another advantage of KLEANER over image-based RMT denoising is that KLEANER can directly suppress noise in the originally-acquired k-space data without concerns of distorting the

Gaussian noise characteristics from previous reconstruction processes (e.g., PI), which can potentially make KLEANER compatible with more MRI applications.

There are limitations of the proposed KLEANER technique. First, calculating singular values from a 2D block-Hankel matrix can become computationally impractical when dealing with large 3D multi-coil multi-contrast datasets. More memory efficient implementations are required for such applications. Second, a theory-based explanation for the singular value distribution of a block-Hankel matrix has not yet been established. Further study of theoretical noise distribution of a block-Hankel matrix is required to better understand the limitations and promise of the KLEANER technique.

6.5 Conclusion

We proposed a k-space denoising method, termed KLEANER, using a low-rank block-Hankel matrix constructed from multi-coil multi-contrast k-space data combined with singular value shrinkage. We demonstrated that KLEANER achieved a 3-fold increase in apparent SNR in phantom experiments at 0.55T and successful denoising for quantitative liver MRI at 0.55T. Compared with image-based RMT denoising methods, KLEANER showed similar noise reduction performance in images and sharper features in quantitative maps.

This work is under review:

Shu-Fu Shih, Zhaohuan Zhang, Bilal Tasdelen, Ecrin Yagiz, Xiaodong Zhong, Sophia X. Cui, Krishna S. Nayak, Holden H. Wu. “K-space Low-rankness Enabled Additive NoisE Removal (KLEANER) for Multi-Coil Multi-Contrast MRI”. (*Under review*)

CHAPTER 7

Summary and Future Studies

7.1 Dissertation Summary

In this dissertation, we developed several reconstruction and motion compensation techniques to improve MRI liver PDFF and R_2* quantification. First, we developed a phase-preserving beamforming-based technique to effectively reduce radial streaking artifacts from system imperfections. We demonstrated how this technique can be integrated with motion-resolved reconstruction to improve self-gated free-breathing stack-of-radial MRI liver PDFF and R_2* quantification. Second, we developed an uncertainty-aware physics-driven deep learning network for rapid reconstruction of PDFF and R_2* maps from self-gated free-breathing stack-of-radial MRI. We demonstrated that the uncertainty maps generated from the network can be used to predict quantification errors and improve reliability of deep learning reconstruction results. Third, we developed a compressed sensing reconstruction model with non-rigid motion compensation to improve and accelerate self-gated free-breathing stack-of-radial MRI liver PDFF and R_2* quantification. The quantitative maps from non-rigid motion compensated compressed sensing reconstruction exhibit sharper features with less artifacts when compared with motion-resolved reconstruction. Fourth, we developed and evaluated image-based and k-space-based denoising techniques to improve quantification accuracy and precision of breath-holding 3D Cartesian-based liver PDFF and R_2* quantification at 0.55T.

Techniques introduced in this dissertation provide 1) accelerated and motion-robust free-breathing liver PDFF and R_2* quantification using stack-of-radial MRI at 3T and 2) accurate and precise breath-holding Cartesian-based liver PDFF and R_2* quantification at 0.55T. Furthermore,

we discussed limitations of the current techniques and potential solutions. There are also opportunities worth considering for clinical applications.

7.2 Standardization of Free-Breathing PDFF and R_2* Imaging Biomarkers

A meta-analysis of over 1500 participants on linearity and bias of breath-holding liver MRI PDFF at 1.5T or 3T showed a regression slope of 0.97 and a mean bias of -0.13% versus PDFF estimated by breath-holding MRS[184]. With a meta-analysis of more than 400 participants, liver MRI PDFF at 1.5T or 3T showed high repeatability and reproducibility coefficients of 2.99% and 4.12%[184]. A systematic phantom study further showed PDFF (from breath-holding acquisitions) was accurate across vendors, imaging centers, and field strengths (1.5T and 3T) using vendor-specific acquisition and reconstruction[167]. This sets a performance benchmark that free-breathing CSE MRI techniques should aim to achieve.

While several research works[36-38,185] evaluated the accuracy or repeatability of free-breathing PDFF and R_2* quantification with respect to breath-holding techniques in patients with hepatic steatosis and/or liver iron overload, these works only studied limited numbers of subjects. One factor limiting a large-scale evaluation is that most of these free-breathing MRI techniques are based on recently developed research sequences that are still being refined and are not widely available. Future efforts to standardize and disseminate free-breathing CSE MRI techniques will be essential to enable studies that evaluate their quantitative performance across in larger populations, especially in subjects with limited breath-holding capability. Repeatability and reproducibility analysis across different scanners and different sites are also necessary for widespread adoption of the free-breathing techniques in clinical settings.

Many free-breathing MRI techniques showed that R_2* is sensitive to motion, which can vary substantially from scan to scan. This can make systematic analysis of the linearity, bias, and repeatability of R_2* measured from free-breathing scans challenging. Compared to liver PDFF, which has an active Quantitative Imaging Biomarker Alliance (QIBA) profile in development [186], more efforts are required to establish R_2* as an accurate and repeatable MR imaging biomarker in the liver. The insights gained from standardizing breath-holding MRI R_2* mapping will also benefit the continued development of free-breathing MRI R_2* mapping.

7.3 Pilot Tone Motion Tracking Technique

Although different navigators, including a readout line interleaved within the sequence or the k-space DC signal, have been shown to effectively estimate respiratory motion in free-breathing MRI scans, they can be inadequate in cases with higher breathing frequency or irregular changes in breathing patterns. Recent studies[187] have found that a rapidly updating navigator (e.g., a navigator echo for every TR) allows better motion gating and can lead to better image quality in radial scans. A recent motion tracking technique, Pilot Tone (PT)[188,189], is a promising motion surrogate signal with a high sampling frequency. During the scan acquisition, a stand-alone device continuously transmits a radiofrequency signal with a frequency within the MRI readout bandwidth. The respiratory information modulated and encoded in the PT signal is acquired along with the k-space data, and can be extracted for motion-gated reconstruction. Since the PT signal is encoded in every k-space readout, the temporal resolution of this type of motion surrogate signal is the same as TR, and notably higher than conventional navigators.

In the reconstruction techniques introduced in Chapter 3 and 4, all the radial spokes with same angle (but different k_z encoding) were binned into the same motion state. As the number of

k_z encoding increases (i.e., larger volumetric coverage), this strategy can lead to suboptimal results because the liver position can have noticeable changes in the position within the acquisition time of one radial angle along all the k_z points. With PT motion tracking techniques, scans with a larger volumetric coverage can become more motion-robust. To combine PT motion tracking with the techniques introduced in Chapters 3 and 4, one only needs to replace the motion gating method, and the other reconstruction modules (e.g., non-rigid motion compensation technique in Chapter 4) can still be applicable.

7.4 Free-Breathing Techniques for Body Composition Measurement in Fetuses and Infants

Body composition analysis quantifies the amount and proportions of body tissue compartments[190]. Quantifying the adipose tissue volume and fat content is one essential aspect of body composition analysis. Studies have reported the body composition analysis may provide information or insights into the risk of metabolic syndrome[190,191]. Studies to develop automatic segmentation pipelines that can help MRI-based body composition analysis are also being actively investigated[192,193].

MRI-based free-breathing PDFF quantification techniques developed in this dissertation can serve as valuable tools for measurement of body composition, especially in challenging cases such as in fetuses[194] and in infants[195] where motion is inevitable during MRI scan acquisitions. Compared to adult and pediatric volunteers and patients investigated in this dissertation, the motion patterns in fetuses and infants are usually more variable and bulk motion is more likely to happen. The non-rigid motion compensation framework introduced in Chapter 4 can be a

promising approach to capture the non-rigid motion and improve image quality and quantification accuracy.

We observed that streaking artifacts usually come from the arms in adult and pediatric scans where a standard axial plane is prescribed. In fetal scans, where the imaging plane needs to be adjusted, the streaking artifact patterns and sources resulting from system imperfections will be more difficult to identify. **Figure 7-1** shows an example with streaking artifacts coming from outside of the prescribed field-of-view obscuring the important imaging features. Key sequence parameter for this scan included: TEs = (1.23, 2.46, 3.69, 4.92, 6.15, 7.38) ms, TR = 8.85 ms, flip angle = 5°, field-of-view = 460 mm x 460 mm, slice thickness = 1.5 mm, in-phane resolution = 1.6 mm x 1.6 mm. In this case, applying beamforming-based streaking reduction with manual selection of an interference region can greatly improve the image quality and resulting PDFF map. Studies to develop an automatic pipeline for interference region identification in fetal MRI cases can be conducted in the future.

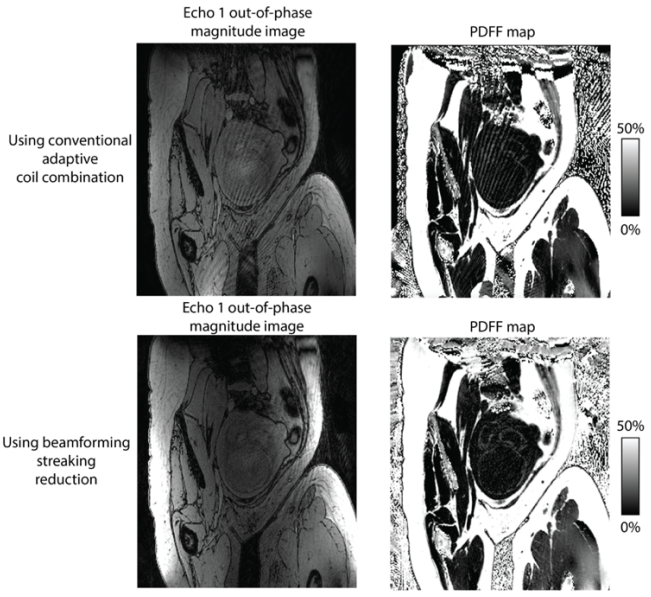

Figure 7-1. Reconstructed images and PDFF maps from a fetal scan using free-breathing 3D stack-of-radial multi-echo gradient-echo MRI. Beamforming-based coil combination can be used to suppress the radial streaking artifacts in the images and corresponding PDFF map.

7.5 Other Non-Cartesian Trajectories for Free-Breathing PDFF and R_2* Quantification

We focused on the 3D stack-of-radial trajectory for free-breathing liver PDFF and R_2* quantification in this dissertation. Other non-Cartesian trajectories, such as 3D radial[196] and 3D cones[197], have also been proposed to quantify liver PDFF and R_2* during a free-breathing acquisition. Despite having different artifact patterns, these non-Cartesian trajectories may also be affected by system imperfections. The artifact suppression technique developed in Chapter 2 may be applied in these datasets. These different methods involve different motion estimation and different reconstruction methods. An extensive study on their motion robustness, diagnostic image quality and quantification accuracy should be conducted in the future.

7.6 Free-Breathing Multi-Parametric Quantitative Liver MRI

There is also a trend towards developing multi-parametric quantitative liver MRI techniques[198] (one example from a MASLD patient shown in **Figure 7-2**). In addition to the quantitative parameters PDFF and R_2* for fat and iron, studies also found associations between liver T_1 and fibrosis and cirrhosis[199,200], associations between liver T_2 and hepatic steatosis and inflammation[201], and associations between liver stiffness measured by magnetic resonance elastography (MRE) and liver fibrosis[202]. Sequences for joint quantification of multiple parameters[203-205] could not only address the confounding factors together but also provide additional information for liver assessment. As multi-parametric quantitative liver MRI with a large volumetric coverage is difficult to achieve in one breath-hold, free-breathing quantitative MRI becomes an attractive approach[206,207]. Reconstruction and motion compensation techniques

developed in Chapters 2 to 4 can be adapted to these applications to reduce streaking artifacts, improve motion robustness, and shorten the acquisition times.

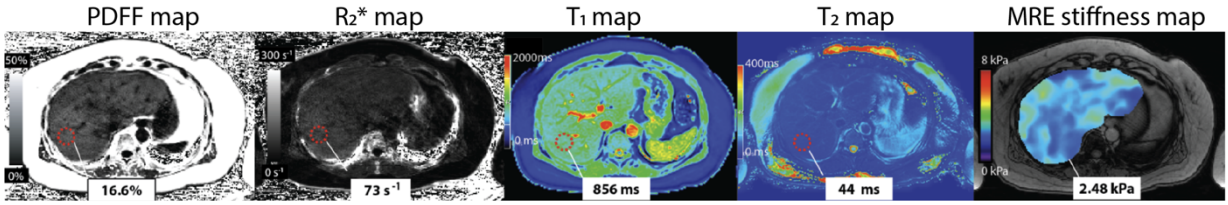

Figure 7-2. Example of multi-parametric quantitative liver MRI from a MASLD patient.

7.7 Free-Breathing PDFF and R_2* Quantification at Lower Field Strengths

We demonstrated that image-based and k-space-based denoising techniques can both improve the Cartesian-based PDFF and R_2* quantification at 0.55T in Chapters 5 and 6. However, further improvement in the image resolution and the volumetric coverage is limited by the breath-holding requirement. Free-breathing motion compensation and reconstruction techniques introduced in Chapters 2 to 4 can be applied for free-breathing PDFF and R_2* quantification at 0.55T using the 3D stack-of-radial MRI sequence.

An example of free-breathing liver PDFF and R_2* quantification results at 0.55T using a multi-echo 3D stack-of-radial Dixon MRI sequence is shown in **Figure 7-3**. Key parameters include TE = (2.17, 4.32, 6.47, 8.62, 10.77, 12.92) ms, TR = 16.2 ms, flip angle = 5°, field of view = 300 mm x 300 mm, matrix size = 192x192x30, radial spokes = 454 (1.5x radial oversampling), scan time = 4 minutes 24 seconds. Motion-gating can reduce the signal blurring around the liver dome and improve sharpness in tissue features. With motion-resolved compressed sensing reconstruction, the streaking artifacts can be further suppressed to improve the diagnostic quality of the PDFF and R_2* maps. Although the free-breathing techniques can

greatly increase the volumetric coverage (e.g., 30 slices compared with the breath-holding Cartesian technique in Chapter 5 with only 8 slices), the acquisition time is long. Further investigation on radial undersampling and the usage of non-rigid motion compensation for scan acceleration (as introduced in Chapter 4) in the future can improve this application at 0.55T.

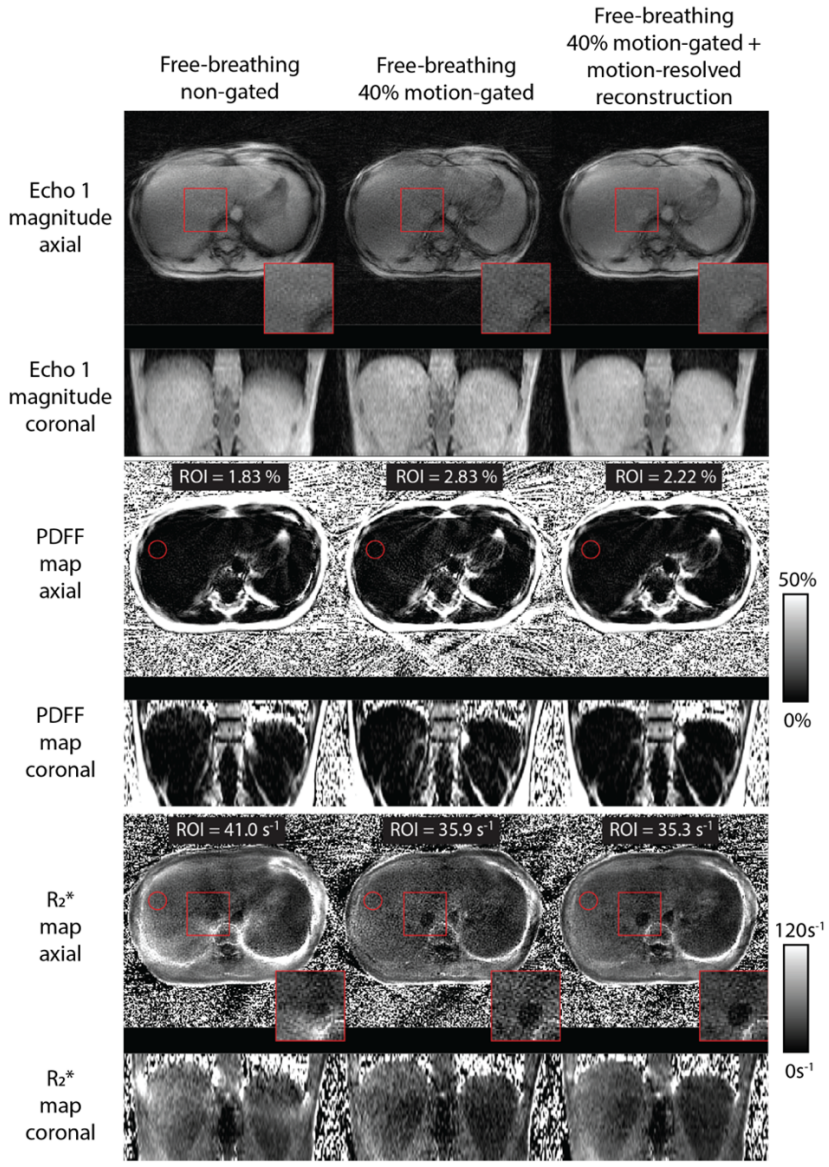

Figure 7-3. Example of free-breathing liver PDFF and R_2* quantification at 0.55T using a 3D stack-of-radial multi-echo gradient-echo sequence. Self-gated motion-resolved reconstruction can reduce blurring and the elevated R_2* values caused by breathing motion.

7.8 k-Space Denoising Techniques for Other Applications

We validated image-based and k-space-based denoising techniques to improve PDFF and R_2* quantification at 0.55T in Chapters 5 and 6. The denoising techniques rely on assumptions of Gaussian-distributed noise and low-rank properties in images or k-space data and can potentially applied in other MRI applications that require noise reduction.

Preliminary works have been performed to investigate image-based RMT denoising in high-resolution diffusion-weighted MRI in the prostate at 3T[155]. Here, we compared KLEANER denoising results versus the image-based denoising results in **Figure 7-4**. Similar to the results in liver scans (Chapter 6), no tissue structures were seen in the residual signal after KLEANER denoising. Image-based RMT and KLEANER denoising both effectively suppressed noise. Apparent diffusion coefficient (ADC) maps from image-based RMT denoising show smoothing, while KLEANER preserved sharper features. Analysis of the ADC maps showed that both denoising techniques provided similar mean ADC values in the prostate. Using standard-resolution diffusion MRI as reference, both denoising techniques reduced the bias in ADC values due to noise (conventional reconstruction without denoising).

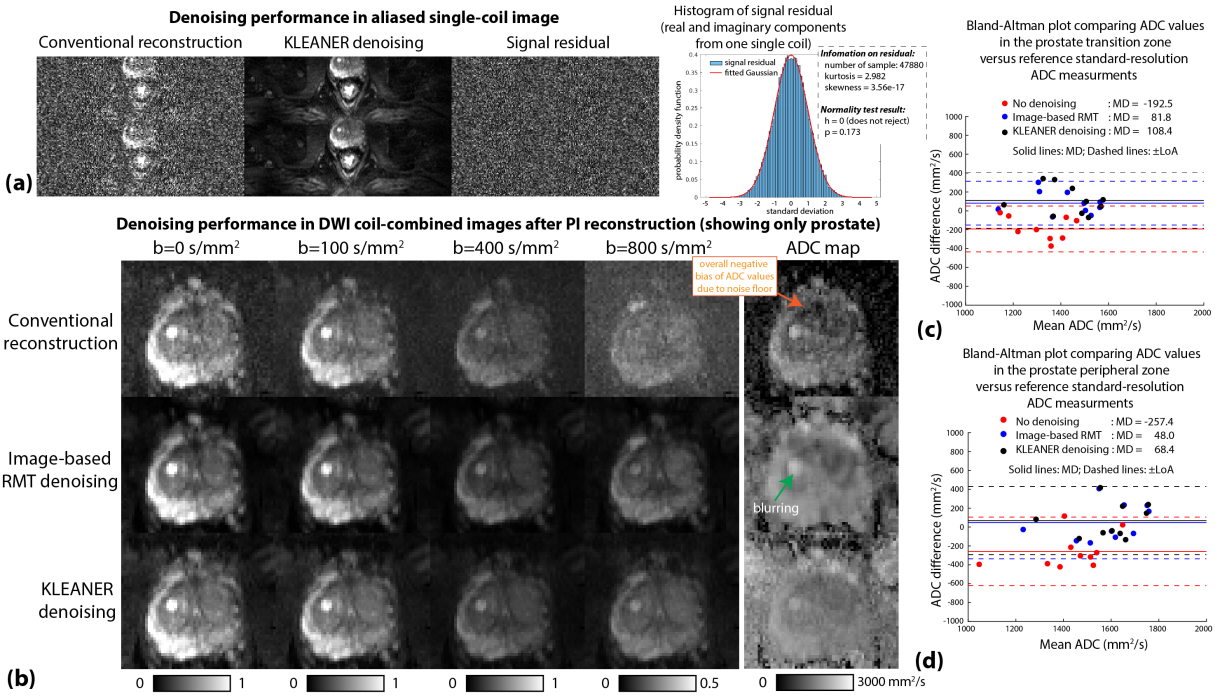

Figure 7-4. **(a)** KLEANER denoising in one single coil before parallel imaging reconstruction. Normality test on the signal residual does not reject the null hypothesis that it is Gaussian distributed. **(b)** The coil combined images and apparent diffusion coefficient (ADC) maps reconstructed from conventional reconstruction and different denoising methods. **(c-d)** Bland-Altman plots comparing ADC values in the prostate transition and peripheral zones.

7.9 Conclusion

In this dissertation, we presented several different reconstruction and motion compensation techniques for liver fat and R_2* quantification. We focused on the technical development, and further validation in large cohorts, including patients with fatty liver and hepatic overload, across different MRI systems and different institutions can pave the way for wide clinical adoption of these advanced techniques. Alongside the technical developments, standardization of the quantitative imaging biomarkers, PDFF and R_2*, is also required for extensive validation of different advanced reconstruction methods.

BIBLIOGRAPHY

1. Rinella ME, Lazarus JV, Ratziu V, Francque SM, Sanyal AJ, Kanwal F, Romero D, Abdelmalek MF, Anstee QM, Arab JP. A multi-society Delphi consensus statement on new fatty liver disease nomenclature. Ann Hepatol 2023;29(1):101133.
2. Chan W-K, Chuah K-H, Rajaram RB, Lim L-L, Ratnasingam J, Vethakkan SR. Metabolic dysfunction-associated Steatotic Liver disease (MASLD): a state-of-the-art review. J Obes Metab Syndr 2023;32(3):197.
3. Ye Q, Zou B, Yeo YH, Li J, Huang DQ, Wu Y, Yang H, Liu C, Kam LY, Tan XXE. Global prevalence, incidence, and outcomes of non-obese or lean non-alcoholic fatty liver disease: a systematic review and meta-analysis. Lancet Gastroenterol Hepatol 2020;5(8):739-752.
4. Quek J, Chan KE, Wong ZY, Tan C, Tan B, Lim WH, Tan DJH, Tang ASP, Tay P, Xiao J. Global prevalence of non-alcoholic fatty liver disease and non-alcoholic steatohepatitis in the overweight and obese population: a systematic review and meta-analysis. Lancet Gastroenterol Hepatol 2023;8(1):20-30.
5. Byrne CD, Targher G. NAFLD: a multisystem disease. J Hepatol 2015;62(1):S47-S64.
6. Benedict M, Zhang X. Non-alcoholic fatty liver disease: An expanded review. World J Hepatol 2017;9(16):715.
7. Kasper P, Martin A, Lang S, Kuetting F, Goeser T, Demir M, Steffen H-M. NAFLD and cardiovascular diseases: a clinical review. Clin Res Cardiol 2021;110:921-937.
8. Huang DQ, El-Serag HB, Loomba R. Global epidemiology of NAFLD-related HCC: trends, predictions, risk factors and prevention. Nat Rev Gastroenterol Hepatol 2021;18(4):223-238.

9. Wree A, Broderick L, Canbay A, Hoffman HM, Feldstein AE. From NAFLD to NASH to cirrhosis—new insights into disease mechanisms. Nat Rev Gastroenterol Hepatol 2013;10(11):627-636.
10. Anstee QM, Targher G, Day CP. Progression of NAFLD to diabetes mellitus, cardiovascular disease or cirrhosis. Nat Rev Gastroenterol Hepatol 2013;10(6):330-344.
11. Nalbantoglu I, Brunt EM. Role of liver biopsy in nonalcoholic fatty liver disease. World J Gastroenterol 2014;20(27):9026-9037.
12. Sumida Y, Nakajima A, Itoh Y. Limitations of liver biopsy and non-invasive diagnostic tests for the diagnosis of nonalcoholic fatty liver disease/nonalcoholic steatohepatitis. World J Gastroenterol 2014;20(2):475.
13. Ratziu V, Charlotte F, Heurtier A, Gombert S, Giral P, Bruckert E, Grimaldi A, Capron F, Poynard T, Group LS. Sampling variability of liver biopsy in nonalcoholic fatty liver disease. Gastroenterology 2005;128(7):1898-1906.
14. Deugnier Y, Turlin B. Pathology of hepatic iron overload. World J Gastroenterol 2007;13(35):4755.
15. Hsu CC, Senussi NH, Fertrin KY, Kowdley KV. Iron overload disorders. Hepatol Commun 2022;6(8):1842-1854.
16. Batts KP. Iron overload syndromes and the liver. Mod Pathol 2007;20(1):S31-S39.
17. Alústiza JM, Castiella A, De Juan MD, Emparanza JI, Artetxe J, Uranga M. Iron overload in the liver diagnostic and quantification. Eur J Radiol 2007;61(3):499-506.
18. Sirlin CB, Reeder SB. Magnetic resonance imaging quantification of liver iron. Magn Reson Imaging Clin 2010;18(3):359-381.

19. Reeder SB, Cruite I, Hamilton G, Sirlin CB. Quantitative assessment of liver fat with magnetic resonance imaging and spectroscopy. J Magn Reson Imaging 2011;34(4):729-749.

20. Eggers H, Börnert P. Chemical shift encoding-based water–fat separation methods. J Magn Reson Imaging 2014;40(2):251-268.

21. Reeder SB, Hu HH, Sirlin CB. Proton density fat-fraction: a standardized MR-based biomarker of tissue fat concentration. J Magn Reson Imaging 2012;36(5):1011-1014.

22. Eggers H, Börnert P. Chemical shift encoding-based water–fat separation methods. Journal of Magnetic Resonance Imaging 2014;40(2):251-268.

23. Horng DE, Hernando D, Hines CD, Reeder SB. Comparison of R2* correction methods for accurate fat quantification in fatty liver. Journal of Magnetic Resonance Imaging 2013;37(2):414-422.

24. Hernando D, Kramer JH, Reeder SB. Multipeak fat-corrected complex R2* relaxometry: theory, optimization, and clinical validation. Magnetic resonance in medicine 2013;70(5):1319-1331.

25. Yu H, Shimakawa A, McKenzie CA, Brodsky E, Brittain JH, Reeder SB. Multiecho water-fat separation and simultaneous R estimation with multifrequency fat spectrum modeling. Magnetic Resonance in Medicine: An Official Journal of the International Society for Magnetic Resonance in Medicine 2008;60(5):1122-1134.

26. Zhong X, Nickel MD, Kannengiesser SA, Dale BM, Kiefer B, Bashir MR. Liver fat quantification using a multi-step adaptive fitting approach with multi-echo GRE imaging. Magnetic resonance in medicine 2014;72(5):1353-1365.

27. Chavhan GB, Babyn PS, Vasanawala SS. Abdominal MR imaging in children: motion compensation, sequence optimization, and protocol organization. Radiographics 2013;33(3):703-719.

28. Courtier J, Rao AG, Anupindi SA. Advanced imaging techniques in pediatric body MRI. Pediatric radiology 2017;47(5):522-533.

29. Speidel T, Meyer CH, Rasche V. Non-cartesian imaging. Advances in Magnetic Resonance Technology and Applications. Volume 6: Elsevier; 2022. p 481-498.

30. Zaitsev M, Maclaren J, Herbst M. Motion artifacts in MRI: A complex problem with many partial solutions. J Magn Reson Imaging 2015;42(4):887-901.

31. Hernando D, Levin YS, Sirlin CB, Reeder SB. Quantification of liver iron with MRI: state of the art and remaining challenges. Journal of Magnetic Resonance Imaging 2014;40(5):1003-1021.

32. Zhong X, Armstrong T, Nickel MD, Kannengiesser SA, Pan L, Dale BM, Deshpande V, Kiefer B, Wu HH. Effect of respiratory motion on free-breathing 3D stack-of-radial liver relaxometry and improved quantification accuracy using self-gating. Magnetic resonance in medicine 2020;83(6):1964-1978.

33. Zhong X, Hu HH, Armstrong T, Li X, Lee YH, Tsao TC, Nickel MD, Kannengiesser SA, Dale BM, Deshpande V, Kiefer B, Wu HH. Free-Breathing Volumetric Liver and Proton Density Fat Fraction Quantification in Pediatric Patients Using Stack-of-Radial MRI With Self-Gating Motion Compensation. Journal of Magnetic Resonance Imaging 2021;53(1):118-129.

34. Zhang T, Cheng JY, Chen Y, Nishimura DG, Pauly JM, Vasanawala SS. Robust self-navigated body MRI using dense coil arrays. Magn Reson Med 2016;76(1):197-205.

35. Feng L, Axel L, Chandarana H, Block KT, Sodickson DK, Otazo R. XD-GRASP: golden-angle radial MRI with reconstruction of extra motion-state dimensions using compressed sensing. Magn Reson Med 2016;75(2):775-788.

36. Armstrong T, Zhong X, Shih S-F, Felker E, Lu DS, Dale BM, Wu HH. Free-breathing 3D stack-of-radial MRI quantification of liver fat and R2* in adults with fatty liver disease. Magnetic Resonance Imaging 2022;85:141-152.

37. Schneider M, Benkert T, Solomon E, Nickel D, Fenchel M, Kiefer B, Maier A, Chandarana H, Block KT. Free-breathing fat and R2* quantification in the liver using a stack-of-stars multi-echo acquisition with respiratory-resolved model-based reconstruction. Magnetic resonance in medicine 2020;84(5):2592-2605.

38. Tan Z, Unterberg-Buchwald C, Blumenthal M, Scholand N, Schaten P, Holme C, Wang X, Raddatz D, Uecker M. Free-Breathing Liver Fat, R* 2 and B 0 Field Mapping Using Multi-Echo Radial FLASH and Regularized Model-based Reconstruction. IEEE Transactions on Medical Imaging 2022.

39. Feng L. Golden-angle radial MRI: basics, advances, and applications. Journal of Magnetic Resonance Imaging 2022;56(1):45-62. doi: 10.1109/TMI.2013.2293974.

40. Block KT, Uecker M. Simple method for adaptive gradient-delay compensation in radial MRI. Proceedings of the 19th Annual Meeting of ISMRM, Montreal, Canada; 2011.

41. Arnold TC, Freeman CW, Litt B, Stein JM. Low-field MRI: clinical promise and challenges. Journal of Magnetic Resonance Imaging 2023;57(1):25-44.

42. Campbell-Washburn AE, Ramasawmy R, Restivo MC, Bhattacharya I, Basar B, Herzka DA, Hansen MS, Rogers T, Bandettini WP, McGuirt DR. Opportunities in interventional

and diagnostic imaging by using high-performance low-field-strength MRI. Radiology 2019;293(2):384-393.

43. Marques JP, Simonis FF, Webb AG. Low-field MRI: An MR physics perspective. Journal of magnetic resonance imaging 2019;49(6):1528-1542.

44. Marques JP, Simonis FF, Webb AG. Low-field MRI: An MR physics perspective. J Magn Reson Imaging 2019;49(6):1528-1542.

45. Sarracanie M, Salameh N. Low-field MRI: how low can we go? A fresh view on an old debate. Front Phys 2020;8:172.

46. Shetty AS, Ludwig DR, Ippolito JE, Andrews TJ, Narra VR, Fraum TJ. Low-Field-Strength Body MRI: Challenges and Opportunities at 0.55 T. RadioGraphics 2023;43(12):e230073. doi: 10.1148/rg.230073.

47. Campbell-Washburn AE, Mancini C, Conrey A, Edwards L, Shanbhag S, Wood J, Xue H, Kellman P, Bandettini WP, Thein SL. Evaluation of Hepatic Iron Overload Using a Contemporary 0. 55 T MRI System. J Magn Reson Imaging 2022;55(6):1855-1863.

48. Nayak KS, Cui SX, Tasdelen B, Yagiz E, Weston S, Zhong X, Ahlgren A. Body composition profiling at 0.55 T: Feasibility and precision. Magn Reson Med 2023;90(3):1114-1120.

49. Chandarana H, Bagga B, Huang C, Dane B, Petrocelli R, Bruno M, Keerthivasan M, Grodzki D, Block KT, Stoffel D. Diagnostic abdominal MR imaging on a prototype low-field 0.55 T scanner operating at two different gradient strengths. Abdom Radiol 2021;46(12):5772-5780.

50. Guenthner C, Dillinger H, Boernert P, Kozerke S. Three-point dixon abdominal water/fat separation using a lower-field 0.75 T MRI. Proc ISMRM; 2021; virtual. p 1283.

51. Campbell-Washburn AE, Mancini C, Conrey A, Edwards L, Shanbhag S, Wood J, Xue H, Kellman P, Bandettini WP, Thein SL. Evaluation of Hepatic Iron Overload Using a Contemporary 0. 55 T MRI System. Journal of Magnetic Resonance Imaging 2022;55(6):1855-1863. doi: 10.1002/jmri.27950.

52. Reeder SB, Cruite I, Hamilton G, Sirlin CB. Quantitative assessment of liver fat with magnetic resonance imaging and spectroscopy. Journal of Magnetic Resonance Imaging 2011;34(4):729-749. doi: 10.1002/jmri.22580.

53. Shih S-F, Cui S, Zhong X, Tasdelen B, Yagiz E, Nayak K, Wu HH. Free-breathing liver fat quantification using radial acquisition on a high-performance 0.55 T MRI system. 2022. ISMRM.

54. Mohan J, Krishnaveni V, Guo Y. A survey on the magnetic resonance image denoising methods. Biomedical signal processing and control 2014;9:56-69. doi: 10.1016/j.bspc.2013.10.007.

55. Manjón JV, Carbonell-Caballero J, Lull JJ, García-Martí G, Martí-Bonmatí L, Robles M. MRI denoising using non-local means. Medical image analysis 2008;12(4):514-523. doi: 10.1016/j.media.2008.02.004.

56. Knoll F, Bredies K, Pock T, Stollberger R. Second order total generalized variation (TGV) for MRI. Magnetic resonance in medicine 2011;65(2):480-491. doi: 10.1002/mrm.22595.

57. Armstrong T, Dregely I, Stemmer A, Han F, Natsuaki Y, Sung K, Wu HH. Free-breathing liver fat quantification using a multiecho 3 D stack-of-radial technique. Magnetic resonance in medicine 2018;79(1):370-382.

58. Li Z, Fu Z, Keerthivasan M, Bilgin A, Johnson K, Galons J-P, Vedantham S, Martin DR, Altbach MI. Rapid high-resolution volumetric T1 mapping using a highly accelerated stack-of-stars Look Locker technique. Magnetic Resonance Imaging 2021;79:28-37.

59. Du J, Thornton F, Fain S, Korosec F, Browning F, Grist T, Mistretta C. Artifact reduction in undersampled projection reconstruction MRI of the peripheral vessels using selective excitation. Magnetic Resonance in Medicine: An Official Journal of the International Society for Magnetic Resonance in Medicine 2004;51(5):1071-1076.

60. Moussavi A, Untenberger M, Uecker M, Frahm J. Correction of gradient-induced phase errors in radial MRI. Magnetic resonance in medicine 2014;71(1):308-312.

61. Block KT, Uecker M. Simple method for adaptive gradient-delay compensation in radial MRI. Proc ISMRM, Montreal, Canada; 2011.

62. Xue Y, Yu J, Kang HS, Englander S, Rosen MA, Song HK. Automatic coil selection for streak artifact reduction in radial MRI. Magnetic resonance in medicine 2012;67(2):470-476.

63. Mandava S, Keerthivasan MB, Martin DR, Altbach MI, Bilgin A. Radial streak artifact reduction using phased array beamforming. Magnetic resonance in medicine 2019;81(6):3915-3923.

64. Zhang L, Armstrong T, Li X, Wu HH. A variable flip angle golden-angle-ordered 3D stack-of-radial MRI technique for simultaneous proton resonant frequency shift and T1-based thermometry. Magnetic resonance in medicine 2019;82(6):2062-2076.

65. Walsh DO, Gmitro AF, Marcellin MW. Adaptive reconstruction of phased array MR imagery. Magnetic Resonance in Medicine: An Official Journal of the International Society for Magnetic Resonance in Medicine 2000;43(5):682-690.

66. Van Trees HL. Optimum array processing: Part IV of detection, estimation, and modulation theory: John Wiley & Sons; 2002.

67. Kim D, Cauley SF, Nayak KS, Leahy RM, Haldar JP. Region-optimized virtual (ROVir) coils: Localization and/or suppression of spatial regions using sensor-domain beamforming. Magnetic Resonance in Medicine 2021;86(1):197-212.

68. Ronneberger O, Fischer P, Brox T. U-net: Convolutional networks for biomedical image segmentation. International Conference on Medical image computing and computer-assisted intervention; 2015. Springer. p 234-241. doi: 10.1007/978-3-319-24574-4_28.

69. Haimovich AM, Bar-Ness Y. An eigenanalysis interference canceler. IEEE Transactions on signal processing 1991;39(1):76-84.

70. Ren J, Dimitrov I, Sherry AD, Malloy CR. Composition of adipose tissue and marrow fat in humans by 1H NMR at 7 Tesla. Journal of lipid research 2008;49(9):2055-2062.

71. Rinella ME. Nonalcoholic fatty liver disease: a systematic review. Jama 2015;313(22):2263-2273.

72. Vernon G, Baranova A, Younossi Z. Systematic review: the epidemiology and natural history of non-alcoholic fatty liver disease and non-alcoholic steatohepatitis in adults. Alimentary pharmacology & therapeutics 2011;34(3):274-285.

73. Williams R. Global challenges in liver disease. Hepatology 2006;44(3):521-526.

74. Powell EE, Jonsson JR, Clouston AD. Steatosis: co-factor in other liver diseases. Hepatology 2005;42(1):5-13. doi: 10.1002/hep.20750.

75. Yokoo T, Browning JD. Fat and iron quantification in the liver: past, present, and future. Top Magn Reson Imaging 2014;23(2):73-94.

76. Aigner E, Weiss G, Datz C. Dysregulation of iron and copper homeostasis in nonalcoholic fatty liver. World J Hepatol 2015;7(2):177. doi: 10.4254/wjh.v7.i2.177.

77. Dongiovanni P, Fracanzani AL, Fargion S, Valenti L. Iron in fatty liver and in the metabolic syndrome: a promising therapeutic target. J Hepatol 2011;55(4):920-932. doi: 10.1016/j.jhep.2011.05.008.

78. Milic S, Mikolasevic I, Orlic L, Devcic E, Starcevic-Cizmarevic N, Stimac D, Kapovic M, Ristic S. The role of iron and iron overload in chronic liver disease. Med Sci Monit 2016;22:2144. doi: 10.12659/MSM.896494.

79. Wood MJ, Skoien R, Powell LW. The global burden of iron overload. Hepatol Int 2009;3(3):434-444. doi: 10.1007/s12072-009-9144-z.

80. Zoller H, Tilg H. Nonalcoholic fatty liver disease and hepatocellular carcinoma. Metabolism 2016;65(8):1151-1160. doi: 10.1016/j.metabol.2016.01.010.

81. Hines CD, Frydrychowicz A, Hamilton G, Tudorascu DL, Vigen KK, Yu H, McKenzie CA, Sirlin CB, Brittain JH, Reeder SB. T1 independent, T2* corrected chemical shift based fat–water separation with multi-peak fat spectral modeling is an accurate and precise measure of hepatic steatosis. J Magn Reson Imaging 2011;33(4):873-881. doi: 10.1002/jmri.22514.

82. Armstrong T, Ly KV, Murthy S, Ghahremani S, Kim GHJ, Calkins KL, Wu HH. Free-breathing quantification of hepatic fat in healthy children and children with nonalcoholic fatty liver disease using a multi-echo 3-D stack-of-radial MRI technique. Pediatr Radiol 2018;48(7):941-953. doi: 10.1007/s00247-018-4127-7.

83. Zhong X, Armstrong T, Nickel MD, Kannengiesser SA, Pan L, Dale BM, Deshpande V, Kiefer B, Wu HH. Effect of respiratory motion on free-breathing 3D stack-of-radial liver

relaxometry and improved quantification accuracy using self-gating. Magn Reson Med 2020;83(6):1964-1978.

84. Schneider M, Benkert T, Solomon E, Nickel D, Fenchel M, Kiefer B, Maier A, Chandarana H, Block KT. Free-breathing fat and R2* quantification in the liver using a stack-of-stars multi-echo acquisition with respiratory-resolved model-based reconstruction. Magn Reson Med 2020;84(5):2592-2605.

85. Cui C, Wu X, Newell JD, Jacob M. Fat water decomposition using globally optimal surface estimation (GOOSE) algorithm. Magnetic resonance in medicine 2015;73(3):1289-1299.

86. Hernando D, Kellman P, Haldar J, Liang ZP. Robust water/fat separation in the presence of large field inhomogeneities using a graph cut algorithm. Magnetic Resonance in Medicine: An Official Journal of the International Society for Magnetic Resonance in Medicine 2010;63(1):79-90.

87. Lustig M, Donoho D, Pauly JM. Sparse MRI: The application of compressed sensing for rapid MR imaging. Magn Reson Med 2007;58(6):1182-1195. doi: 10.1002/mrm.21391.

88. Lee D, Yoo J, Tak S, Ye JC. Deep residual learning for accelerated MRI using magnitude and phase networks. IEEE Trans Biomed Eng 2018;65(9):1985-1995.

89. Schlemper J, Caballero J, Hajnal JV, Price A, Rueckert D. A deep cascade of convolutional neural networks for MR image reconstruction. International Conference on Information Processing in Medical Imaging; 2017. Springer. p 647-658. doi: 10.1007/978-3-319-59050-9_51.

90. Han Y, Yoo J, Kim HH, Shin HJ, Sung K, Ye JC. Deep learning with domain adaptation for accelerated projection-reconstruction MR. Magn Reson Med 2018;80(3):1189-1205. doi: 10.1002/mrm.27106.

91. Kofler A, Dewey M, Schaeffter T, Wald C, Kolbitsch C. Spatio-temporal deep learning-based undersampling artefact reduction for 2D radial cine MRI with limited training data. IEEE Trans Med Imaging 2019;39(3):703-717. doi: 10.1109/TMI.2019.2930318.

92. Lv J, Chen K, Yang M, Zhang J, Wang X. Reconstruction of undersampled radial free-breathing 3D abdominal MRI using stacked convolutional auto-encoders. Med Phys 2018;45(5):2023-2032. doi: 10.1002/mp.12870.

93. El-Rewaidy H, Fahmy AS, Pashakhanloo F, Cai X, Kucukseymen S, Csecs I, Neisius U, Haji-Valizadeh H, Menze B, Nezafat R. Multi-domain convolutional neural network (MD-CNN) for radial reconstruction of dynamic cardiac MRI. Magn Reson Med 2021;85(3):1195-1208. doi: 10.1002/mrm.28485.

94. Goldfarb JW, Craft J, Cao JJ. Water–fat separation and parameter mapping in cardiac MRI via deep learning with a convolutional neural network. J Magn Reson Imaging 2019;50(2):655-665. doi: 10.1002/jmri.26658.

95. Andersson J, Ahlström H, Kullberg J. Separation of water and fat signal in whole-body gradient echo scans using convolutional neural networks. Magn Reson Med 2019;82(3):1177-1186. doi: 10.1002/mrm.27786.

96. Cho J, Park H. Robust water–fat separation for multi-echo gradient-recalled echo sequence using convolutional neural network. Magn Reson Med 2019;82(1):476-484. doi: 10.1002/mrm.27697.

97. Liu K, Li X, Li Z, Chen Y, Xiong H, Chen F, Bao Q, Liu C. Robust water–fat separation based on deep learning model exploring multi-echo nature of mGRE. Magn Reson Med 2021;85(5):2828-2841. doi: 10.1002/mrm.28586.

98. Jafari R, Spincemaille P, Zhang J, Nguyen TD, Luo X, Cho J, Margolis D, Prince MR, Wang Y. Deep neural network for water/fat separation: Supervised training, unsupervised training, and no training. Magn Reson Med 2021;85(4):2263-2277. doi: 10.1002/mrm.28546.

99. Edupuganti V, Mardani M, Vasanawala S, Pauly J. Uncertainty quantification in deep MRI reconstruction. IEEE Trans Med Imaging 2020;40(1):239-250. doi: 10.1109/TMI.2020.3025065.

100. Zhang Z, Romero A, Muckley MJ, Vincent P, Yang L, Drozdzal M. Reducing uncertainty in undersampled MRI reconstruction with active acquisition. Proceedings of the IEEE/CVF Conference on Computer Vision and Pattern Recognition; 2019. p 2049-2058.

101. Schlemper J, Castro DC, Bai W, Qin C, Oktay O, Duan J, Price AN, Hajnal J, Rueckert D. Bayesian deep learning for accelerated MR image reconstruction. International Workshop on Machine Learning for Medical Image Reconstruction; 2018. Springer. p 64-71.

102. Shih S-F, Kafali SG, Armstrong T, Zhong X, Calkins KL, Wu HH. Deep learning-based parameter mapping with uncertainty estimation for fat quantification using accelerated free-breathing radial MRI. 2021 IEEE 18th International Symposium on Biomedical Imaging (ISBI); 2021. IEEE. p 433-437. doi: 10.1109/ISBI48211.2021.9433938.

103. Liu F, Samsonov A, Chen L, Kijowski R, Feng L. SANTIS: sampling-augmented neural network with incoherent structure for MR image reconstruction. Magnetic resonance in medicine 2019;82(5):1890-1904.

104. Gao C, Ghodrati V, Shih S-F, Wu HH, Liu Y, Nickel MD, Vahle T, Dale B, Sai V, Felker E. Undersampling artifact reduction for free-breathing 3D stack-of-radial MRI based on a deep adversarial learning network. Magnetic resonance imaging 2023;95:70-79.

105. Ledig C, Theis L, Huszár F, Caballero J, Cunningham A, Acosta A, Aitken A, Tejani A, Totz J, Wang Z. Photo-realistic single image super-resolution using a generative adversarial network. Proceedings of the IEEE conference on computer vision and pattern recognition; 2017. p 4681-4690.

106. Ulyanov D, Vedaldi A, Lempitsky V. Instance normalization: The missing ingredient for fast stylization. arXiv preprint arXiv:160708022 2016.

107. Kendall A, Gal Y. What uncertainties do we need in bayesian deep learning for computer vision? arXiv preprint arXiv:170304977 2017.

108. Abdar M, Pourpanah F, Hussain S, Rezazadegan D, Liu L, Ghavamzadeh M, Fieguth P, Cao X, Khosravi A, Acharya UR. A review of uncertainty quantification in deep learning: Techniques, applications and challenges. Inf Fusion 2021. doi: 10.1016/j.inffus.2021.05.008.

109. Arjovsky M, Chintala S, Bottou L. Wasserstein generative adversarial networks. International conference on machine learning; 2017. PMLR. p 214-223.

110. Harris PA, Taylor R, Thielke R, Payne J, Gonzalez N, Conde JG. Research electronic data capture (REDCap)—a metadata-driven methodology and workflow process for

providing translational research informatics support. J Biomed Inform 2009;42(2):377-381. doi: 10.1016/j.jbi.2008.08.010.

111. Fu Z, Mandava S, Keerthivasan MB, Li Z, Johnson K, Martin DR, Altbach MI, Bilgin A. A multi-scale residual network for accelerated radial MR parameter mapping. Magn Reson Imaging 2020;73:152-162. doi: 10.1016/j.mri.2020.08.013.

112. Shao J, Ghodrati V, Nguyen KL, Hu P. Fast and accurate calculation of myocardial T1 and T2 values using deep learning Bloch equation simulations (DeepBLESS). Magn Reson Med 2020;84(5):2831-2845.

113. Shih S-F, Wu HH. A beamforming-based coil combination method to reduce streaking artifacts and preserve phase fidelity in radial MRI. Proceedings of the ISMRM 30th Annual Meeting; 2022. p 1697.

114. Freedman JN, Gurney-Champion OJ, Nill S, Shiarli A-M, Bainbridge HE, Mandeville HC, Koh D-M, McDonald F, Kachelrieß M, Oelfke U. Rapid 4D-MRI reconstruction using a deep radial convolutional neural network: Dracula. Radiother Oncol 2021;159:209-217. doi: 10.1016/j.radonc.2021.03.034.

115. Doneva M, Börnert P, Eggers H, Mertins A, Pauly J, Lustig M. Compressed sensing for chemical shift-based water–fat separation. Magn Reson Med 2010;64(6):1749-1759.

116. Jiang M, Yuan Z, Yang X, Zhang J, Gong Y, Xia L, Li T. Accelerating CS-MRI reconstruction with fine-tuning Wasserstein generative adversarial network. IEEE Access 2019;7:152347-152357. doi: 10.1109/ACCESS.2019.2948220.

117. Yi X, Walia E, Babyn P. Generative adversarial network in medical imaging: A review. Med Image Anal 2019;58:101552. doi: 10.1016/j.media.2019.101552.

118. Mehta R, Christinck T, Nair T, Bussy A, Premasiri S, Costantino M, Chakravarty M, Arnold DL, Gal Y, Arbel T. Propagating uncertainty across cascaded medical imaging tasks for improved deep learning inference. IEEE Trans Med Imaging 2021;41(2):360-373. doi: 10.1109/TMI.2021.3114097.

119. Liang D, Cheng J, Ke Z, Ying L. Deep magnetic resonance image reconstruction: Inverse problems meet neural networks. IEEE Signal Process Mag 2020;37(1):141-151. doi: 10.1109/MSP.2019.2950557.

120. Idilman IS, Aniktar H, Idilman R, Kabacam G, Savas B, Elhan A, Celik A, Bahar K, Karcaaltincaba M. Hepatic steatosis: quantification by proton density fat fraction with MR imaging versus liver biopsy. Radiology 2013;267(3):767-775. doi: 10.1148/radiol.13121360.

121. Gu J, Liu S, Du S, Zhang Q, Xiao J, Dong Q, Xin Y. Diagnostic value of MRI-PDFF for hepatic steatosis in patients with non-alcoholic fatty liver disease: a meta-analysis. European radiology 2019;29:3564-3573.

122. Rinella ME, Lazarus JV, Ratziu V, Francque SM, Sanyal AJ, Kanwal F, Romero D, Abdelmalek MF, Anstee QM, Arab JP. A multisociety Delphi consensus statement on new fatty liver disease nomenclature. Hepatology 2023;78(6):1966-1986.

123. Loomba R, Sanyal AJ. The global NAFLD epidemic. Nature reviews Gastroenterology & hepatology 2013;10(11):686-690.

124. Wood JC, Enriquez C, Ghugre N, Tyzka JM, Carson S, Nelson MD, Coates TD. MRI R2 and R2* mapping accurately estimates hepatic iron concentration in transfusion-dependent thalassemia and sickle cell disease patients. Blood 2005;106(4):1460-1465. doi: doi.org/10.1182/blood-2004-10-3982.

125. Hankins JS, McCarville MB, Loeffler RB, Smeltzer MP, Onciu M, Hoffer FA, Li C-S, Wang WC, Ware RE, Hillenbrand CM. R2* magnetic resonance imaging of the liver in patients with iron overload. Blood, The Journal of the American Society of Hematology 2009;113(20):4853-4855.

126. Zhong X, Nickel MD, Kannengiesser SA, Dale BM, Han F, Gao C, Shih SF, Dai Q, Curiel O, Tsao TC. Accelerated free-breathing liver fat and R 2* quantification using multi-echo stack-of-radial MRI with motion-resolved multidimensional regularized reconstruction: Initial retrospective evaluation. Magnetic Resonance in Medicine 2024.

127. Cruz G, Atkinson D, Henningsson M, Botnar RM, Prieto C. Highly efficient nonrigid motion-corrected 3D whole-heart coronary vessel wall imaging. Magnetic resonance in medicine 2017;77(5):1894-1908.

128. Zhu X, Chan M, Lustig M, Johnson KM, Larson PE. Iterative motion-compensation reconstruction ultra-short TE (iMoCo UTE) for high-resolution free-breathing pulmonary MRI. Magnetic resonance in medicine 2020;83(4):1208-1221.

129. Zeilinger MG, Kunze K-P, Munoz C, Neji R, Schmidt M, Croisille P, Heiss R, Wuest W, Uder M, Botnar RM. Non-rigid motion-corrected free-breathing 3D myocardial Dixon LGE imaging in a clinical setting. European Radiology 2022;32(7):4340-4351.

130. Feng L, Axel L, Chandarana H, Block KT, Sodickson DK, Otazo R. XD-GRASP: golden-angle radial MRI with reconstruction of extra motion-state dimensions using compressed sensing. Magnetic resonance in medicine 2016;75(2):775-788.

131. Thirion J-P. Image matching as a diffusion process: an analogy with Maxwell's demons. Medical image analysis 1998;2(3):243-260.

132. Shewchuk JR. An introduction to the conjugate gradient method without the agonizing pain. 1994.

133. Vercauteren T, Pennec X, Perchant A, Ayache N. Diffeomorphic demons: Efficient non-parametric image registration. NeuroImage 2009;45(1):S61-S72.

134. Fleet D, Weiss Y. Optical flow estimation. Handbook of mathematical models in computer vision: Springer; 2006. p 237-257.

135. Ilg E, Mayer N, Saikia T, Keuper M, Dosovitskiy A, Brox T. Flownet 2.0: Evolution of optical flow estimation with deep networks. Proceedings of the IEEE conference on computer vision and pattern recognition; 2017. p 2462-2470.

136. Küstner T, Pan J, Qi H, Cruz G, Gilliam C, Blu T, Yang B, Gatidis S, Botnar R, Prieto C. LAPNet: Non-rigid registration derived in k-space for magnetic resonance imaging. IEEE transactions on medical imaging 2021;40(12):3686-3697.

137. Li Z, Huang C, Tong A, Chandarana H, Feng L. Kz-accelerated variable-density stack-of-stars MRI. Magnetic Resonance Imaging 2023;97:56-67.

138. Artz NS, Haufe WM, Hooker CA, Hamilton G, Wolfson T, Campos GM, Gamst AC, Schwimmer JB, Sirlin CB, Reeder SB. Reproducibility of MR-based liver fat quantification across field strength: Same-day comparison between 1.5 T and 3T in obese subjects. Journal of Magnetic Resonance Imaging 2015;42(3):811-817. doi: 10.1002/jmri.24842.

139. Alam MH, Auger D, McGill L-A, Smith GC, He T, Izgi C, Baksi AJ, Wage R, Drivas P, Firmin DN. Comparison of 3 T and 1.5 T for T2* magnetic resonance of tissue iron. Journal of Cardiovascular Magnetic Resonance 2016;18:1-9. doi: 10.1186/s12968-016-0259-9.

140. Bashir MR, Zhong X, Nickel MD, Fananapazir G, Kannengiesser SA, Kiefer B, Dale BM. Quantification of hepatic steatosis with a multistep adaptive fitting MRI approach: prospective validation against MR spectroscopy. American Journal of Roentgenology 2015;204(2):297-306. doi: 10.2214/AJR.14.12457.

141. Kühn J-P, Hernando D, Muñoz del Rio A, Evert M, Kannengiesser S, Völzke H, Mensel B, Puls R, Hosten N, Reeder SB. Effect of multipeak spectral modeling of fat for liver iron and fat quantification: correlation of biopsy with MR imaging results. Radiology 2012;265(1):133-142. doi: 10.1148/radiol.12112520.

142. Tian Y, Nayak KS. New clinical opportunities of low-field MRI: heart, lung, body, and musculoskeletal. Magnetic Resonance Materials in Physics, Biology and Medicine 2024;37(1):1-14. doi: 10.1007/s10334-023-01123-w.

143. Michael AE, Heuser A, Moenninghoff C, Surov A, Borggrefe J, Kroeger JR, Niehoff JH. Does bore size matter?—A comparison of the subjective perception of patient comfort during low field (0.55 Tesla) and standard (1.5 Tesla) MRI imaging. Medicine 2023;102(47):e36069. doi: 10.1097/MD.0000000000036069.

144. Kühn JP, Jahn C, Hernando D, Siegmund W, Hadlich S, Mayerle J, Pfannmöller J, Langner S, Reeder S. T1 bias in chemical shift-encoded liver fat-fraction: role of the flip angle. Journal of Magnetic Resonance Imaging 2014;40(4):875-883.

145. Feng Y, He T, Gatehouse PD, Li X, Harith Alam M, Pennell DJ, Chen W, Firmin DN. Improved MRI R2* relaxometry of iron-loaded liver with noise correction. Magnetic Resonance in Medicine 2013;70(6):1765-1774.

146. Lugauer F, Nickel D, Wetzl J, Kannengiesser SA, Maier A, Hornegger J. Robust spectral denoising for water-fat separation in magnetic resonance imaging. Medical Image

Computing and Computer-Assisted Intervention--MICCAI 2015: 18th International Conference, Munich, Germany, October 5-9, 2015, Proceedings, Part II 18; 2015. Springer. p 667-674.

147. Stein CM. Estimation of the mean of a multivariate normal distribution. The annals of Statistics 1981:1135-1151.

148. Candes EJ, Sing-Long CA, Trzasko JD. Unbiased Risk Estimates for Singular Value Thresholding and Spectral Estimators. IEEE Transactions on Signal Processing 2013;61(19):4643-4657. doi: 10.1109/TSP.2013.2270464.

149. Allen BC, Lugauer F, Nickel D, Bhatti L, Dafalla RA, Dale BM, Jaffe TA, Bashir MR. Effect of a low-rank denoising algorithm on quantitative magnetic resonance imaging-based measures of liver fat and iron. Journal of Computer Assisted Tomography 2017;41(3):412-416.

150. Veraart J, Novikov DS, Christiaens D, Ades-Aron B, Sijbers J, Fieremans E. Denoising of diffusion MRI using random matrix theory. Neuroimage 2016;142:394-406.

151. Lemberskiy G, Baete S, Veraart J, Shepherd TM, Fieremans E, Novikov DS. Achieving sub-mm clinical diffusion MRI resolution by removing noise during reconstruction using random matrix theory. Proc ISMRM; 2019.

152. Moeller S, Pisharady PK, Ramanna S, Lenglet C, Wu X, Dowdle L, Yacoub E, Uğurbil K, Akçakaya M. NOise reduction with DIstribution Corrected (NORDIC) PCA in dMRI with complex-valued parameter-free locally low-rank processing. Neuroimage 2021;226:117539. doi: 10.1016/j.neuroimage.2020.117539.

153. Marchenko VA, Pastur LA. Distribution of eigenvalues for some sets of random matrices. Matematicheskii Sbornik 1967;114(4):507-536. doi: 10.1070/SM1967v001n04ABEH001994.

154. Cordero-Grande L, Christiaens D, Hutter J, Price AN, Hajnal JV. Complex diffusion-weighted image estimation via matrix recovery under general noise models. Neuroimage 2019;200:391-404. doi: 10.1016/j.neuroimage.2019.06.039.

155. Zhang Z, Aygun E, Shih S-F, Raman SS, Sung K, Wu HH. High-resolution prostate diffusion MRI using eddy current-nulled convex optimized diffusion encoding and random matrix theory-based denoising. Magnetic Resonance Materials in Physics, Biology and Medicine 2024:1-17.

156. Lemberskiy G, Chandarana H, Bruno M, Ginocchio LA, Huang C, Tong A, Keerthivasan MB, Fieremans E, Novikov DS. Feasibility of Accelerated Prostate Diffusion-Weighted Imaging on 0.55 T MRI Enabled With Random Matrix Theory Denoising. Investigative radiology 2023;58(10):720-729. doi: 10.1097/RLI.0000000000000979.

157. Liu CY, McKenzie CA, Yu H, Brittain JH, Reeder SB. Fat quantification with IDEAL gradient echo imaging: correction of bias from T1 and noise. Magnetic Resonance in Medicine 2007;58(2):354-364. doi: 10.1002/mrm.21301.

158. Levin YS, Yokoo T, Wolfson T, Gamst AC, Collins J, Achmad EA, Hamilton G, Middleton MS, Loomba R, Sirlin CB. Effect of echo-sampling strategy on the accuracy of out-of-phase and in-phase multiecho gradient-echo MRI hepatic fat fraction estimation. Journal of Magnetic Resonance Imaging 2014;39(3):567-575.

159. Hernando D, Kühn JP, Mensel B, Völzke H, Puls R, Hosten N, Reeder SB. R2* estimation using “in-phase” echoes in the presence of fat: the effects of complex spectrum of fat. Journal of magnetic resonance imaging 2013;37(3):717-726.

160. Caussy C, Reeder SB, Sirlin CB, Loomba R. Noninvasive, quantitative assessment of liver fat by MRI-PDFF as an endpoint in NASH trials. Hepatology 2018;68(2):763-772.

161. Tang A, Tan J, Sun M, Hamilton G, Bydder M, Wolfson T, Gamst AC, Middleton M, Brunt EM, Loomba R. Nonalcoholic fatty liver disease: MR imaging of liver proton density fat fraction to assess hepatic steatosis. Radiology 2013;267(2):422-431.

162. Gavish M, Donoho DL. Optimal shrinkage of singular values. IEEE Transactions on Information Theory 2017;63(4):2137-2152. doi: 10.1109/TIT.2017.2653801.

163. Pruessmann KP, Weiger M, Börnert P, Boesiger P. Advances in sensitivity encoding with arbitrary k-space trajectories. Magnetic Resonance in Medicine 2001;46(4):638-651. doi: 10.1002/mrm.1241.

164. Breuer FA, Kannengiesser SA, Blaimer M, Seiberlich N, Jakob PM, Griswold MA. General formulation for quantitative G-factor calculation in GRAPPA reconstructions. Magnetic Resonance in Medicine 2009;62(3):739-746.

165. Lawrence I, Lin K. A concordance correlation coefficient to evaluate reproducibility. Biometrics 1989:255-268. doi: 10.2307/2532051.

166. Roberts NT, Hernando D, Holmes JH, Wiens CN, Reeder SB. Noise properties of proton density fat fraction estimated using chemical shift–encoded MRI. Magnetic resonance in medicine 2018;80(2):685-695. doi: 10.1002/mrm.27065.

167. Hu HH, Yokoo T, Bashir MR, Sirlin CB, Hernando D, Malyarenko D, Chenevert TL, Smith MA, Serai SD, Middleton MS. Linearity and bias of proton density fat fraction as a

quantitative imaging biomarker: a multicenter, multiplatform, multivendor phantom study. Radiology 2021;298(3):640-651.

168. Mazurowski MA, Buda M, Saha A, Bashir MR. Deep learning in radiology: An overview of the concepts and a survey of the state of the art with focus on MRI. Journal of Magnetic Resonance Imaging 2019;49(4):939-954. doi: 10.1002/jmri.26534.

169. Koonjoo N, Zhu B, Bagnall GC, Bhutto D, Rosen M. Boosting the signal-to-noise of low-field MRI with deep learning image reconstruction. Scientific Reports 2021;11(1):8248. doi: 10.1038/s41598-021-87482-7.

170. Schmidt IL, Haag N, Shahzadi I, Frohwein LJ, Schneider C, Niehoff JH, Kroeger JR, Borggrefe J, Moenninghoff C. Diagnostic image quality of a low-field (0.55 T) knee MRI protocol using deep learning image reconstruction compared with a standard (1.5 T) knee MRI protocol. Journal of Clinical Medicine 2023;12(5). doi: 10.3390/jcm12051916.

171. Zhao R, Hamilton G, Brittain JH, Reeder SB, Hernando D. Design and evaluation of quantitative MRI phantoms to mimic the simultaneous presence of fat, iron, and fibrosis in the liver. Magnetic Resonance in Medicine 2021;85(2):734-747. doi: 10.1002/mrm.28452.

172. Mishro PK, Agrawal S, Panda R, Abraham A. A survey on state-of-the-art denoising techniques for brain magnetic resonance images. IEEE Reviews in Biomedical Engineering 2021;15:184-199.

173. Gavish M, Donoho DL. The optimal hard threshold for singular values is $4/\sqrt {3} $. IEEE Transactions on Information Theory 2014;60(8):5040-5053.

174. Griswold MA, Jakob PM, Heidemann RM, Nittka M, Jellus V, Wang J, Kiefer B, Haase A. Generalized autocalibrating partially parallel acquisitions (GRAPPA). Magnetic

Resonance in Medicine: An Official Journal of the International Society for Magnetic Resonance in Medicine 2002;47(6):1202-1210.

175. Shin PJ, Larson PE, Ohliger MA, Elad M, Pauly JM, Vigneron DB, Lustig M. Calibrationless parallel imaging reconstruction based on structured low-rank matrix completion. Magnetic resonance in medicine 2014;72(4):959-970. doi: 10.1002/mrm.24997.

176. Haldar JP, Zhuo J. P-LORAKS: low-rank modeling of local k-space neighborhoods with parallel imaging data. Magnetic resonance in medicine 2016;75(4):1499-1514. doi: 10.1002/mrm.25717.

177. Lee D, Jin KH, Kim EY, Park SH, Ye JC. Acceleration of MR parameter mapping using annihilating filter-based low rank hankel matrix (ALOHA). Magnetic resonance in medicine 2016;76(6):1848-1864.

178. Shih S-F, Zhang Z, Tasdelen B, Yagiz E, Cui SX, Zhong X, Nayak KS, Wu HH. Multi-coil multi-contrast random matrix theory-based denoising for liver fat and R2* quantification at 0.55T. Proc ISMRM; 2023.

179. Haldar JP. Low-rank modeling of local $ k $-space neighborhoods (LORAKS) for constrained MRI. IEEE transactions on medical imaging 2013;33(3):668-681.

180. Breuer FA, Blaimer M, Mueller MF, Seiberlich N, Heidemann RM, Griswold MA, Jakob PM. Controlled aliasing in volumetric parallel imaging (2D CAIPIRINHA). Magnetic Resonance in Medicine: An Official Journal of the International Society for Magnetic Resonance in Medicine 2006;55(3):549-556.

181. Dietrich O, Raya JG, Reeder SB, Reiser MF, Schoenberg SO. Measurement of signal-to-noise ratios in MR images: influence of multichannel coils, parallel imaging, and

reconstruction filters. Journal of Magnetic Resonance Imaging 2007;26(2):375-385. doi: 10.1002/jmri.20969.

182. Chan CC, Haldar JP. Local perturbation responses and checkerboard tests: Characterization tools for nonlinear MRI methods. Magnetic resonance in medicine 2021;86(4):1873-1887.

183. Fernandes FF, Olesen JL, Jespersen SN, Shemesh N. MP-PCA denoising of fMRI time-series data can lead to artificial activation "spreading". NeuroImage 2023;273:120118.

184. Yokoo T, Serai SD, Pirasteh A, Bashir MR, Hamilton G, Hernando D, Hu HH, Hetterich H, Kühn J-P, Kukuk GM. Linearity, bias, and precision of hepatic proton density fat fraction measurements by using MR imaging: a meta-analysis. Radiology 2018;286(2):486-498.

185. Shih SF, Kafali SG, Calkins KL, Wu HH. Uncertainty-aware physics-driven deep learning network for free-breathing liver fat and R2* quantification using self-gated stack-of-radial MRI. Magnetic Resonance in Medicine 2023;89(4):1567-1585.

186. Guimaraes AR. Quantitative imaging biomarker alliance (QIBA): Protocols and profiles. 2021.

187. Maatman IT, Ypma S, Kachelrieß M, Berker Y, van der Bijl E, Block KT, Hermans JJ, Maas MC, Scheenen TW. Single-spoke binning: Reducing motion artifacts in abdominal radial stack-of-stars imaging. Magn Reson Med 2023;89(5):1931-1944.

188. Solomon E, Rigie DS, Vahle T, Paška J, Bollenbeck J, Sodickson DK, Boada FE, Block KT, Chandarana H. Free-breathing radial imaging using a pilot-tone radiofrequency transmitter for detection of respiratory motion. Magn Reson Med 2021;85(5):2672-2685.

189. Huang SS, Boyacioglu R, Bolding R, MacAskill C, Chen Y, Griswold MA. Free-breathing abdominal magnetic resonance fingerprinting using a pilot tone navigator. J Magn Reson Imaging 2021;54(4):1138-1151.

190. Toomey CM, Cremona A, Hughes K, Norton C, Jakeman P. A review of body composition measurement in the assessment of health. Topics in clinical nutrition 2015;30(1):16-32.

191. Wells JC, Fewtrell MS. Is body composition important for paediatricians? Archives of disease in childhood 2008;93(2):168-172.

192. Kafali SG, Shih S-F, Li X, Kim GHJ, Kelly T, Chowdhury S, Loong S, Moretz J, Barnes SR, Li Z. Automated abdominal adipose tissue segmentation and volume quantification on longitudinal MRI using 3D convolutional neural networks with multi-contrast inputs. Magnetic Resonance Materials in Physics, Biology and Medicine 2024:1-16.

193. Kafali SG, Shih S-F, Li X, Chowdhury S, Loong S, Barnes S, Li Z, Wu HH. 3D neural networks for visceral and subcutaneous adipose tissue segmentation using volumetric multi-contrast MRI. 2021 43rd Annual International Conference of the IEEE Engineering in Medicine & Biology Society (EMBC); 2021. IEEE. p 3933-3937.

194. Strobel KM, Kafali SG, Shih S-F, Artura AM, Masamed R, Elashoff D, Wu HH, Calkins KL. Pregnancies complicated by gestational diabetes and fetal growth restriction: an analysis of maternal and fetal body composition using magnetic resonance imaging. J Perinatol 2023;43(1):44-51.

195. Armstrong T, Ly KV, Ghahremani S, Calkins KL, Wu HH. Free-breathing 3-D quantification of infant body composition and hepatic fat using a stack-of-radial magnetic resonance imaging technique. Pediatric Radiology 2019;49:876-888.

196. Wang Y, Qi H, Wang Y, Xiao M, Xiang C, Dong J, Chen H. Free-breathing simultaneous water-fat separation and T1 mapping of the whole liver (SWALI) with isotropic resolution using 3D golden-angle radial trajectory. Quant Imaging Med Surg 2023;13(2):912.

197. Kee Y, Sandino CM, Syed AB, Cheng JY, Shimakawa A, Colgan TJ, Hernando D, Vasanawala SS. Free-breathing mapping of hepatic iron overload in children using 3D multi-echo UTE cones MRI. Magn Reson Med 2021;85(5):2608-2621.

198. Unal E, Idilman IS, Karçaaltıncaba M. Multiparametric or practical quantitative liver MRI: towards millisecond, fat fraction, kilopascal and function era. Expert Rev Gastroenterol Hepatol 2017;11(2):167-182.

199. Cassinotto C, Feldis M, Vergniol J, Mouries A, Cochet H, Lapuyade B, Hocquelet A, Juanola E, Foucher J, Laurent F. MR relaxometry in chronic liver diseases: comparison of T1 mapping, T2 mapping, and diffusion-weighted imaging for assessing cirrhosis diagnosis and severity. Eur J Radiol 2015;84(8):1459-1465.

200. Hoad CL, Palaniyappan N, Kaye P, Chernova Y, James MW, Costigan C, Austin A, Marciani L, Gowland PA, Guha IN. A study of T1 relaxation time as a measure of liver fibrosis and the influence of confounding histological factors. NMR Biomed 2015;28(6):706-714.

201. Idilman IS, Celik A, Savas B, Idilman R, Karcaaltincaba M. The feasibility of T2 mapping in the assessment of hepatic steatosis, inflammation, and fibrosis in patients with non-alcoholic fatty liver disease: a preliminary study. Clin Radiol 2021;76(9):709.e713-709.e718.

202. Venkatesh SK, Yin M, Ehman RL. Magnetic resonance elastography of liver: technique, analysis, and clinical applications. Journal of magnetic resonance imaging 2013;37(3):544-555.

203. Roberts NT, Tamada D, Muslu Y, Hernando D, Reeder SB. Confounder-corrected T1 mapping in the liver through simultaneous estimation of T1, PDFF, R2*, and B1+ in a single breath-hold acquisition. Magn Reson Med 2023;89(6):2186-2203.

204. Jaubert O, Arrieta C, Cruz G, Bustin A, Schneider T, Georgiopoulos G, Masci PG, Sing-Long C, Botnar RM, Prieto C. Multi-parametric liver tissue characterization using MR fingerprinting: Simultaneous T1, T2, T2*, and fat fraction mapping. Magn Reson Med 2020;84(5):2625-2635.

205. Velasco C, Cruz G, Jaubert O, Lavin B, Botnar RM, Prieto C. Simultaneous comprehensive liver T1, T2, T1ρ, and fat fraction characterization with MR fingerprinting. Magn Reson Med 2022;87(4):1980-1991.

206. Kafali SG, Armstrong T, Shih S-F, Kim GJ, Holtrop JL, Venick RS, Ghahremani S, Bolster Jr BD, Hillenbrand CM, Calkins KL. Free-breathing radial magnetic resonance elastography of the liver in children at 3 T: a pilot study. Pediatric radiology 2022;52(7):1314-1325.

207. Wang N, Cao T, Han F, Xie Y, Zhong X, Ma S, Kwan A, Fan Z, Han H, Bi X. Free-breathing multitasking multi-echo MRI for whole-liver water-specific T1, proton density fat fraction, and quantification. Magnetic resonance in medicine 2022;87(1):120-137.